



Cite this: *Chem. Soc. Rev.*, 2020, **49**, 6884

## Transition metal-based catalysts for the electrochemical CO<sub>2</sub> reduction: from atoms and molecules to nanostructured materials

Federico Franco, Clara Rettenmaier, Hyo Sang Jeon  and Beatriz Roldan Cuenya \*

The electrochemical reduction of carbon dioxide (CO<sub>2</sub>) powered by renewable energy is an attractive sustainable approach to mitigate CO<sub>2</sub> emissions and to produce fuels or value-added chemicals. In order to tackle the challenges related to selectivity, activity, overpotential and durability, transition metal-based catalysts have been widely investigated in the last decades. In an effort to bridge the gap between the fields of homogeneous and heterogeneous catalysis, this review aims to survey the main strategies explored for the rational design of a wide variety of different metal catalysts, ranging from molecular systems to single-atom and nanostructured catalysts. Transition metal complexes containing heme and non-heme ligands have been selected to discuss the recent advances in the understanding of the structure–function relationship in molecular homogeneous catalysis as well as to summarize the main approaches proposed for the heterogenization or confinement of molecular catalysts on conductive surfaces. The main strategies to minimize catalyst cost are also presented, leading to atomically dispersed molecular-like M–N<sub>x</sub> moieties embedded on 2D conducting materials. The superior performances of single-atom catalysts (SACs) and the structural similarity with their molecular analogs, suggest that transition metal catalysts containing well-defined sites may be intrinsically more active and selective towards CO<sub>2</sub> conversion than the bulk heterogeneous materials. Finally, design approaches for metal nanoparticles (NPs) based on size, shape, and support tuning are summarized and compared to novel strategies based on the interaction with surface-bonded organic molecules. The studies herein presented show that the basic principles in molecular catalysis and organometallic chemistry can be effectively used to design new efficient and selective heterogeneous catalysts for CO<sub>2</sub> reduction.

Received 1st July 2020

DOI: 10.1039/d0cs00835d

[rsc.li/chem-soc-rev](http://rsc.li/chem-soc-rev)

Department of Interface Science, Fritz-Haber Institute of the Max Planck Society, 14195 Berlin, Germany. E-mail: [roldan@fhi-berlin.mpg.de](mailto:roldan@fhi-berlin.mpg.de)



**Federico Franco**

*Federico Franco earned a PhD in Chemistry and Material Sciences at the University of Turin in 2016 under the supervision of Prof. Roberto Gobetto. Until 2019, he worked as a postdoctoral researcher at the Institute of Chemical Research of Catalonia (ICIQ) in the group of Prof. Julio Lloret-Fillol, where he focused on the mechanistic understanding of molecular catalysts for the electro- and photochemical activation of small molecules.*

*He is currently a postdoctoral researcher in the Department of Interface Science at the Fritz-Haber Institute of the Max Planck Society, where he is studying heterogeneous electrocatalysts for energy conversion processes.*



**Clara Rettenmaier**

*Clara Rettenmaier received her master's degree in physical chemistry from the Technical University of Munich (Germany) in 2018. She is now a PhD candidate in the Department of Interface Science at the Fritz-Haber Institute of the Max Planck Society, Germany. Her current research focuses on in situ and operando electrocatalytic studies of carbon dioxide reduction.*



# 1. Introduction

The dependence of anthropogenic activities on fossil fuels has contributed to a dramatic rise in the atmospheric CO<sub>2</sub> levels leading to severe environmental issues in our modern society, including global warming and serious pollution problems.<sup>1</sup> In this scenario, the implementation of technologies based on CO<sub>2</sub> utilization to produce carbonaceous fuels and commodity chemicals is highly desirable to drive the transition towards a new green economy.<sup>2–4</sup> Among the proposed approaches, the electrochemical conversion of CO<sub>2</sub> powered by renewable sources is an attractive sustainable alternative to the massive utilization of fossil resources.<sup>5–8</sup> It can occur at ambient conditions and the efficiency of the process can be potentially controlled by the applied bias. Furthermore, this strategy is compatible with an on-site production of a wide variety of organic C<sub>1</sub>- and C<sub>2</sub>-building blocks from a non-toxic, abundant and inexpensive greenhouse gas, mitigating the limitations related to their storage and distribution (especially for toxic gaseous products, like CO).<sup>9</sup>

The electrocatalytic CO<sub>2</sub> reduction reaction (CO<sub>2</sub>RR) may undergo several multi-electron multi-proton pathways, leading to a wide range of carbon-based products.<sup>10</sup> Selectivity is therefore a major challenge in CO<sub>2</sub>RR, since competitive undesired CO<sub>2</sub>RR mechanisms and/or the hydrogen evolution reaction (HER) may interfere with the formation of a specific product. Due to the extreme inertness and stability of the CO<sub>2</sub> molecule, both thermodynamic and kinetic barriers hinder an efficient electrochemical CO<sub>2</sub> activation.<sup>11</sup> In the absence of a catalyst, the direct outer-sphere single-electron reduction of CO<sub>2</sub> to form the CO<sub>2</sub><sup>•−</sup> radical anion is energetically demanding ( $E^0 = -1.90$  V vs. NHE), mainly due to the high reorganizational energy required to bend the linear CO<sub>2</sub> molecule.<sup>12</sup> Proton-assisted multi-electron steps generally lead to thermodynamically more favorable pathways.<sup>13</sup> A transition metal-based catalyst is

often required to lower the activation barrier of the reaction and to drive the process at acceptable rates at specific potentials. The specific interaction of the catalytic metal center with H<sup>+</sup>/CO<sub>2</sub> or CO<sub>2</sub>RR intermediates is crucial to determine the selectivity of the overall process.<sup>14</sup> In addition, a proper kinetic control of the whole catalytic system is essential to achieve the desired selectivity, and factors such as the applied potential, the proton concentration in the reaction medium, and the solubility of CO<sub>2</sub> (e.g. about 0.03 M in common aqueous electrolytes, 0.31 M in CH<sub>3</sub>CN and 0.19 M in DMF<sup>15</sup>) must be also carefully assessed. In the last decades, a plethora of transition metal-based catalysts have been reported for efficient CO<sub>2</sub>RR, ranging from molecular catalysts<sup>16–22</sup> to metal nanoparticles<sup>23,24</sup> and bulk heterogeneous materials.<sup>25–27</sup> In parallel, the increasing interest for *in situ* and *operando* microscopic and spectroelectrochemical (SEC) techniques applied to both, the homogeneous and heterogeneous systems has led to a strong improvement in the fundamental understanding of the factors governing the CO<sub>2</sub>RR process.<sup>28–32</sup> In spite of this, further improvement of the catalyst performance in terms of activity, selectivity and stability is highly desired to match the requirements for practical applications.

In this perspective, we aim to provide an overview of the major advances and trends in the broad field of the electrochemical CO<sub>2</sub>RR, covering the different explored areas from molecular catalysis to nanostructured materials. In addition to the conventional distinction between molecular and heterogeneous catalysts, here we will feature some innovative promising approaches to design novel hybrid catalysts for CO<sub>2</sub>RR with intermediate properties between molecules and bulk materials (Fig. 1).<sup>33–38</sup>

A rational catalyst design primarily requires the elucidation of the structure–activity relationship. The present work will focus on the main reported strategies to control the structure, morphology and chemical composition at the atomic, molecular, supramolecular and nano levels, highlighting how these aspects



**Hyo Sang Jeon**

*Hyo Sang Jeon received his PhD in Clean Energy and Chemical Engineering from the Korea University of Science and Technology (UST-KIST). He is now a postdoctoral researcher in the Department of Interface Science of the Fritz-Haber Institute of the Max Planck Society, Germany. His research mainly focuses on the understanding of structure-chemical state and reactivity correlations during the electrochemical reduction of carbon dioxide.*



**Beatriz Roldan Cuenya**

*Beatriz Roldan Cuenya is a Professor and Director of the Interface Science Department of the Fritz-Haber Institute of the Max-Planck Society in Berlin Germany since 2017. She received her PhD in solid state physics from the University of Duisburg-Essen (Germany) in 2001. She was a postdoctoral scholar at the Chemical Engineering Department of the University of California Santa Barbara (USA) from 2001–2003. She joined the University of Central Florida (USA) as an Assistant Professor of Physics in 2004, and became a full professor in 2012. From 2013–2017 she worked as Professor of Physics at the Ruhr University Bochum (Germany).*





Fig. 1 Different types of transition metal catalysts for CO<sub>2</sub>RR: (a) homogeneous molecular catalysis, (b) surface-anchored molecular catalysis by using several immobilization strategies and (c) heterogeneous catalysis.

affect the reactivity towards CO<sub>2</sub>RR. Some aspects related to the modeling of the electrical interface in a broader sense, such as the effect of the local pH, electrolyte or ionic strength will be also briefly discussed.<sup>39–41</sup> In the attempt to link molecular and heterogeneous systems, a recurrent topic will be the contribution from the fundamental principles of molecular catalysis and coordination chemistry to the design of new efficient materials with tunable activity and selectivity. To emphasize this concept, the CO<sub>2</sub>RR catalytic properties of molecular systems and materials containing active metal sites with structurally similar well-defined coordinative environments will be correlated to each other. Given the huge number of metal complexes reported over the last decades as efficient CO<sub>2</sub>RR catalysts, the discussion about molecular catalysis will be herein mainly limited to metal complexes containing heme (including metalloporphyrins and phthalocyanines) and non-heme (cyclam, cyclam-like and others) macrocyclic ligands as representative examples. There are several reasons supporting this choice. Firstly, they represent one of the most widely studied and relevant families of molecular catalysts reported up to date, being able to promote a highly efficient and selective CO<sub>2</sub> reduction to CO under electrochemical conditions. They also showed an extreme versatility and long-term durability

as both homogeneous and supported catalysts, which make them very appealing systems for scale-up applications. From a fundamental perspective, the mechanistic understanding of the catalytic CO<sub>2</sub>RR for these systems possesses a solid experimental and theoretical basis, providing a broad overview for the critical assessment of structural effects in molecular catalysis, as well as of the strategies for heterogenization of molecular catalysts on solid electrodes. Furthermore, the active M–N<sub>4</sub> moiety of metalloporphyrinoid derivatives or non-heme macrocyclic complexes represents an ideal model to describe the active sites of several reported single-atom electrocatalysts for CO<sub>2</sub>RR. In this regard, we have also included a brief discussion about some representative examples of Ni, Fe and Co molecular catalysts containing non-macrocyclic tetradentate nitrogen ligands, which help us to establish a more intimate connection between the molecular and heterogeneous systems. It is worth reminding that several remarkable classes of molecular catalysts based on 1st/2nd/3rd row transition metals and non-heme ligands (polypyridyl, aminopyridyl, organometallic ligands, *etc.*) have been widely studied for efficient CO<sub>2</sub>RR to HCOOH or CO and comprehensively reviewed in recent works.<sup>16–18,20,42–46</sup> Nevertheless, this work aims to highlight the main concepts and findings from molecular



catalysis that can be useful for the design of new efficient catalysts, rather than providing an exhaustive overview of all the molecular families reported in the literature for CO<sub>2</sub>RR.

After briefly defining the general structural features of the materials discussed in the review (Section 2), the main examples of molecular catalysts containing heme and non-heme macrocyclic ligands for electrocatalytic CO<sub>2</sub> conversion (in homogeneous and surface-immobilized forms, reticular materials and supramolecular assemblies) will be presented in Sections 3 and 4, respectively. The latter address a critical discussion on the different approaches for the heterogenization of molecular catalysts to shed light on the similarities and differences with the homogeneous counterparts. The state-of-the-art of the emerging fields of single-atom catalysts for CO<sub>2</sub>RR will be examined in Section 5, whereas Section 6 will be focused on the recent developments regarding the use of nanostructured catalysts.

## 2. CO<sub>2</sub>RR catalysts based on transition metals

Following a traditional scheme, the transition metal-based catalysts for CO<sub>2</sub>RR are roughly divided into two main categories, corresponding to molecular and heterogeneous catalysts. In molecular catalysis, a well-defined active site is generally proposed, whereby a metal center is surrounded by a specific organic ligand framework (Fig. 1a and b). The coordination environment (first and second coordination sphere) of the catalytic site determines its electronic and steric properties, providing a specific catalyst–substrate interaction under given external conditions (solvent, pH, electrolyte). Thus, the control over the intrinsic activity and selectivity for CO<sub>2</sub>RR is achieved through ligand design by using conventional synthetic methods of organic/organometallic chemistry.<sup>47–50</sup> An accurate investigation of the mechanistic details of the catalytic reaction is generally obtained by using electrochemical and spectroscopic tools, leading to a deep understanding of CO<sub>2</sub>RR mechanistic details. Most of the reported molecular catalysts for CO<sub>2</sub>RR are capable to promote the two-electron (2e) CO<sub>2</sub> conversion to carbon monoxide (CO) or formic acid (HCOOH) with high efficiency and selectivity. On the other hand, clear examples of molecular systems able to produce more than 2e CO<sub>2</sub>RR reduction products are still rare.<sup>51–53</sup> Furthermore, molecular systems generally suffer from low current densities, which limit their implementation in real devices for scale-up applications.

In sharp contrast, bulk heterogeneous catalysts usually contain a large number of poorly characterized active surface states, without a full structural control at the molecular or atomic levels (Fig. 1c). These aspects typically result in considerably higher current densities in comparison with the molecular systems, at the expense of a lower selectivity and a more difficult rationalization of the process. Nevertheless, although the HER is generally favored over CO<sub>2</sub>RR on several metal electrodes (*e.g.* Ni, Fe, Ti, Pt) in aqueous media, a number of transition metals have been shown to produce CO (*e.g.* Au, Ag, Zn)<sup>54</sup>

or HCOOH (*e.g.* In, Sn, Cd) with high faradaic yields.<sup>55</sup> The product distribution is generally determined by the relative binding energies of adsorbed \*CO, \*COOH and \*H intermediates (\* indicates the adsorption site on the metal surface), which are strongly dependent on the metal's electronic structure (*i.e.* density of states).<sup>10,56–58</sup> Weak \*CO binding on the metal surface facilitates CO desorption and evolution (Au), whereas too large \*CO adsorption energies are detrimental for CO<sub>2</sub>RR, leading to catalyst poisoning and a preference for HER (Pt). For intermediate \*CO binding energies (*e.g.* Cu), \*CO is not easily desorbed and undergoes further reductive and/or alternative chemical steps (protonation, coupling reactions) enabling the formation of the target >2e CO<sub>2</sub>RR products, such as hydrocarbons or alcohols.<sup>14,59–65</sup>

In the last years, the rigid dualism between molecules and heterogeneous catalysts has been gradually overcome through the investigation of novel families of materials with specific molecularly or atomically defined properties. As such, emerging classes of hybrid heterogeneous catalysts showed superior CO<sub>2</sub>RR performances than the molecular counterparts albeit preserving the integrity of the molecular catalytic site (Fig. 1). The main families of transition metal-based catalysts investigated by the current research in the CO<sub>2</sub>RR field can be summarized as follows:

- Homogeneous molecular catalysts, which are typically organometallic complexes able to promote electrochemical CO<sub>2</sub>RR when dissolved in common organic electrolytes (CH<sub>3</sub>CN, THF, DMF, NMP). In this case, the catalyst is a molecule freely-diffusing in solution with a well-defined standard potential and acts as a redox mediator between the electrode and the substrate (Fig. 1a). In most instances, the real active species is electro-generated *in situ*: when the applied bias matches the redox potential of the catalyst, the catalyst precursor gets reduced at the electrode surface forming the catalytic species which, in turn, reacts with the substrate with kinetics ( $k_{\text{cat}}$ ) depending on its intrinsic activity and the external conditions (*e.g.* applied potential, medium). In homogeneous electrocatalysis, only a small fraction (confined in the diffusion layer) of the total amount of catalyst present in solution ( $\approx$  mM concentration) is directly involved in the catalytic process. The catalytic behavior can be accurately studied by electrochemical (cyclic voltammetry) and complementary *in situ* spectro-electrochemical methods (UV-Vis, FTIR, EPR, Raman) to identify the main intermediate species involved in the process. In some cases, the reaction intermediates can be even chemically synthesized and isolated. Homogeneous catalysts are ideal candidates to investigate the catalytic CO<sub>2</sub>RR mechanism at a fundamental level, but deactivation pathways occurring in solution or on the electrode surface affect their long-term stability.

- Heterogenized molecular catalysts, whereby the catalytic species no longer diffuses in solution but is immobilized on the electrode, thus improving the electrical contact between the electrode and the catalyst at the interface (Fig. 1b).<sup>45,66,67</sup> Although a number of water-soluble molecular catalysts for CO<sub>2</sub>RR have been reported so far,<sup>68–71</sup> the electrode functionalization approach allows to overcome the solubility limitations



in aqueous electrolytes often reported for homogeneous catalysts (most of them are soluble in organic solvents or organic-water mixtures), and helps to facilitate the catalyst recycling and the separation of liquid CO<sub>2</sub>RR products. Moreover, the physicochemical interactions at the catalyst-electrode interface may induce drastic reactivity changes, including altering the conventional reaction pathways occurring in the homogeneous phase. In this perspective, the fundamental understanding of these factors would represent a powerful tool to tune the reactivity, activity and selectivity of molecular catalysts. The heterogenized electrocatalysts consist of thin films containing a number of active sites ( $10^{-7}$ – $10^{-12}$  mol cm<sup>-2</sup>) which is highly dependent on the catalyst loading and the deposition method. The strategies used for molecular catalyst immobilization can be divided into three main classes: (1) electropolymerization, which leads to the formation of electroactive polymer films with high surface densities and porosity.<sup>72</sup> Depending on the number of voltammetric cycles, a precise control over the thickness and surface coverage may be obtained; (2) covalent attachment to the surface through the presence of different functional groups (amino, diazonium, thiol, carboxylic acids, *etc.*), which typically entails the formation of robust films with low surface coverage ( $\approx 10^{-10}$ – $10^{-12}$  mol cm<sup>-2</sup> for a monolayer);<sup>73,74</sup> (3) immobilization *via* non-covalent ( $\pi$ - $\pi$  stacking) interactions, which generally provides higher catalyst densities ( $\approx 10^{-8}$  mol cm<sup>-2</sup>) but also a less controlled surface functionalization.<sup>75</sup> In analogy with the homogeneous case, surface spectroscopic techniques are used to gain mechanistic insight into the catalytic process. Low catalyst loading, partial catalyst detachment during operation, poor electrochemical contact and the need for elaborated synthetic strategies are the main limitations of classical functionalization methods.

• Reticular 3D materials, in which the active molecular unit is encapsulated into porous organic or metalorganic ordered architectures with tunable structure and properties. Among them, covalent organic frameworks (COFs), metal organic frameworks (MOFs) or porous supramolecular assemblies are versatile platforms used to significantly improve the robustness of a catalyst under electrochemical conditions. In principle, the combination of the characteristic physical properties of MOF and COF materials (*e.g.* high surface area, adjustable pore size) with suitable integrated molecular building blocks enables to fine-tune their activity and selectivity for CO<sub>2</sub>RR.<sup>33</sup> However, an accurate control over the thickness of the layers grown on the electrode is essential to optimize the electron and mass transport properties of the material and, therefore, to maximize the efficiency of the process.<sup>76</sup> Furthermore, the catalytic performance of these materials is typically limited by an inefficient charge carrier mobility, which leads to slow electron kinetics. In this regard, imine-based COFs have shown enhanced electronic properties, improving the electrical connection between the active sites of the layered material.<sup>77–79</sup> Moreover, in comparison with conventional heterogenization methods, the imine (or amine) groups contained in the microporous matrix, together with its specific porous morphology favor the capture of CO<sub>2</sub>, leading to an increase in the local CO<sub>2</sub>

concentration at the catalytic sites (especially in aqueous media).<sup>80–82</sup> Homogeneous, heterogenized and reticular systems can be defined as molecular materials, since the metalorganic active site preserves its fundamental structural and electronic properties at a molecular level even after the heterogenization process.<sup>83</sup>

• Single-atom catalysts (SACs), a rapidly emerging unique class of materials bridging the molecular and heterogeneous catalysis fields. In SACs, transition metal atoms are atomically dispersed on a 2D support and stabilized through the coordination to heteroatom (usually N, C, P or S) dopants. Indeed, the active sites are homogeneously distributed on a conductive surface, mimicking the coordination environment of molecular complexes. This feature enables an accurate structural characterization of the catalyst at an atomic scale and, at the same time, maximizes the number of free coordination sites per metal atom. Unlike the molecular materials, the SACs are generally obtained by thermal treatment of generic metal precursors (inorganic salts) and heteroatom-rich organic molecules which, depending on the synthetic conditions, give rise to isolated molecular-like surface units. A challenge from this approach is however to demonstrate that in fact only SAC motifs are available on the as prepared samples (as opposed to a mixture of single atoms and small clusters or nanoparticles) as well as the difficulty of keeping such SAC motifs stable under reaction conditions. Doped carbon-based materials are generally used as suitable supports for SACs, due to their high specific surface area and tunable surface properties.

• Nanostructured materials, which comprise metal clusters (MCs) and nanoparticles (NPs), differing from each other by the number of atoms. These materials are extremely attractive for CO<sub>2</sub>RR, due to their high surface-to-volume-ratios and the presence of several low-coordinated reactive surface sites. Their properties are strongly dependent on their size (from approximately 1–5 to hundreds of nanometers), aggregation level, shape and composition (mono- or multimetallic). The nanostructured materials represent the last frontier between the molecular materials and the extended (mainly metallic) surfaces, which include single-crystal and polycrystalline materials.

It is worth mentioning that the classification reported above is meant to exemplify the rationalization of the enormous number of CO<sub>2</sub>RR catalysts reported in the literature, in an effort to give a general perspective of the multi-faceted CO<sub>2</sub>RR field. Some interesting limiting cases that lay out of this classification, including the *in situ* decomposition of homogeneous catalysts under electrochemical conditions to form active nanostructured deposits on the electrode, are beyond the scope of the present review.<sup>84</sup> Nonetheless, the case of Ni-cyclam catalyst will be discussed as an example of *in situ* heterogenization of molecular systems, highlighting the critical role that the specific interactions between the adsorbed molecular reduced species and the electrode surface may play in catalysis. Furthermore, a discussion on CO<sub>2</sub>RR promoted by organic or metal-free catalysts will not be included in this review.



### 3. Molecular catalysts for CO<sub>2</sub>RR containing heme ligands

As anticipated above, here we discuss the main examples of molecular materials for CO<sub>2</sub>RR reported in the literature based on metal complexes with heme ligands, including porphyrin and phthalocyanine derivatives. The first paragraphs describe the most relevant systems based on Fe and Co, highlighting the main strategies for catalyst optimization in both homogeneous and heterogenized approaches. The last paragraph will instead summarize the main findings reported for analogous systems containing other transition metals.

#### 3.1 Iron

**3.1.1 Homogeneous molecular catalysis.** The electrochemical activation of CO<sub>2</sub> mediated by electrogenerated iron(0) porphyrins as homogeneous catalysts has been widely explored over more

than 30 years (Chart 1). In particular, the detailed kinetic studies performed by Savéant, Costentin, Robert and coworkers have strongly contributed to improve the fundamental understanding of molecular CO<sub>2</sub>RR catalysis.<sup>47,85–87</sup> The pioneering studies on the parent [Fe(TPP)]Cl compound (FeTPP, **1**, see Chart 1) (TPP = *meso*-tetraphenylporphyrin) in a DMF electrolyte date back to the 1980s, indicating that the electrogenerated [Fe(TPP)]<sup>2–</sup> species is catalytically active.<sup>88</sup> Although the [Fe<sup>0</sup>(TPP)]<sup>2–</sup> mesomeric form with a formal Fe<sup>0</sup> oxidation state was found to play a crucial role in the reactivity of the active species,<sup>89</sup> recent combined spectroscopic and computational studies suggested that the electronic structure of its ground state can be more properly described by the [Fe<sup>II</sup>(TPP••)]<sup>2–</sup> form, whereby the porphyrin ring strongly participates to the electron delocalization.<sup>90–92</sup>

In aprotic conditions, a modest catalytic response was observed at the formal Fe<sup>I/0</sup> wave under CO<sub>2</sub> atmosphere, corresponding to very low faradaic yields for CO formation and low catalyst



Chart 1 Synthetic molecular Fe porphyrin systems reported as homogeneous catalysts for CO<sub>2</sub>RR.



stability. However, the addition of Lewis<sup>93,94</sup> or Brønsted<sup>95,96</sup> acids significantly improved the efficiency of the catalytic CO<sub>2</sub>RR process in terms of intrinsic activity, selectivity to CO and durability (number of catalytic turnovers) (Fig. 2). In the presence of mono- (Li<sup>+</sup>, Na<sup>+</sup>) or divalent (Mg<sup>2+</sup>, Ca<sup>2+</sup>, Ba<sup>2+</sup>) cations, carbon monoxide was predominantly produced with formate as a byproduct.<sup>94</sup> An even more remarkable boosting effect on catalysis was triggered by the addition of weak/moderate organic acids (CF<sub>3</sub>CH<sub>2</sub>OH, PhOH), resulting in excellent faradaic efficiencies (FEs) for CO production, with no hydrogen or formate being detected.<sup>86,95,96</sup> The catalytic currents for CO<sub>2</sub>RR and the catalyst lifetime increased proportionally to the acidity of the medium. Room-temperature ionic liquids (RTILs) have been also recently reported to enhance the CO<sub>2</sub>RR performances of **1** in the presence of CF<sub>3</sub>CH<sub>2</sub>OH as an external proton source.<sup>97</sup>

The electrochemical catalytic CO<sub>2</sub>-to-CO conversion mediated by FeTPP in the presence of Lewis or Brønsted acids has been proposed to occur *via* a two-electron “push-pull mechanism”.<sup>94,96</sup> In the first step, the electrogenerated active [Fe(TPP)]<sup>2-</sup> species interacts with CO<sub>2</sub> to form a key [Fe(CO<sub>2</sub>)(TPP)]<sup>2-</sup> adduct, in which the electron density is “pushed” from the nucleophilic metal center to the electrophilic CO<sub>2</sub> molecule. The asymmetric [Fe<sup>I</sup>(CO<sub>2</sub>•<sup>-</sup>)]<sup>2-</sup> resonance form has been proposed to be the predominant structure, in agreement with DFT calculations (Scheme 1).<sup>86,87,98</sup> Through an ion-pair (Lewis) or H-bonding (Brønsted) formation, the acid stabilizes the intermediate and

helps to “pull” the electron density out of the substrate, thereby facilitating the C–O cleavage step. Notably, an additional stabilization of the key intermediates due to an intramolecular H-bonding allowed the experimental detection of a [Fe<sup>II</sup>CO<sub>2</sub>]<sup>2-</sup> adduct and its protonated [Fe<sup>II</sup>CO<sub>2</sub>H]<sup>-</sup> derivative at cryogenic temperatures using vibrational spectroscopy.<sup>99</sup> This scheme is also consistent with the reported catalytic behavior of a dimeric Fe porphyrin system, whereby the catalytic response of the catalytic Fe site is enhanced by the intramolecular assistance of the second Fe porphyrin unit.<sup>100</sup>

The role of added Brønsted acids in the proton-assisted mechanism of FeTPP was systematically investigated in detailed kinetic studies, based on the “foot-of-the-wave” analysis (FOWA) of the voltammetric profiles.<sup>85,86,101</sup> In the initial stage of the process, an acid molecule (AH) undergoes an H-bonding stabilization of the [Fe(CO<sub>2</sub>)(TPP)]<sup>2-</sup> primary intermediate ([Fe<sup>I</sup>(CO<sub>2</sub>•<sup>-</sup>)]<sup>2-</sup> predominant resonance form, *vide supra*), followed by a successive dehydration step involving another AH molecule which leads to the cleavage of the C–O bond (Scheme 1).<sup>86,102</sup> At moderate acid concentrations, a proton-coupled intramolecular electron transfer from the iron center to CO<sub>2</sub>, concerted with the breaking of the C–O bond, was unambiguously determined to be the rate-determining step of the catalytic process.<sup>86,98,102,103</sup> The subsequent [Fe<sup>II</sup>(CO)(TPP)] intermediate undergoes fast CO release, closing the catalytic cycle upon homogeneous single electron transfer by another formal Fe<sup>0</sup> species (Scheme 1). The extreme robustness, efficiency and selectivity of **1** towards CO formation for a wide range of concentrations of various mild proton donors is appealing for several applications. Recently, Skrydstrup and



Fig. 2 Cyclic voltammetry of FeTPP (**1**) (1 mM) in DMF + 0.1 M *n*-Bu<sub>4</sub>NPF<sub>6</sub>, in the absence (blue) and presence of 0.23 M CO<sub>2</sub> and of 10 mM PhOH (red). Sketch of the electrochemical reactions. Adapted with permission from ref. 86. Copyright 2013 American Chemical Society.



Scheme 1 Proposed catalytic mechanism for the electrochemical CO<sub>2</sub>-to-CO mediated by [Fe(TPP)Cl] (**1**) in organic media in the presence of Brønsted acids.<sup>86,102</sup>



collaborators have developed a low-cost and scalable setup to use the CO generated by the FeTPP-mediated CO<sub>2</sub> electro-reduction in homogeneous phase as reactant in Pd-catalyzed carbonylation reactions for the synthesis of pharmaceutically relevant molecules.<sup>104,105</sup>

The acidity of the reaction medium primarily affects the overpotential and selectivity of FeTPP (**1**) (Chart 1). When strong acids are employed (*e.g.* Et<sub>4</sub>NH<sup>+</sup>, CH<sub>3</sub>COOH), metal protonation occurs and the competitive HER becomes the main pathway. On the other hand, weak proton donors, like 1-propanol (PrOH), generally induce sluggish kinetics for CO<sub>2</sub>RR with non-selective formation of CO (FE ≈ 60%) and formate (FE ≈ 35%) mixtures.<sup>96</sup> A recent report suggests that the addition of tertiary amines is an effective strategy to drive the selectivity of **1** towards HCOOH formation in the presence of weak acids.<sup>106</sup> The strong *trans*-coordination of tertiary amines to the Fe center increases the basicity of the central C-atom of the substrate in the [Fe(CO<sub>2</sub>)(TPP)]<sup>2-</sup> adduct, thereby facilitating its protonation with the subsequent release of formate. Following this approach, FEs as high as 68% or 72% for HCOOH were obtained by adding 40 mM of quinuclidine or trimethylamine to a 40 mM PrOH solution of **1**, respectively.<sup>106</sup> In contrast with the conventional pathway for HCOOH formation based on net CO<sub>2</sub> insertion into a reactive M–H bond (a common intermediate to HER),<sup>107,108</sup> this alternative strategy uses weak acids to produce HCOOH, circumventing the formation of undesired hydride species.

On the basis of the accurate elucidation of the CO<sub>2</sub>RR catalytic mechanism of the parent system and the extreme versatility of the porphyrin moiety, in the last decade numerous efforts have been directed to the rational design of novel iron porphyrin-based catalysts. In particular, a number of studies have focused on the correlation between the electronic and steric effects of different substituents on the porphyrin ring and the CO<sub>2</sub>RR activity of the catalyst (Chart 1). The substituent effects can be divided into two categories, defined as through-structure and through-space effects, respectively (Fig. 3 and 4).<sup>47,109</sup> The former term mainly refers to the use of mesomeric or inductive effects promoted by electron-withdrawing or electron-donating substituents to modify the electronic structure of the catalyst.<sup>110,111</sup> To investigate the influence of the through-bond inductive effect on CO<sub>2</sub>RR, the electrochemical behavior of the unsubstituted FeTPP compound (**1**) was systematically compared with a series of Fe tetraphenylporphyrins, containing different degrees of substitution with perfluoro (**2–4**) and *o,o'*-methoxy *meso* aryl groups (**5**) (see Chart 1 and Fig. 3).<sup>110,112</sup> The correlation between the catalytic rate (defined as maximum turnover frequency or TOF<sub>max</sub>) and the standard redox potential of a catalyst ( $E_{\text{cat}}^0$ ) enables a rational evaluation of the electronic substitution effect on the catalytic performance within the same family of molecular catalysts.<sup>113–117</sup> The analysis of the inductive effects in the series **1–4** gives rise to a linear scaling relationship, which highlights two opposite trends (Fig. 3a, right): for electron-withdrawing groups, the positive impact on the  $E_{\text{cat}}^0$  is partially balanced by lower catalytic rates, as a consequence of a diminished nucleophilicity of the Fe<sup>0</sup> center. In turn, electron-donating

substituents tend to enhance the reactivity of the catalytic center at the expense of a less favorable catalytic potential. In other words, considerations solely focused on electronic effects (*i.e.* the so-called “redox innocence” and “non-innocence” of the ligand frameworks<sup>89</sup>) leave little room for the optimization of the catalyst.

The modeling of through-space interactions between specific residues in the second or outer coordination sphere and the metal center may activate alternative mechanistic pathways for a catalytic reaction, giving rise to new scaling relations. This strategy represents a powerful tool for catalyst optimization and has been effectively used in molecular catalysis to circumvent the tradeoff between rate and overpotential forced by the scaling relationships observed with substituents displaying bare inductive effects.<sup>112,118,119</sup> A first common approach consists in the use of local proton sources or H-bond donors on the porphyrin moiety. Depending on the specific spatial orientation of the pendant groups, they may induce a strong boosting effect on the CO<sub>2</sub> reduction catalysis, due to a stabilization of the Fe–CO<sub>2</sub> adduct by intramolecular H-bonding and/or an increase of the local concentration of proton donors. For instance, the introduction of eight phenolic functionalities in *ortho*, *ortho'* positions of the porphyrin phenyls (**6**) led to a dramatic enhancement of the catalytic properties of **1**, resulting in a durable and selective CO production (FE<sub>CO</sub> = 94%, FE<sub>H<sub>2</sub></sub> = 6%) at –1.16 V vs. NHE ( $\eta$  = 0.466 V) in DMF/0.1 M NBu<sub>4</sub>PF<sub>6</sub> + 2 M H<sub>2</sub>O.<sup>120</sup> It clearly outperformed the corresponding methoxy derivative (**5**), thus unambiguously confirming the crucial role played by the pre-positioned OH groups in **6** on CO<sub>2</sub>RR. The latter act both as intramolecular proton relays, facilitating the successive protonation and C–O bond cleavage steps, and as H-bonding stabilizers of the primary Fe–CO<sub>2</sub> intermediate formed between the electro-generated formal Fe<sup>0</sup> and CO<sub>2</sub>. As a consequence of the additional H-bonding stabilization induced by the pendant hydroxyl groups, catalysis requires a second electron uptake after the Fe–CO<sub>2</sub> adduct formation, which is more difficult than the first one, unlike for the unsubstituted FeTPP catalyst (**1**, Scheme 1).<sup>87,98,102</sup> In the case of the catalyst **6**, the second electron transfer, required to close the catalytic cycle, was suggested to be concerted with the breaking of one of the two C–O bonds of CO<sub>2</sub> and with proton transfer.<sup>87</sup> A combination of the inductive and spatial effects may lead to catalysts with superior activity. As an example, the perfluorination of two opposite phenyl rings of **6** gave rise to the catalyst **7** with improved CO<sub>2</sub>RR performances.<sup>121</sup> The choice for a suitable reaction medium is another crucial aspect to consider for catalyst optimization.<sup>122,123</sup> An asymmetric tetraphenylporphyrin iron catalyst **8** containing only a single proton relay revealed to be a poor CO<sub>2</sub>RR catalyst in DMF, whereas a strong enhancement in the catalytic response was observed in CH<sub>3</sub>CN.<sup>122</sup>

In an attempt to mimic the key stabilizing role of amino acid residues by H-bonding interaction in enzymatic systems, a number of varying H-bond donor groups have been incorporated in the structure of iron porphyrin complexes.<sup>99,124–127</sup> The effect of different hanging proton donors (phenol (**9**), guanidine (**10**) and sulfonate (**11**) groups) at a dibenzofuran scaffold



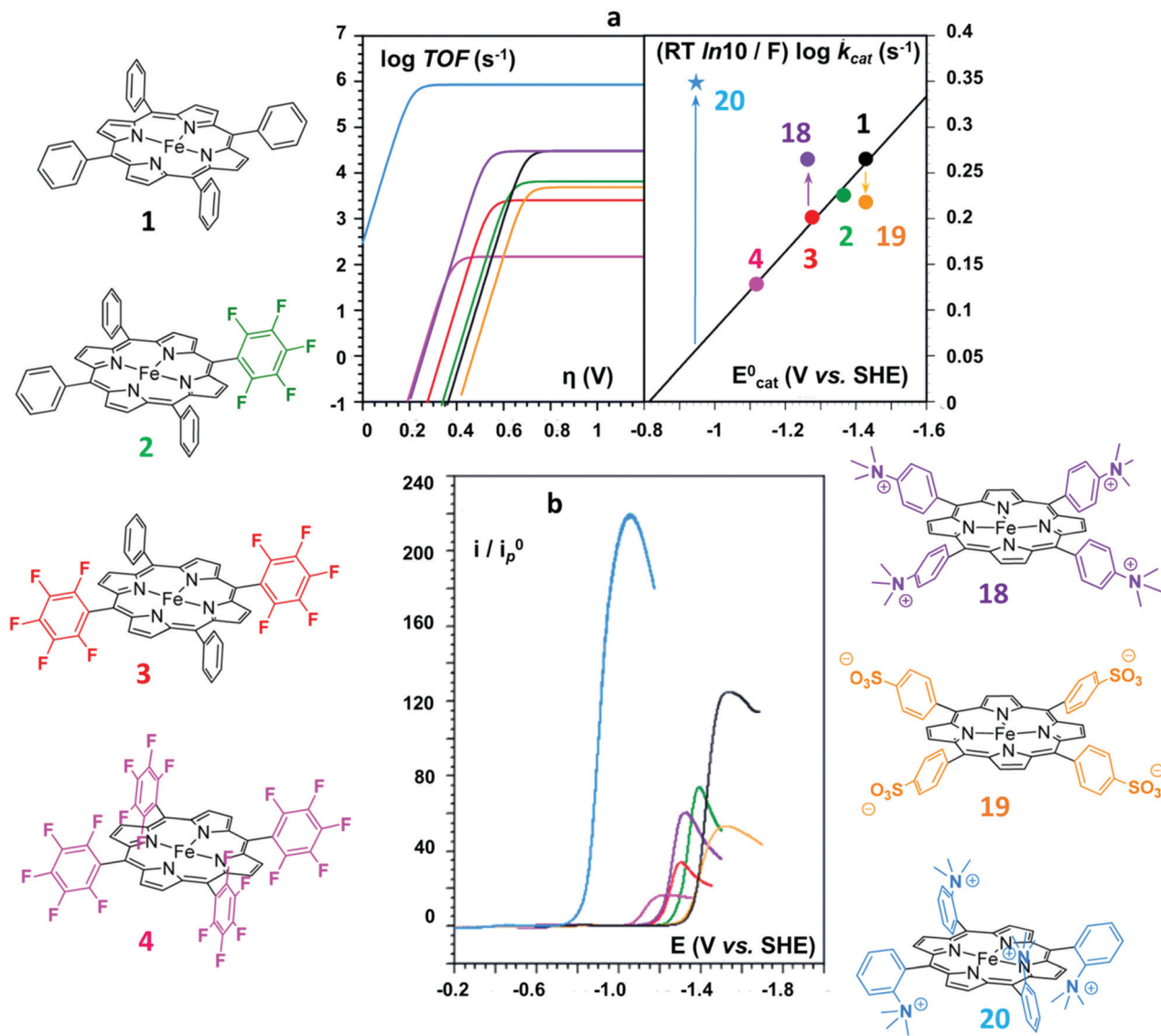


Fig. 3 Structure substituent effects and Coulombic interaction effects of positively and negatively charged substituents on electrocatalytic  $\text{CO}_2$  conversion to CO by the series of homogeneous Fe porphyrin catalysts 1–4 and 18–20: (a) catalytic Tafel plots (left) and correlation between  $\text{TOF}_{\text{max}} = k_{\text{cat}}$  and  $E_{\text{cat}}^0$  (right); (b) cyclic voltammetry of **20** (light blue), **4** (magenta), **3** (red), **18** (purple), **2** (green), **1** (black), and **19** (orange) in the potential domain of the catalytic  $\text{CO}_2$  reduction wave in DMF + 0.1 M  $n\text{-Bu}_4\text{NPF}_6$  + 0.1 M  $\text{H}_2\text{O}$  + 3 M PhOH, at 0.1  $\text{V s}^{-1}$  under 1 atm  $\text{CO}_2$  (catalyst conc.: 1 mM). The current,  $i$ , is normalized against the peak current of the one-electron  $\text{Fe}^{\text{II}}/\text{Fe}^{\text{I}}$  reversible wave,  $i_p^0$ , obtained at the same scan rate (0.1  $\text{V s}^{-1}$ ). Adapted with permission from ref. 112. Copyright 2016 American Chemical Society.

has been explored in a series of iron hangman porphyrins.<sup>124</sup> Although an excellent selectivity to CO was obtained in all three cases (FES > 93%), the  $\text{CO}_2\text{RR}$  catalytic rate was found to follow the  $9 > 10 > 11$  order, highlighting the detrimental effect of the deprotonated pendant sulfonate group on catalysis due to unfavorable electrostatic interactions. While the hanging guanidine group in **10** could potentially mimic the role played by arginine in several  $\text{CO}_2$  binding proteins,<sup>128</sup> it was found to interact *via* H-bonding more favorably with the porphyrin platform than with  $\text{CO}_2$ , resulting in a minor activity of **10** in comparison with **9**. Recently, Chang and co-workers have systematically investigated a series of four positional isomers (12–15) with amide functionalities in the *ortho*- or *para*-positions

of the *meso* phenyl ring, exploring the effect of both proximal and distal N–H configurations with respect to the porphyrin platform.<sup>125</sup>  $\text{CO}_2$  reduction analysis revealed that the presence of the amide group in the *ortho* position is required to observe a significant increase in  $\text{CO}_2\text{RR}$  activity, with the distal isomer (**14**) being the most active across the series. This resulted from a more favorable spatial location of the amide group which leads to an enhanced H-bonding stabilization of the  $\text{Fe}\text{-CO}_2$  intermediate. The presence of local urea functional groups, able to establish multipoint H-bonding with the metal-bound  $\text{CO}_2$  molecule, was reported to have an even stronger effect on catalysis in comparison with the amide groups.<sup>126</sup> In particular, due to the cooperative effect of four urea groups, the biomimetic complex **16**



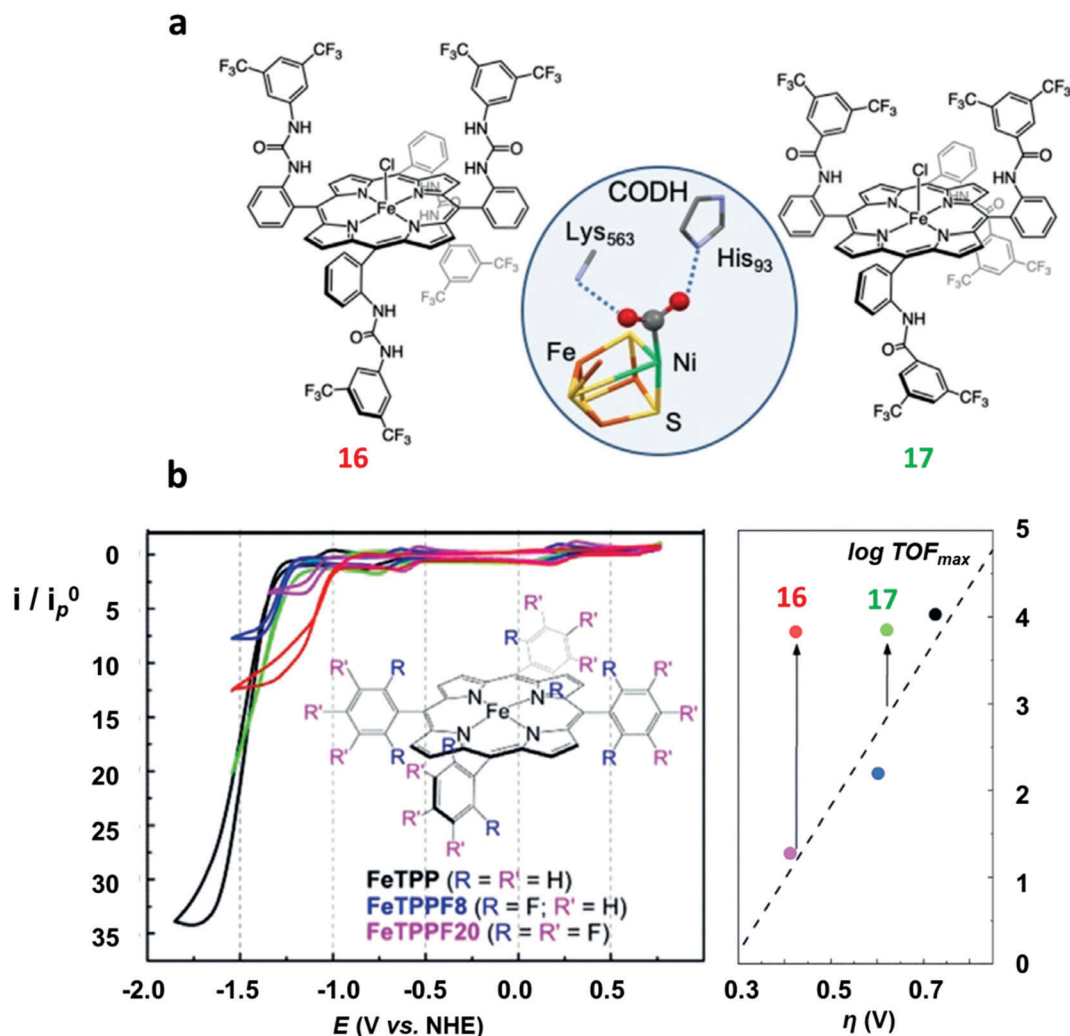


Fig. 4 (a) Molecular drawing of **16** (left) and **17** (right). The X-ray structure of the FeNi active site (C-cluster) of CO dehydrogenase (CODH)<sup>134</sup> (center) is shown for comparison. (b) Cyclic voltammograms of 1 mM FeTPP (**1**, black) and its modified analogues (blue = FeTPPF8, pink = FeTPPF20 (**4**), green = **17**, red = **16**) in DMF containing 0.1 M *n*-Bu<sub>4</sub>NPF<sub>6</sub> at 25 °C under argon (top left) and under CO<sub>2</sub> with 5.5 M water as proton source (bottom left). Plot of calculated TOF<sub>max</sub> (from FOW analysis) as a function of the catalytic overpotential (right). Adapted with permission from ref. 126. Copyright 2019, Wiley-VCH.

exhibited a considerably higher intrinsic CO<sub>2</sub>RR activity than the amide-containing derivative **17**, resulting in a comparable TOF value as to **1** at ca. 300 mV more positive overpotential (Fig. 4).

As an alternative strategy to a directional intramolecular H-bonding interaction, the stabilization of negatively charged iron-CO<sub>2</sub> bound intermediates may also be obtained *via* through-space Coulombic interaction with positively charged pendant groups spatially oriented in the proximity of the active site.<sup>47</sup> This effect was first demonstrated by the enhanced CO<sub>2</sub>RR activity of complex **18**, in which the presence of four trimethylanilinium groups in a *para* position of the TPP phenyl rings resulted in a marked upper left deviation from the linear through-structure effect relationship between catalytic rate and catalyst redox potential (Fig. 3a, right).<sup>112</sup> A comparable effect but opposite in sign was observed by replacing the trimethylanilinium substituents with negatively charged sulfonate groups (**19**), owing to unfavorable electrostatic interactions. Furthermore, the derivative bearing the quaternary ammonium

groups in *ortho* positions (compound **20**) exhibited a significant decrease of the catalytic overpotential while dramatically increasing the TOF (Fig. 3). This effect also leads to a parallel improvement of the molecular catalytic Tafel plot, which correlates the catalyst efficiency (log TOF) and the overpotential (defined as the difference between the applied potential and the standard potential of the reaction to be catalyzed, in general  $A \rightarrow B$ ,  $\eta = E_{AB}^0 - E$ ) (Fig. 3a, left). Despite the fact that there is some debate on the value of the standard potential for the CO<sub>2</sub>/CO couple in organic solvents,<sup>49,129,130</sup> complex **20** represents the most efficient homogeneous molecular catalyst for selective CO<sub>2</sub>-to-CO electroreduction reported to date, displaying an unprecedented maximum TOF value of  $\approx 10^6$  s<sup>-1</sup> at a 220 mV overpotential. Remarkably, the selectivity to CO is nearly quantitative even in the presence of high concentration of phenol (3 M). Moreover, **20** showed an excellent durability, without any selectivity loss after 84 h electrolysis under CO<sub>2</sub> on different working electrodes.<sup>112</sup> Taking advantage of the ionic character of the



porphyrin, the trimethylammonium derivative **18** was also employed to drive homogeneous CO<sub>2</sub> conversion to CO in an aqueous electrolyte.<sup>68,98</sup> At a close to neutral pH (6.7), CO was electrocatalytically produced with a FE of 90%, with only a minor amount of H<sub>2</sub> (7%) at  $-0.97$  V vs. NHE.<sup>68</sup> Analogously to trimethylammonium cations, pendant methylimidazolium moieties in the complex **21** displayed a positive effect on CO<sub>2</sub>RR catalysis in a DMF/H<sub>2</sub>O mixture due to the electrostatic stabilization of the reaction intermediate.<sup>131</sup> In a homogeneous 0.1 M KCl aqueous solution, **21** showed an excellent selectivity to CO (91%) at low overpotential ( $-0.948$  V vs. NHE,  $\eta = 418$  mV).

**3.1.2 Heterogenized molecular catalysis.** In parallel with the design of homogeneous water-soluble catalysts, several heterogenization approaches have been explored to perform CO<sub>2</sub>RR in aqueous electrolytes with iron porphyrin systems (Fig. 5). A straightforward electropolymerization method was used to control the deposition of microporous films of a carbazole-functionalized tetraphenylporphyrin on a glassy carbon (GC) surface (Fig. 5a). However, the catalytic studies were carried out only in organic media (CH<sub>3</sub>CN), resulting in a severe catalyst deactivation likely due to a partial carboxylation of the porphyrin backbone.<sup>72</sup> A substantial improvement was obtained by the immobilization of a modified iron tetraphenyl porphyrin bearing six pendant OH groups in *ortho* and *ortho'* positions to multi-walled carbon nanotubes (MWCNTs) *via* either non-covalent and covalent interactions.<sup>132,133</sup> In the former case, the pyrene-modified porphyrin moiety of the catalyst is grafted on the carbon surface *via*  $\pi$ - $\pi$  stacking interactions (Fig. 5d). This immobilization strategy was found to preserve the intrinsic catalytic properties of the molecular catalyst, leading to an almost exclusive production of CO (TON = 432 after 3 h electrolysis) at  $-1.03$  V vs. NHE ( $\eta = 480$  mV) in neutral aqueous conditions (pH 7.3). The durability of the functionalized electrode is also remarkable, reaching a TON value of 813 after 12 h with a catalytic selectivity of 85%.<sup>133</sup>

Analogous results were obtained for a similar system, whereby the pyrene-terminal linker on the porphyrin moiety was replaced by a phenyl ring with a carboxylic acid at the para position (Fig. 5b). The coupling between the  $-\text{COOH}$  group of the catalyst and the surface  $-\text{NH}_2$  groups of the MWCNT electrode led to a covalent attachment of the catalyst through the formation of an amide linkage.<sup>132</sup> At a slightly more negative applied potential ( $-1.06$  V vs. SHE,  $\eta = 510$  mV), the functionalized electrode showed an excellent selectivity for CO production (80–90%) over 3 hours electrolysis. Remarkably, a drastic drop of the activity and selectivity to CO (FE going from 77% to 51% over 3 h) was observed for the immobilized unsubstituted iron porphyrin derivative without pendant OH groups.<sup>132</sup> A strong chemical binding of molecular catalysts to metal oxide surfaces may be also obtained.<sup>135</sup> For instance, a co-facial Fe porphyrin dimer was successfully immobilized as a monolayer ( $\approx 10^{-12}$  mol cm<sup>-2</sup>) on a fluorine-doped tin oxide (FTO) surface *via* a phosphonic acid anchoring group (Fig. 5c).<sup>136</sup> The FTO/Fe porphyrin assembly exhibited good electrocatalytic activity and stability for CO<sub>2</sub>-to-CO conversion in both non-aqueous and aqueous (pH 7.0) solutions. The immobilization

of the catalyst on a thin layer of SnO<sub>2</sub> or TiO<sub>2</sub> NPs on FTO increased the catalyst loading ( $\approx 10^{-9}$ – $10^{-10}$  mol cm<sup>-2</sup>), whereas the co-modification of the catalyst-free FTO surface with hydrophobic *n*-butyl phosphonic acid groups allowed to suppress the non-innocent behavior of the bare FTO electrode.

In some cases, the interaction of the porphyrin unit itself with the electrode surface was found to be strong enough to guarantee a stable functionalization without the need for a chemical modification of the ligand structure. For instance, the positively charged trimethylammonium molecular derivative **18**, was effectively anchored to a carbon support by simply drop-casting a suspension of the catalyst with the Nafion binder and carbon powder.<sup>137</sup> The modified electrode was integrated into a home-made electrolyzer for CO<sub>2</sub>/H<sub>2</sub>O splitting into CO/O<sub>2</sub> and was employed as a cathode for selective CO production (FE 90%) at neutral pH. The device showed good performances, providing an overall 50% energy efficiency and current densities of about 1 mA cm<sup>-2</sup> over 30 h electrolysis at a 2.5 V cell voltage.<sup>137</sup> In a recent report, a highly porous 3D hierarchical composite (FePGF) was fabricated by mixing complex **18** with reduced liquid crystalline graphene oxide (rLCGO), as a result of the agglomeration due to the  $\pi$ - $\pi$  stacking and electrostatic interactions between the positive charges on **18** and the negative charges of rLCGO (Fig. 5e).<sup>138</sup> The FePGF electrode (obtained by drop-casting a suspension of FePGF on a carbon support) showed an enhanced CO production and stability in comparison with the homogeneous derivative **18**. Moreover, the catalyst-graphene interaction contributed to improve the electron delocalization and facilitate the electron transfer, inducing a *ca.* 100 mV positive shift in the catalytic onset potential. At neutral pH and 430 mV overpotential ( $-0.54$  V vs. RHE), the FePGF electrode sustained a highly selective production of CO (FE 99%, TOF = 2.9 s<sup>-1</sup>, TON = 104 400) over 10 h electrolysis, with negligible formation of H<sub>2</sub>.<sup>138</sup> By a slight modification of this system, a simple and facile self-assembly hydrothermal method was developed to prepare a **18**-graphene hydrogel (FePGH) deposited on a reticulated vitreous carbon (RVC) support.<sup>139</sup> The FePGH/RVC electrode displayed similar performances as the FePGF/CFP system in terms of selectivity and long-term stability, but at a lower overpotential ( $-0.39$  V vs. RHE,  $\eta = 280$  mV).

In the attempt to increase the amount of catalyst incorporated in the thin film, modified Fe porphyrin complexes were used as structural and functional building blocks of porous hybrid architectures. Some Fe porphyrin-based MOF materials containing Zr<sub>6</sub> clusters as nodes were reported to be able to mediate CO<sub>2</sub>RR to CO in both organic and aqueous electrolytes. More specifically, the Fe-MOF-525 system produced a mixture of CO (FE 54%) and H<sub>2</sub> (FE 45%) in CH<sub>3</sub>CN solution,<sup>140</sup> whereas the PCN-222(Fe) MOF catalyst mixed with carbon black afforded a selective conversion of CO<sub>2</sub> to CO (FE<sub>CO</sub> 91%) in aqueous solution at  $-0.60$  V vs. RHE ( $\eta = 494$  mV).<sup>141</sup> Notably, the amount of electroactive Fe-TPP units deposited on the electrode surface in the Fe-MOF-525 catalyst is considerably higher than the conventional heterogenization methods.<sup>140</sup> A novel Fe porphyrin-based COF material, prepared by a straightforward solvent-free method, was also recently reported





Fig. 5 Different strategies for heterogenization of Fe porphyrin CO<sub>2</sub>RR catalysts on carbon-based electrodes. The panels show pictorial representations of the catalysts reported in the ref. 72 (a), 132 (b), 136 (c), 133 (d) and 138 (e), respectively. Figure a is adapted with permission from ref. 72. Copyright 2016, Royal Society of Chemistry. Figure b is adapted with permission from ref. 132. Copyright 2016, Royal Society of Chemistry. Figure c is adapted with permission from ref. 136. Copyright 2017 American Chemical Society. The figure e is adapted with permission from ref. 138. Copyright 2018, Wiley-VCH.

as a fairly stable catalyst for CO<sub>2</sub>RR, producing CO in good yields in organic media. Nevertheless, catalytic tests in aqueous conditions resulted in major H<sub>2</sub> production.<sup>142</sup> In addition to MOFs and COFs, supramolecular assemblies accommodating

iron porphyrin moieties served as competent catalysts for efficient CO production. In comparison with direct non-covalent functionalization of molecular FeTPP, its encapsulation into a rhombicuboctahedral porous organic cage (POC) substantially



increased the electroactive surface area, leading to superior catalytic rates and durability.<sup>143</sup> In neutral water, the supra-molecular catalyst was able to produce 55 250 turnovers of CO with FEs close to 100% at  $-0.63$  V vs. RHE ( $\eta = 510$  mV) over 24 hours. Remarkably, a kinetic analysis suggested that the porous POC framework enhances the catalytic response by facilitating CO<sub>2</sub> diffusion and increasing the local concentration of CO<sub>2</sub>, albeit not altering the catalytic mechanism of FeTPP at a molecular level.<sup>143</sup>

### 3.2 Cobalt

In contrast with the Fe analogues, the Co complexes bearing porphyrin-like ligands have received considerably less attention as homogeneous CO<sub>2</sub>RR catalysts in both organic and aqueous electrolytes.<sup>144–146</sup> Instead, they were found to be very efficient catalysts once immobilized on the surface of conductive carbon-based electrodes using a wide variety of functionalization strategies. Here we aim to focus on the molecular Co catalysts containing the most popular porphyrin and phthalocyanine moieties (see Chart 2). A comparative study between an immobilized Co phthalocyanine and other porphyrin-like Co-N<sub>4</sub> complexes highlighted that the former possesses an ideal platform for catalytic CO production, favoring the rapid formation of the key intermediate \*COOH and the desorption of CO.<sup>147</sup> These findings suggest that not only the metal

coordinative environment, but also the bulk structure of the ligand plays an important role in catalysis. A variety of other Co porphyrinoids have been proposed for CO<sub>2</sub>RR so far, including chlorins,<sup>148</sup> corroles<sup>149,150</sup> and corrins.<sup>151</sup> Among them, it is worth mentioning a Co<sup>II</sup> chlorin complex (22) adsorbed on MWCNTs, which was shown to be able to catalyse the CO<sub>2</sub>-to-CO electroreduction with high FE (89%) at low pH values.<sup>148</sup>

**3.2.1 Co porphyrin derivatives.** In a recent report, Daasbjerg and co-workers have systematically compared the electrocatalytic behaviour of the unmodified CoTPP complex (23) under CO<sub>2</sub> as homogeneous catalyst in DMF solution and as simply drop-casted on a CNT/GC electrode in aqueous electrolyte (0.5 M KHCO<sub>3</sub>), respectively (Fig. 6).<sup>152</sup> In organic media, CoTPP was found to be a poor catalyst under homogeneous conditions, due to the need for the formation of the catalytically active doubly reduced [Co<sup>0</sup>TPP]<sup>2-</sup> species at unfavorable overpotentials for CO<sub>2</sub>RR. At an applied voltage of  $-2.05$  V vs. SCE ( $\eta = 1120$  mV), 23 produced only a small amount of CO after 4 h electrolysis, corresponding to a *ca.* 50% FE and 3.8 turnovers (Fig. 6a). Besides H<sub>2</sub> (FE 2%), several CO<sub>2</sub>RR by-products were obtained in small amounts, including formate (4%), oxalate (0.4%) and acetate (2%). As indicated by cyclic voltammetry and UV-Vis measurements, a strong catalyst degradation was observed during long-term electrolysis. Conversely, the heterogenized molecular catalyst was capable to drive a selective CO<sub>2</sub> conversion to CO (FE 91%)



Chart 2 Selected molecular Co systems containing porphyrinoid structures reported for CO<sub>2</sub>RR.





**Fig. 6** Comparison of the  $\text{CO}_2\text{RR}$  catalytic behavior of CoTPP (**23**) as homogeneous catalyst in (a) organic medium (DMF), and (b) heterogenized catalyst supported on MWCNTs in aqueous electrolyte, respectively. (a) Current density recorded for an electrolysis at  $-2.05$  V vs. SCE at a GC plate on 1 mM CoTPP (**23**) in the presence of  $\text{CO}_2$  (left) and the ensuing production of CO and  $\text{H}_2$  (right). The electrolyte solution is 0.1 M  $n\text{-Bu}_4\text{NBF}_4/\text{DMF}$ . (b) Current density for a 4 h electrolysis at  $-1.35$  V vs. SCE with CoTPP–CNT on a GC plate ( $\Gamma = 1.7 \times 10^{-7}$  mol  $\text{cm}^{-2}$ ) in the presence of  $\text{CO}_2$ , and the ensuing production of CO and  $\text{H}_2$ . The electrolyte is 0.5 M  $\text{KHCO}_3$ . Adapted with permission from ref. 152. Copyright 2017, Wiley-VCH.

at a considerably lower overpotential ( $-1.35$  V vs. SCE,  $\eta = 550$  mV) than the homogenous counterpart (Fig. 6b). In agreement with previous DFT mechanistic studies, these results suggest that  $[\text{Co}^{\text{I}}\text{TPP}]^-$  is the catalytic species responsible for  $\text{CO}_2$  binding and activation.<sup>153,154</sup> Moreover, the heterogenization process improved substantially the catalyst stability, resulting in a 300 times higher activity ( $\text{TON}_{\text{CO}} = 1118$ ). These data clearly show the crucial role played by the catalyst support material in heterogeneous catalysis, and aspects such as its porosity and conductivity are of vital importance.<sup>155</sup> Several carbon-based materials have been used for the immobilization of Co porphyrins, including gas diffusion electrodes (GDE),<sup>156</sup> pyrolytic graphite (PG)<sup>51</sup> and reduced graphene oxide (rGO).<sup>157</sup> In the latter case, the carboxyl groups of the rGO film have been proposed to strongly interact with the cobalt [5,10,15,20-(tetra-*N*-methyl-4-pyridyl)porphyrin] (CoTMPyP, **24**) catalyst, inducing the formation of a hydride intermediate species that would be responsible for an unexpected non-negligible formate production.<sup>157</sup>

In addition to the interaction between the catalyst and the support, the pH is a crucial factor to control selectivity. A recent study of a Co protoporphyrin (**25**) immobilized on PG (CoPP/PG) revealed that small amounts of  $\text{CH}_3\text{OH}$  (**6e**) and  $\text{CH}_4$  (**8e**) can be formed in addition to CO in water at moderate overpotential (*ca.* 500 mV), being the product distribution highly dependent on pH.<sup>51</sup> In addition to gas-chromatographic measurements during electrolysis experiments, online electrochemical mass spectrometry (OLEMS) was used to detect the

gaseous products during slow voltammetric scans ( $1$  mV  $\text{s}^{-1}$ ). At pH 3, production of CO (major, FE  $\approx 40\%$ ) and  $\text{CH}_4$  (FE  $< 0.5\%$ ) was observed at less negative potentials than HER, whereas  $\text{H}_2$  is the dominant product at pH 1, with FEs below 1% for both CO and  $\text{CH}_4$  (traces of  $\text{HCOOH}$  and  $\text{CH}_3\text{OH}$  were also detected). In spite of the very low yields, the FE for  $\text{CH}_4$  was found to be slightly higher at pH 1, due to a fast CO reduction to  $\text{CH}_4$  occurring in these conditions simultaneous to HER. The pH-dependent  $\text{CO}_2\text{RR}$  behaviour of CoPP/PG is consistent with the DFT mechanism proposed for the simple Co porphyrin complex (CoP, **26**):<sup>154</sup> the initial  $[\text{Co}(\text{P})(\text{CO}_2)]^-$  formation, due to the  $\text{CO}_2$  binding by the active  $[\text{Co}^{\text{I}}(\text{P})]^-$  is followed by an intramolecular electron transfer which leads to a catalyst-bound  $\text{CO}_2^{\bullet-}$  radical anion. This adduct acts as a strong Brønsted base abstracting a proton by a water molecule to give the neutral  $[\text{Co}(\text{P})(\text{COOH})]^0$  intermediate. Then, the next neutral  $[\text{Co}(\text{P})(\text{CO})]^0$  carbonyl species can undergo either CO release or further reduction to  $\text{CH}_4$  through a series of concerted PCET steps.<sup>154</sup>

A fine-tuning of the electronic properties of the ligand scaffold is another key aspect to consider for the rational design of an optimal heterogeneous molecular catalyst for  $\text{CO}_2\text{RR}$ . Recently, a rigorous study on a series of immobilized Co porphyrin catalysts containing varying peripheral aryl substituents (**24**, **27–32**, Chart 2) showed that both inductive and electrostatic substituent effects impact the catalytic  $\text{CO}_2$  electro-reduction to CO in neutral aqueous media.<sup>158</sup> In order to



minimize the aggregation effects, the catalytic properties were probed at low catalyst loadings using  $\text{TOF}_{\text{CO}}$  as a descriptor of the  $\text{CO}_2\text{RR}$  activity. As a major finding, the  $\log \text{TOF}_{\text{CO}}$  was found to linearly increase with the electron-donating character of the substituent (lower Hammett parameter,  $\sigma$ ) across the series, in agreement with a rate-determining step involving an electron transfer from the Co center to  $\text{CO}_2$ . Furthermore, the immobilized Co complexes bearing cationic functionalities displayed an enhanced  $\text{CO}_2\text{RR}$  catalytic response, likely due to an additional electrostatic stabilization of the key intermediate (analogously to homogeneous Fe porphyrin catalysts in non-aqueous electrolyte<sup>112</sup>).

Several strategies for covalent attachment of Co porphyrins to carbon-based electrodes have been developed in alternative to the non-covalent approach (Fig. 7). In most cases, the molecular catalyst undergoes a chemical reaction or coordinates to specific functional groups or organic molecules introduced on the electrode surface. For instance, the functionalization of GC electrodes with 4-aminopyridine was obtained by direct anodic oxidation of the amine group (Fig. 7a)<sup>159</sup> or through the formation of an amide linkage (Fig. 7b).<sup>160</sup> The axial coordination of the pendant pyridine group to the unsubstituted CoTPP complex ensured a stable immobilization of the molecular catalyst on the surface. The so-formed catalytic films produced CO with moderate FEs ( $>50\%$ ) at  $-1.2$  V vs. SCE in phosphate buffer, corresponding to *ca.*  $10^5$  turnovers.<sup>160</sup> More recently, a robust covalent linkage of an alkyne-functionalized Co porphyrin to a boron-doped diamond electrode was achieved *via* a  $\text{Cu}^{\text{I}}$ -catalyzed

“click” reaction with superficial azide-terminal groups (Fig. 7c).<sup>73</sup> The  $\text{CO}_2\text{RR}$  process in  $\text{CH}_3\text{CN}$  was monitored by FTIR, providing evidence of a reductive disproportionation of  $\text{CO}_2$  into CO and  $\text{CO}_3^{2-}$ , even though the evolved products were not quantified. In another report, an unmodified protoporphyrin IX (25) was covalently grafted to the O-atoms of hydroxyl-functionalized CNTs by reflux in the presence of a tertiary amine (Fig. 7d).<sup>161</sup> In comparison with conventional physical methods, this procedure increased the catalyst loading, maintaining a high level of dispersion. In terms of  $\text{CO}_2\text{RR}$  performance, the modified electrode exhibited an excellent selectivity to CO (FE 98%) and durability ( $\text{TON}_{\text{CO}} = 6 \times 10^4$ ) at a 490 mV overpotential, with a stable current density of *ca.*  $25 \text{ mA cm}^{-2}$  over 12 hours. Recently, a direct electroreductive covalent grafting of a diazonium-modified CoTPP to carbon cloth also revealed to be an effective way to obtain high catalytic CO turnovers ( $3.9 \times 10^5$ ) and good selectivity (FE<sub>CO</sub> 81%) (Fig. 7e).<sup>162</sup> In this case, the  $\pi$ -conjugated phenylene linker contributes to enhance the electron transfer from the electrode to the attached molecular catalyst. Lastly, the electropolymerization of substituted Co porphyrins containing aminophenyl<sup>163</sup> or vinyl<sup>164</sup> groups also resulted in the formation of catalytic films for  $\text{CO}_2\text{RR}$ .

The reticulation of Co porphyrin-like molecular catalysts into porous networks has represented a significant step forward towards the design of new electrocatalytic materials for  $\text{CO}_2\text{RR}$ .<sup>76,78,165</sup> In a first example, a modified CoTPP was used as the catalytic linker unit assembled into a porous MOF structure, namely  $\text{Al}_2(\text{OH})_2\text{TCPP-Co}$  ( $\text{TCPP-H}_2 = 4,4',4'',4'''$ -(porphyrin-5,10,15,20-tetrayl)tetrabenzoate).<sup>76</sup>



Fig. 7 Different proposed strategies for covalent attachment of Co porphyrin catalysts for  $\text{CO}_2\text{RR}$ . Pictorial representation of catalysts reported in ref. 73 and 159–162.



In an attempt to maximize the amount of Co centres electrically connected to the electrode, thin films of MOF were grown directly on the surface, resulting in a sustained electrocatalytic conversion of aqueous CO<sub>2</sub> to CO with current selectivity up to 76% at  $-0.7$  V vs. RHE. By directly growing the MOF on a transparent conductive fluorine-doped tin oxide (FTO) plate, an estimation of the formal redox potential ( $E_{1/2}$ ) for the Co<sup>III/I</sup> transition was made by means of *in situ* UV-Vis spectroelectrochemistry.<sup>76</sup> Recently, the structure of 2D MOF nanosheets [TCPP(Co)/Zr-BTB] was reported to facilitate the exposure of the Co porphyrin active sites to CO<sub>2</sub>, showing comparable results as to Al<sub>2</sub>(OH)<sub>2</sub>TCPP-Co.<sup>166</sup> The post-modification of the unsaturated coordination sites of Zr<sub>6</sub> clusters with different organic molecules allowed to tune the microenvironment around TCPP(Co), favouring CO<sub>2</sub>RR over HER. Following another strategy, the combination of a Co porphyrin linker with a reductive polyoxometalate (POM) unit gave rise to a MOF electrocatalyst for CO<sub>2</sub>RR to CO with improved electrical properties, resulting in excellent FE<sub>CO</sub> (99%) and durability (>36 h) at  $-0.8$  V vs. RHE.<sup>167</sup>

A remarkable improvement in the catalytic performance was obtained by the incorporation of Co porphyrin building blocks into COF structures, whereby a dialdehyde organic linker is connected to the catalytic unit (5,10,15,20-tetrakis[(4-aminophenyl)porphinato]-cobalt, CoTAP) by imine condensation (Fig. 8).<sup>78</sup> Unlike MOFs, the presence of organic linkers offers the opportunity to easily tune the pore size and, in turn, the CO<sub>2</sub> adsorption properties of the material. In order to study this effect on CO<sub>2</sub>RR, 1,4-benzenedicarboxaldehyde (BDA) and biphenyl-4,4'-dicarboxaldehyde (BPDA) were employed as struts for the synthesis of two different COF materials, namely COF-366-Co and COF-367-Co, respectively. Albeit an excellent selectivity to CO (FE ca. 90%) was obtained for both catalysts in neutral aqueous conditions at  $-0.67$  V vs. RHE ( $\eta = 550$  mV), the latter exhibited an increased TON<sub>CO</sub> in comparison with COF-366-Co over a 24 h electrolysis period. The catalytic turnover of COF-367-Co was further improved by adopting a multivariate approach (>2.9 × 10<sup>5</sup> CO turnovers for COF-367-Co(1%)), consisting in diluting the electroactive Co porphyrin active sites in the lattice with isostructural metalloporphyrins that are catalytically inactive for CO<sub>2</sub>RR (e.g. Cu). It was also found that growing thin films of COFs on highly oriented pyrolytic graphite led to a 9-fold improvement in the catalytic activity of COF-366-Co over the microcrystalline COF powder deposited on a carbon fabric support, due to an improved electrical contact between the catalytic centers and the electrode.<sup>165</sup>

In addition to the physical properties of the COF material, the electronic effect exerted by the framework on the metal center was also investigated. Interestingly, the observation of an additional pre-edge feature in the X-ray absorption spectra (XAS) of the COF catalysts absent in the molecular CoTAP counterpart suggested that an electronic communication takes place between the lattice and the metal center.<sup>78</sup> To investigate the inductive effect of the framework in more detail, a series of COFs were prepared using struts with different electron-withdrawing or electron-donating groups. Even though the experimental trend deviates from the expected order based on

basic inductive effect considerations, XAS and CV measurements showed clear differences across the series, providing a direct observation of the effect of the framework functionalization on the metal center.<sup>165</sup>

Besides the electronic effect related to the framework, reticular materials are ideal systems to investigate the role of secondary interactions on catalysis, offering the opportunity to tune the local microenvironment of molecularly defined catalytic sites. The boosting effect of such interactions on CO<sub>2</sub>RR electroreduction in aqueous media was recently demonstrated for Co protoporphyrin (CoPP) molecular units immobilized on 2D metal-organic layer (MOL) scaffolds (Fig. 9).<sup>168</sup> Following a post-synthetic approach, CoPP moieties were incorporated into two different MOL backbone derivatives, built from benzene-tribenzoate (BTB) and 4'-(4-benzoate)-(2,2',2''-terpyridine)-5,5''-dicarboxylate (TPY) linkers, respectively. In the TPY-MOL-CoPP material, the pyridine/pyridinium pendant groups adjacent to the CoPP active sites were found to engage a cooperative synergistic boosting effect on catalysis (Fig. 9a), resembling the second or outer coordination sphere effects above discussed for the homogeneous heme catalysts (see Section 3.1.1). In particular, the presence of pendant pyridine residues resulted in a significant improvement of the CO<sub>2</sub>RR selectivity over HER for TPY-MOL-CoPP (FE<sub>CO</sub> > 90%,  $j_{CO}/j_{H_2} = 11.8$ ) in comparison with the BTB-MOL-CoPP derivative containing only phenyl rings ( $j_{CO}/j_{H_2} = 2.7$ ), Fig. 9b. The crucial role of the preassembled pyridine/pyridinium groups was demonstrated by the FE<sub>CO</sub> decay observed upon addition of divalent cations (Ca<sup>2+</sup> or Zn<sup>2+</sup>) to the solution, due to the blockage of the terpyridyl units. Moreover, a possible electronic effect of axial coordination of the pendant pyridine rings was ruled out by the low faradaic yields obtained upon addition of exogenous pyridine. Notably, during reduction of TPY-MOL-CoPP under CO<sub>2</sub> (pH 6.8), *in situ* electrochemical diffuse reflectance infrared Fourier transform spectroscopy (DRIFTS) provided evidence of pyridine protonation to form pyridinium units (increasing band at 1438 cm<sup>-1</sup>), while these spectral changes were not observed under N<sub>2</sub> neither with BTB-MOL-CoPP under CO<sub>2</sub> (Fig. 9c).<sup>168</sup> DFT calculations suggested that the pyridinium moieties of the framework exert a cooperative boosting effect by lowering the energy barrier for both, CO<sub>2</sub> adsorption and C-O bond cleavage, the latter being the rate-determining step of the process. The proposed mechanism is analogous to the one above mentioned for the Co porphine system,<sup>154</sup> whereby the one-electron reduction of CoPP to [CoPP]<sup>-</sup> is followed by CO<sub>2</sub> binding and protonation steps, leading to the formation of the key [pyH-O<sub>2</sub>C-Co(PP)]<sup>0</sup> adduct, stabilized by a pre-positioned pyridine moiety to favor CO<sub>2</sub>RR over HER. A second electron uptake is then followed by the C-O bond cleavage to form the [Co(PP)(CO)]<sup>0</sup> species which undergoes CO release.<sup>168</sup>

Finally, the efficiency of electron transport to the catalytic site is a crucial limiting factor to the usage of reticular systems for efficient CO<sub>2</sub>RR.<sup>33</sup> In this regard, the incorporation of electron carriers as building blocks of the framework has revealed to be an effective strategy to improve electron migration in COFs. For instance, crystalline COFs obtained through



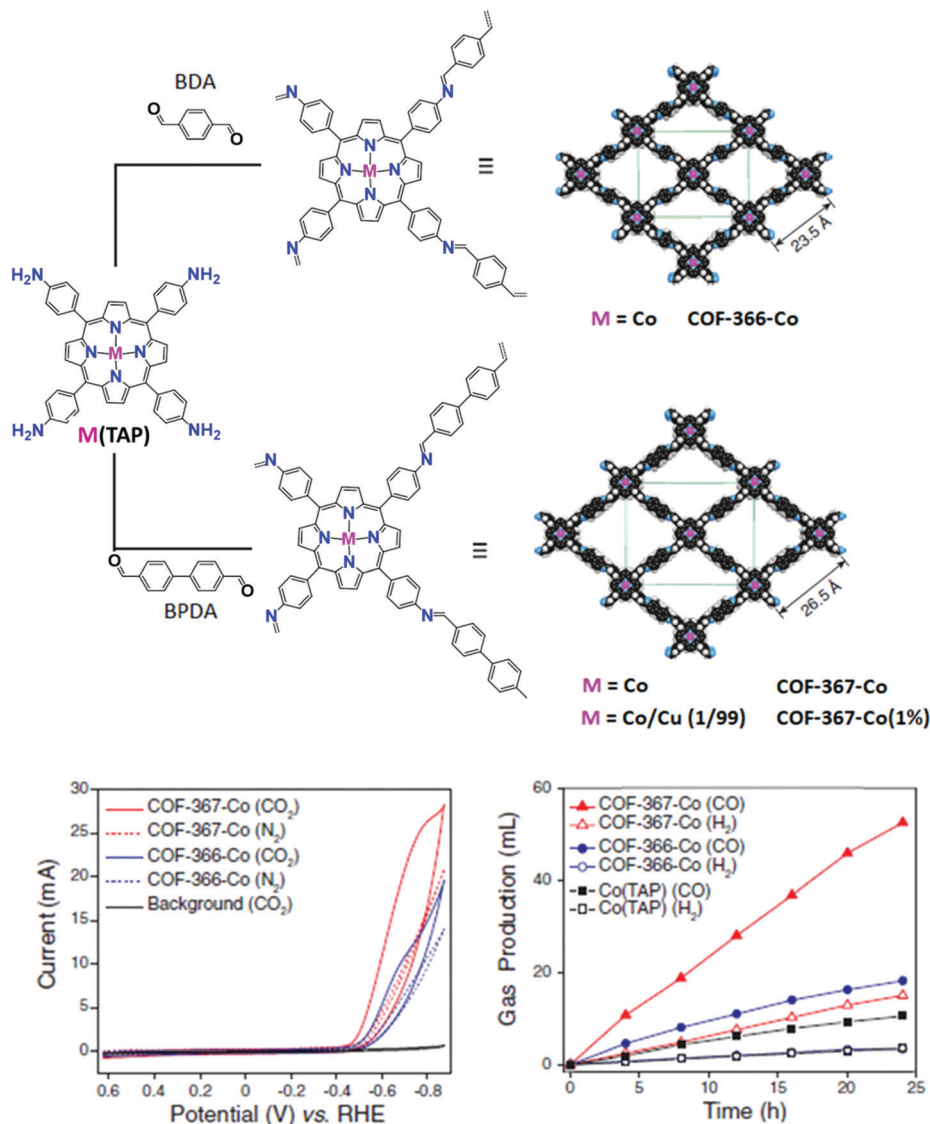


**Fig. 8** Design and synthesis of metalloporphyrin-derived 2D covalent organic frameworks reported in ref. 78. The space-filling structural models of COF-366-M and COF-367-M were obtained using Materials Studio 7.0 and refined with experimental PXRD data. Bottom left: Cyclic voltammograms of COF-366-Co and COF-367-Co in a CO<sub>2</sub>-saturated medium (blue and red solid lines, respectively) or N<sub>2</sub>-saturated medium (blue and red dotted lines, respectively). The black solid line shows background (bare carbon electrode) CV responses in the CO<sub>2</sub>-saturated medium. The medium was pH 7.2 aqueous potassium phosphate buffer (0.2 M) with additives: 0.5 M KHCO<sub>3</sub> under CO<sub>2</sub> atmosphere to maintain a neutral pH, or 0.5 M NaClO<sub>4</sub> under N<sub>2</sub> atmosphere to match the ionic strength. Bottom right: Long-term bulk electrolyses at  $-0.67$  V (vs. RHE), showing the volume of CO produced by COF-367-Co (red solid triangles), COF-366-Co (blue solid circles), or Co(TAP) (black solid squares) and the volume of H<sub>2</sub> produced by COF-367-Co (red open triangles), COF-366-Co (blue open circles), or Co(TAP) (black open squares). Adapted with permission from ref. 78. Copyright 2015, American Association for the Advancement of Science.

the assembly of Co porphyrin catalytic units and tetrathiafulvalene struts, serving as an electron donors, resulted in enhanced durability, activity and selectivity to CO.<sup>79,169</sup> Moreover, the exfoliation of bulk COFs into 2D ultrathin nanosheets (*ca.* 5 nm thickness) led to further improved CO<sub>2</sub>RR performances compared to the unexfoliated COF material, resulting in excellent CO selectivity in a wide potential range.<sup>79</sup>

**3.2.2 Co phthalocyanine derivatives.** In an early report, Co phthalocyanine (CoPc, **33**) adsorbed on graphite electrodes was investigated as a catalyst for CO<sub>2</sub>RR in aqueous solution.<sup>170</sup> Analogously to Co porphyrins,<sup>152</sup> CoPc has been reported as a

poor electrocatalyst for CO<sub>2</sub>RR in homogeneous conditions. In contrast, the immobilization of CoPc onto a carbon-based electrode leads to a sustained CO<sub>2</sub> conversion in aqueous conditions, forming CO as a major product.<sup>171</sup> Taking advantage of the strong  $\pi$ - $\pi$  stacking interaction between cobalt phthalocyanines and carbonaceous materials, straightforward dip-coating or drop-casting methods are the most popular deposition techniques to attach the catalyst on a carbon support.<sup>170-175</sup> A recent study highlighted the effect of catalyst loading ( $5 \times 10^{-12}$ – $1 \times 10^{-7}$  mol cm<sup>-2</sup>) and dispersion on the CO<sub>2</sub>RR activity of a CoPc catalyst drop-casted on oxygen-functionalized carbon paper.<sup>176</sup>





**Fig. 9** (a) Schematic showing the structure of the TPY-MOL-CoPP and the cooperative activation of CO<sub>2</sub> by CoPP and pyH<sup>+</sup>. (b) FE for CO and H<sub>2</sub> at varying electrolysis potentials for different catalysts in CO<sub>2</sub>-saturated 0.1 M NaHCO<sub>3</sub>. (c) On the left it is shown a schematic of the thin-layer IR cell for the *in situ* DRIFTS measurements. On the right, the IR spectrum of TPYH<sup>+</sup>-MOL (pH 4.0 with HClO<sub>4</sub>, red line), and DRIFTS of TPY-MOL-CoPP in the potential scan range of -0.06 to -0.86 V vs. RHE in a CO<sub>2</sub>-saturated aqueous solution of 0.1 M NaHCO<sub>3</sub>. The reference spectrum was taken at 0.14 V vs. RHE. Adapted with permission from ref. 168. Copyright 2019 American Chemical Society.

As a general trend, the FE for CO production slightly decreased upon reducing the loading of the catalyst (from 96% to 80% across the series), likely due to a more pronounced exposure of the carbon paper support, which is able to catalyse HER. However, low loadings and high dispersion levels contribute to mitigate transport limitations and to avoid the formation of aggregates or stacking phenomena, thus providing a substantial increase in the TOF. The hybridization with carbon nanotubes is also reported to minimize CoPc aggregation in many cases.<sup>177</sup> Besides the catalyst loading and the specific catalyst-support interaction, the stability of the system can be improved by introducing suitable modifications to the ligand framework. The presence of sterically hindered long alkoxy chains (34) on the phthalocyanine backbone constituted an effective strategy to contrast CoPc aggregation on graphene sheets, leading to better CO<sub>2</sub>RR performances.<sup>178</sup> A limited formation of aggregates was also obtained for robust Co polyphthalocyanine thin films on MWCNTs synthesized *via* an *in situ* microwave-assisted template-directed method.<sup>179</sup> Other approaches based on single-pot hydrothermal<sup>180</sup> or solid-state<sup>181</sup> polycondensation of CoPc-type catalysts, as well as direct electro-polymerization methods<sup>182</sup> have also been reported.

The functionalization of the CoPc structure with electron-withdrawing substituents displayed beneficial effects on catalysis. For example, a perfluorinated CoPc complex (35) adsorbed on carbon cloth served as a robust catalyst for simultaneous CO<sub>2</sub>/CO conversion and H<sub>2</sub>O/O<sub>2</sub> splitting.<sup>183</sup> At the cathode, 35 was able to produce CO with high selectivity (FE 93%) at -0.8 V vs. RHE at neutral pH. It has been hypothesized that the fluorine substituents not only induce a positive shift of the Co<sup>III/I</sup> redox potential, but also facilitate the CO release step, thus accelerating the product removal and catalytic turnover. An analogous enhancing catalytic effect was observed by introducing -CN groups to the CoPc molecule (Fig. 10). The CN-functionalized CoPc complex (36) supported on MWCNTs exhibited higher CO selectivity at a lower overpotential than the parent CoPc catalyst, producing CO in high yields (FE 98%) and current densities ( $\approx 15 \text{ mA cm}^{-2}$ ) at -0.63 V vs. RHE ( $\eta = 520 \text{ mV}$ ) at near-neutral pH.<sup>184</sup> The preparation method and the use of MWCNTs had a positive impact on the CO<sub>2</sub>RR activity, ensuring uniform and robust catalyst distribution on the electrode. Notably, a 36/CNT cathode was successfully implemented in a microflow cell with





Fig. 10 Comparison of the CO<sub>2</sub>RR performances of CoPc (**33**) and the CN-functionalized derivative **36** anchored to a MWCNT electrode in aqueous electrolyte (0.1 M KHCO<sub>3</sub>). Chronoamperograms (top right) and FEs (bottom right) of CO<sub>2</sub>RR products at different potentials for CoPc-CN/CNT (solid line) in comparison with CoPc/CNT (dotted line). Adapted with permission from ref. 184. Copyright 2017, Nature Publishing Group.

a CoO<sub>x</sub>/CNT anode, sustaining a selective CO production (FE 94% with  $j_{\text{CO}} = 31 \text{ mA cm}^{-2}$ ) at a cell voltage of 1.9 V in 1 M KOH aqueous electrolyte.<sup>185</sup> A stable CO evolution (FE  $\approx$  90%) was observed for 10 h at a constant cell voltage of 2.0 V.

Another remarkable example of high-performance heterogeneous catalyst for CO<sub>2</sub>-to-CO conversion is represented by a novel Co complex bearing a trimethylammonium group and three *tert*-butyl substituents installed on the phthalocyanine moiety (**37**) (Chart 2).<sup>186</sup> The structure of the latter is reminiscent of the highly active Fe porphyrin systems containing positively charged pendant groups.<sup>112,137–139</sup> Remarkably, porous films of **37** with carbon black or MWCNTs on carbon paper showed an excellent stability and nearly quantitative selectivity to CO in a wide range of pH (4–14). At neutral pH, **37** was found to outperform CoPc (**33**), resulting in an average current density of *ca.* 18 mA cm<sup>-2</sup> for CO production (93% selectivity) at  $-0.676 \text{ V vs. RHE}$  ( $\eta = 539 \text{ mV}$ ). Even more importantly, **37** provided excellent results once supported on a gas-diffusion cathode and used in a flow cell setup under alkaline conditions (1 M KOH): at a very low overpotential ( $-0.3 \text{ V vs. RHE}$ ,  $\eta = 200 \text{ mV}$ ) a  $j_{\text{CO}} = 22.2 \text{ mA cm}^{-2}$  was obtained, while reaching an impressive maximum partial current density of 165 mA cm<sup>-2</sup> at  $-0.92 \text{ V vs. RHE}$  ( $\eta = 810 \text{ mV}$ ) (Fig. 11).<sup>186</sup> In a related work, the readily available, low-cost parent CoPc complex (**33**) was able to sustain a selective CO<sub>2</sub>-to-CO conversion at 50 mA cm<sup>-2</sup> for >100 hours in a flow reactor.<sup>187</sup> The implementation of **33** in a tandem flow cell with a Ni foam OER catalyst led to an excellent selectivity for CO production at commercially relevant current densities ( $\geq 150 \text{ mA cm}^{-2}$ ). Furthermore, the FE<sub>CO</sub> drop observed upon increasing the current density from 150 to 200 mA cm<sup>-2</sup> was due to a depletion in proton concentration, rather than to a real degradation of the molecular catalyst. Indeed, a FE<sub>CO</sub>  $\approx$  88% was maintained at 200 mA cm<sup>-2</sup>

upon the addition of PhOH during the preparation of the catalyst ink.<sup>187</sup> The latter may also act as a local pH buffer, alleviating the issues related to precipitation of insoluble KHCO<sub>3</sub> crystals at the cathode. This improvement led to an overall cell voltage of *ca.* 2.5 V, outperforming an Ag solid-state CO<sub>2</sub>RR catalyst at a comparable CO partial current density.<sup>188</sup> These results demonstrate that earth-abundant metal-based molecular catalysts can be efficiently implemented in real devices for selective CO<sub>2</sub> conversion to CO.

Besides the outstanding stability and efficiency for CO production, their extreme versatility is another attractive feature of Co phthalocyanines. Very recently, it has been demonstrated that CoPc/MWCNT electrodes are able to catalyse the electrochemical CO<sub>2</sub> reduction to CH<sub>3</sub>OH in aqueous media *via* a CO intermediate.<sup>52</sup> Electrolyses performed under CO-saturated and highly basic (pH 13) conditions reached a FE  $\approx$  14% for CH<sub>3</sub>OH production at  $-0.64 \text{ V vs. RHE}$  ( $\eta = 740 \text{ mV}$ ). In addition to CH<sub>3</sub>OH, a small amount (*ca.* 3%) of formaldehyde, HCHO, was also detected in solution after an electrolysis under CO at  $-0.54 \text{ V vs. RHE}$ . In strongly alkaline conditions, a non-faradaic disproportionation of HCHO to a mixture of CH<sub>3</sub>OH and HCOO<sup>-</sup> (Cannizzaro reaction) may occur in solution and it should be considered.<sup>189</sup> In order to demonstrate that the Cannizzaro reaction accounts only for a small part of the detected CH<sub>3</sub>OH after electrolysis under CO, the ratios CH<sub>3</sub>OH/HCOO<sup>-</sup> were calculated to be 16 and 27 at pH 13 and 12, respectively. Furthermore, an electrolysis experiment under Ar in the presence of HCHO led to a considerable amount of CH<sub>3</sub>OH (FE > 18%) at  $-0.54 \text{ V vs. RHE}$ , confirming that HCHO is an intermediate for CH<sub>3</sub>OH formation. These findings open the door to a new sequential two-step CO<sub>2</sub>RR strategy for fuels production using the same CoPc molecular catalyst: at neutral pH, CoPc can efficiently and selectively convert CO<sub>2</sub> into CO, which can be



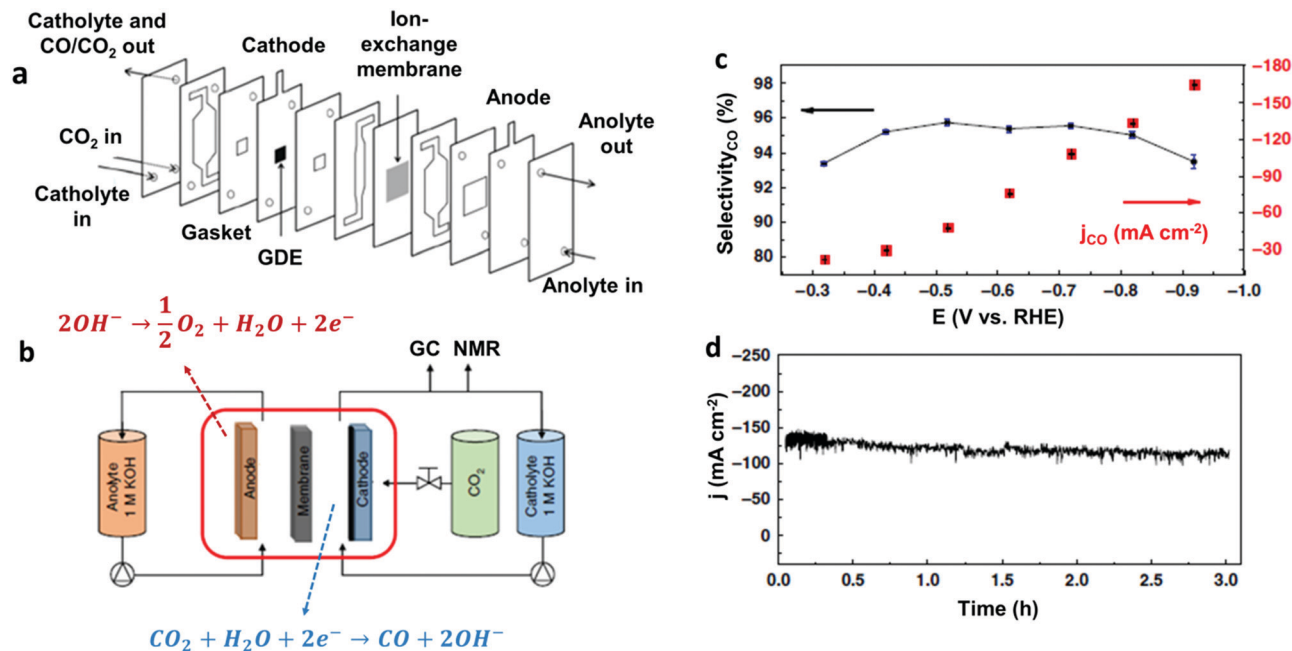


Fig. 11 (a) Cross-sectional view of the CO<sub>2</sub> electrolyzer flow cell and (b) general scheme of the entire experimental set-up used in ref. 186. (c) Current density (right) and selectivity for CO production (left) as a function of the potential, and (d) bulk electrolysis at a fixed potential ( $E = -0.72$  V vs. RHE) for **37**@carbon black deposited onto a carbon paper as cathodic material, in 1 M KOH. Adapted with permission from ref. 186. Copyright 2019, Nature Publishing Group.

further reduced to CH<sub>3</sub>OH using the same catalyst under basic conditions (pH 12–13). The capability of the immobilized molecular CoPc system to catalyse multi-electron CO<sub>2</sub>RR has been further confirmed by a recent study, whereby a CoPc/CNT composite was found to convert CO<sub>2</sub> to CH<sub>3</sub>OH with FE > 40% at  $-0.94$  V vs. RHE in a near-neutral electrolyte.<sup>53</sup> The major drawback relies in the low durability of the system, likely due to a partial hydrogenation of the Pc ligand, causing a dramatic drop of the CH<sub>3</sub>OH production after a few hours of electrolysis. However, the introduction of four amino groups onto the Pc moiety resulted in a substantial improvement of the catalyst (compound **38**, Chart 2) robustness, leading to a sustained production of CH<sub>3</sub>OH with average FE ca. 28% for 12 h of electrolysis.

In alternative to non-covalent functionalization methods, CoPc can be effectively anchored to a carbon-based electrode surface *via* the incorporation within a deposited layer of a coordination polymer such as poly-4-vinylpyridine (P4VP) (Fig. 12).<sup>190,191</sup> The dangling-free pyridyl groups act as the anchoring points for CoPc through an axial coordination to the Co center (Fig. 12a). In acidic conditions, the CoPc-P4VP electrode is a competent catalyst for the selective CO production (FE ≈ 90%) at  $-0.73$  V vs. RHE ( $\eta = 610$  mV), outperforming the parent CoPc system.<sup>192</sup> The catalytic boosting effect of pyridine coordination on CoPc has been also reported elsewhere.<sup>193</sup> Two major parameters were found to affect the catalytic response: (i) the axial coordination of pyridine (primary coordinative environment), which increases the nucleophilicity of the Co<sup>I</sup> center facilitating the CO<sub>2</sub> binding step; (ii) the interaction with partially protonated peripheral pyridyl residues of the polymeric film that may undergo secondary coordination sphere

effects (*e.g.* stabilizing H-bonding interactions, proton relays), as previously seen for a Co porphyrin catalyst incorporated into a MOF structure (see Section 3.2.1).<sup>192</sup> In order to evaluate these factors independently from each other, the electrocatalytic CO<sub>2</sub>RR behaviour of CoPc and CoPc-P4VP was systematically compared with the following three systems (Fig. 12b): the five-coordinate CoPc(py), in the absence of the P4VP membrane; CoPc encapsulated into a non-coordinating poly-2-vinylpyridine layer (CoPc-P2VP), whereby the axial coordination of the pyridine is prevented by steric hindrance; the five-coordinate CoPc(py)-P2VP, derived by embedding CoPc(py) within the P2VP polymer.<sup>192</sup> A detailed kinetic analysis highlighted a change in the rate determining step across the series, corresponding to the CO<sub>2</sub> binding step for the four coordinate derivatives (CoPc, CoPc-P2VP) and to a subsequent protonation of the coordinated CO<sub>2</sub> intermediate for the five-coordinated systems (CoPc(py), CoPc-P4VP, CoPc(py)-P2VP), confirming the pivotal role of the secondary proton relays in controlling the proton delivery to the CoPc active sites.<sup>194</sup> Other surface functionalities than the pyridyl groups may also contribute to enhance the catalytic properties of CoPc-type species. For example, the preferential immobilization of planar Co 2,3-naphthalocyanine (**39**) on doped graphene *via* axial Co–O coordination to the terminal sulfoxide groups rather than to the carboxyl ones, improved the electronic communication between the catalyst and the conductive surface, leading to a 3-fold increase of TOF for CO production and a FE up to 97%.<sup>195</sup>

Finally, Co phthalocyanine derivatives have been employed to design new hierarchical 3D materials for efficient CO<sub>2</sub>RR. In a recent report, Co phthalocyanine catechol building blocks have been implemented into a novel metal–catecholate





**Fig. 12** (a) An illustration of a cobalt phthalocyanine (CoPc) encapsulated within a hydrophobic poly-4-vinylpyridine (P4VP) membrane highlighting the postulated primary-, secondary-, and outer-coordination sphere effects.<sup>192,194</sup> (b) Selected catalyst and polymer-catalyst composite systems investigated in ref. 192 and 194 along with their postulated coordination environment and proton relays. Adapted with permission from ref. 194. Copyright 2019, Nature Publishing Group.

framework, namely MOF-1992.<sup>196</sup> The system displayed an original topology with more accessible CoPc sites, as well as improved charge transfer properties, leading to significantly higher electroactive surface area than the previously reported reticular Co/Fe catalysts.<sup>76,78,140,141,165</sup> At neutral pH, MOF-1992 was able to mediate a selective conversion of CO<sub>2</sub> to CO (FE 80%) at  $-0.63$  V vs. RHE ( $\eta = 520$  mV) with relevant current densities ( $> 16$  mA cm<sup>-2</sup>). Among the other proposed reticular or supramolecular approaches, it is worth to mention a hybrid approach, based on the decoration of the external surface of the zeolite ZIF-90 with active Co tetraminonaphthalocyanine units for selective CO<sub>2</sub>-to-CO conversion.<sup>80</sup> In this case, the electronic structure of the Co center was not altered by the zeolite framework.

### 3.3 Other transition metals

**3.3.1 Porphyrin derivatives.** Metalloporphyrinoids containing other transition metals than Fe or Co have received much less attention as catalysts for CO<sub>2</sub>RR. In an early report, homogeneous solutions of Pd and Ag porphyrins produced traces of oxalate upon electrolysis under CO<sub>2</sub> in aprotic media, suffering from severe deactivation likely due to partial demetalation.<sup>197</sup> Koper and co-workers investigated the influence of the metal center on the CO<sub>2</sub>RR to HCOOH in a series of heterogenized metalloprotoporphyrin catalysts immobilized on pyrolytic graphite in aqueous media.<sup>198</sup> Two main trends became apparent across the series: metals such as Cr, Mn, Co and Fe did not produce any observable amount of HCOOH at pH 3. On the contrary, the Ni-, Pd-, Ga-, Cu-, Sn-, In- and Rh-based systems showed variable amounts of HCOOH depending on pH and applied potential. A maximum FE<sub>HCOOH</sub> of ca. 70% was achieved for the In derivative at pH 9.6 and  $-1.9$  V vs. RHE. A later theoretical study suggested that the

nature of the electrogenerated nucleophilic species interacting with the substrate primarily controls the selectivity for CO<sub>2</sub>RR to CO or HCOOH in the series.<sup>199</sup> Accordingly to the proposed model, CO can be formed only by metal-electroactive metalloporphyrins, in which the nucleophilic metal center is able to bind CO<sub>2</sub> to form a metal-carboxylate intermediate. Conversely, HCOOH is triggered by the formation of a hydride donor species, which may be a metal hydride or a hydridic phlorin ligand (protonation of the *meso* carbon of the porphyrin). In this scenario, metal-electroactive metalloporphyrins (*e.g.* Fe, Co, Rh) are suitable catalysts for CO or HCOOH depending on the external conditions. It is worth noting that the homogeneous FeTPP catalyst was found to convert CO<sub>2</sub> into formate in high faradaic yields in the presence of an excess of tertiary amines (high pH) in an organic electrolyte *via* an alternative pathway not involving the formation of a metal hydride (Section 3.1.1).<sup>106</sup> On the other hand, ligand-electroactive metalloporphyrins (*e.g.* Ni, Zn, Cu, Pd, Ag, Cd, Ga, In, Sn) are predicted to be potential catalysts for selective CO<sub>2</sub> reduction to HCOOH *via* the hydride donor phlorin ligand pathway. Nevertheless, some reported Cu and Zn porphyrin systems deviate from the aforementioned predictions, producing CO with high FEs.<sup>200,201</sup> An *in situ* restructuring of the original molecular species under reducing conditions or the specific interaction with substituents to the porphyrin moiety have been invoked to explain the unexpected behaviour.<sup>199</sup> It is worth noting that a synthetic Zn bacteriochlorin has been recently reported as a robust catalyst for selective CO production in DMF/H<sub>2</sub>O mixture without any evidence of catalyst degradation.<sup>202</sup> Moreover, a number of extrinsic factors including the nature of the support material, its pre-treatment or the encapsulation of the molecular catalyst in polymer matrices may affect the CO<sub>2</sub>RR selectivity, reactivity and stability of metalloporphyrins.<sup>203</sup>



**3.3.2 Phthalocyanine derivatives.** Carbon monoxide (Co, Fe, Ni, Pd) and formic acid (Sn, Pb, In, Zn, Al) are the most common products reported for CO<sub>2</sub>RR mediated by metal phthalocyanines.<sup>175</sup> Nevertheless, comparative studies on a series of phthalocyanine model catalysts containing different metals (Co, Fe, Mn, Ni, Cu), showed that the Co derivative clearly outperformed the other counterparts in terms of efficiency, stability and selectivity to CO.<sup>204</sup> DFT calculations suggest that the optimal CO<sub>2</sub>RR activity of the latter is related to its favourable properties for \*COOH formation and \*CO desorption. In comparison with the direct loading of molecular catalysts on the electrode, CNT hybridization revealed to be an effective strategy to boost the CO<sub>2</sub>-to-CO conversion catalytic performances of Co, Fe and Mn phthalocyanine catalysts, being the Co counterpart still the most active across the series.<sup>177</sup> Recent examples of efficient and selective molecular catalysts based on Cu<sup>205,206</sup> and Ni<sup>207</sup> phthalocyanine catalysts have been also recently reported for selective CO<sup>206,207</sup> or CH<sub>4</sub><sup>205</sup> production in aqueous media.

## 4. Molecular catalysts for CO<sub>2</sub>RR containing non-heme macrocyclic and polydentate nitrogen ligands

In this section, the most relevant molecular systems based on non-heme macrocyclic and polydentate nitrogen ligands will be reviewed. We will focus on Fe, Co and Ni systems, which cover the majority of the molecular catalysts with this type of ligands reported so far for CO<sub>2</sub> electroreduction. Section 4.1 is devoted to the discussion of the widely studied Ni<sup>II</sup> and Co<sup>II</sup> tetraazamacrocyclic complexes. The main molecular catalysts with alternative nitrogen-containing macrocyclic frameworks will be

summarized in Section 4.2. Finally, Section 4.3 briefly summarizes some relevant recent studies carried out on molecular systems based on macrocyclic-like nitrogen ligands, comprising aminopyridyl, polypyridyl and tripodal N<sub>4</sub> systems.

### 4.1 Tetraazacyclam macrocycles

**4.1.1 Nickel.** The activity of molecular Ni complexes bearing N<sub>4</sub> macrocyclic ligands towards CO<sub>2</sub>RR was first documented by Fisher and Eisenberg in 1980.<sup>208</sup> A few years later, Sauvage and co-workers published a series of studies reporting the outstanding ability of the [Ni(cyclam)]<sup>2+</sup> complex (**40**, see Chart 3) (cyclam = (1,4,8,11-tetra-azacyclotetradecane)) to drive an efficient CO<sub>2</sub> electroreduction to CO in water.<sup>209–211</sup> Although its electrocatalytic behaviour is not fully understood yet, this system has been widely studied over more than 30 years, representing a milestone in the field of molecular catalysis for electrochemical CO<sub>2</sub> reduction. It displays excellent performance in water in terms of activity, selectivity and durability over a wide range of pH, being able to selectively produce high turnover numbers (TONs) of CO in acidic media (pH = 4–5) on a Hg pool electrode at –1.00 V vs. NHE.<sup>210</sup> For this system, a drastic current increase is observed in correspondence of the Ni<sup>III/I</sup> wave, suggesting an active role of the Ni<sup>I</sup> species in the catalysis (Fig. 13). However, the catalytic behavior of **40** is extremely sensitive to several experimental factors, including the electrode material. Exceptional performances were obtained by using a Hg working electrode, owing to the strong adsorption of the electrogenerated [Ni(cyclam)]<sup>+</sup> species on the electrode surface.<sup>212</sup> This is consistent with the huge (*ca.* 300 mV) positive shift observed for the potential of the Ni<sup>III/I</sup> wave under CO<sub>2</sub> and with the presence of a pre-wave just before the catalytic wave (Fig. 13). Moreover, the catalytic current was found to reach a plateau at increasing catalyst concentration, suggesting an adsorption saturation on the electrode surface.<sup>210</sup> Albeit with

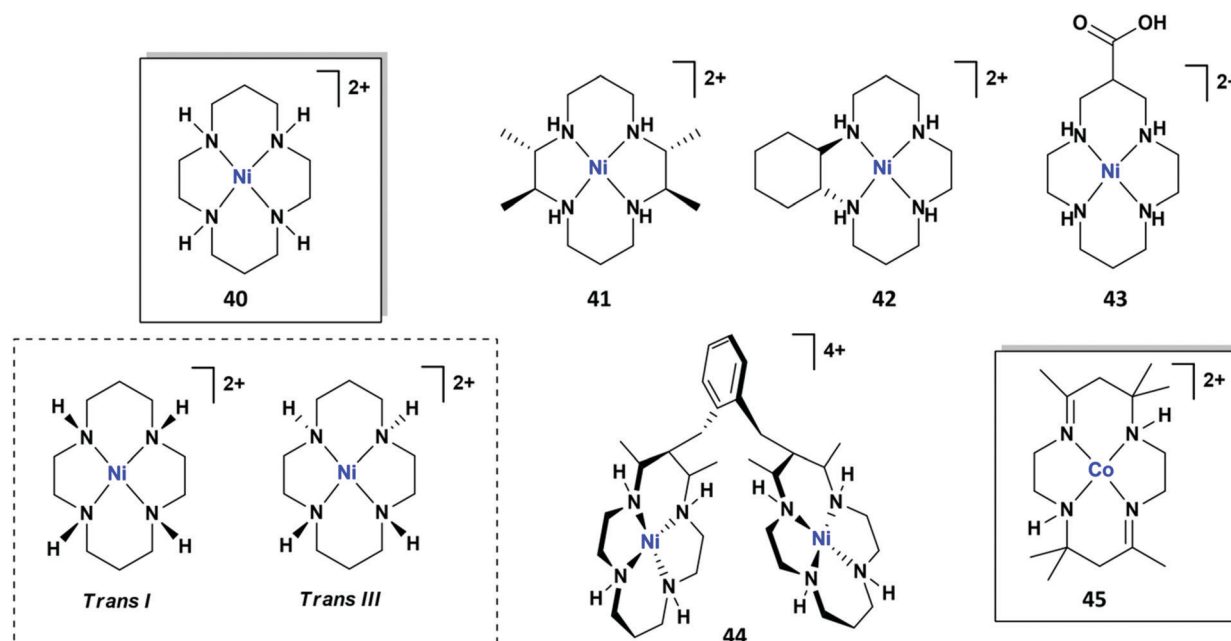


Chart 3 Structures of selected molecular Ni and Co tetraazamacrocycles reported for CO<sub>2</sub>RR.





Fig. 13 Cyclic voltammetry of  $[\text{Ni}(\text{cyclam})]^{2+}$  (**40**, 1 mM) in 0.1 M  $\text{KClO}_4$  (pH 4.5) under  $\text{N}_2$  (curve a) or  $\text{CO}_2$  (curve b) on a hanging Hg electrode. Scan rate:  $0.1 \text{ V s}^{-1}$ . Reprinted with permission from ref. 210. Copyright 1986 American Chemical Society.

slower catalytic rates, more recent experiments on glassy carbon electrodes confirmed that **40** may also act as a purely homogeneous catalyst for selective  $\text{CO}_2\text{RR}$  to  $\text{CO}$ , with  $\text{CO}$  FE close to 90% at  $-1.30 \text{ V vs. NHE}$  in an aqueous  $\text{KCl}$  solution or in a  $\text{CH}_3\text{CN}:\text{H}_2\text{O}$  4:1 mixture.<sup>213</sup>

The exclusive selectivity of **40** toward  $\text{CO}_2\text{RR}$  over  $\text{H}_2$  evolution in water has been attributed to the unfavorable formation of the  $[\text{Ni}(\text{H})(\text{cyclam})]^{2+}$  hydride intermediate ( $\text{p}K_{\text{a}} \sim 1.8$ ) in the operating pH conditions ( $\text{pH} \sim 4$ ).<sup>214</sup> In the proposed mechanism for  $\text{CO}_2$  conversion to  $\text{CO}$  mediated by **40** (Scheme 2), the electrogenerated  $[\text{Ni}(\text{cyclam})]^+$  species readily adsorbs on the electrode surface, undergoing  $\text{CO}_2$  binding to form a  $[\text{Ni}(\text{CO}_2)(\text{cyclam})]^+$  adduct in a  $\eta^1\text{-CO}_2$  binding mode.<sup>215</sup> Analysis of the molecular orbitals suggests that the electronic structure of this intermediate can be described by the  $\text{Ni}^{\text{I}}\text{-CO}_2^0 \leftrightarrow \text{Ni}^{\text{II}}\text{-CO}_2^{\bullet-}$  resonance forms, featuring only moderate metal-to-ligand charge transfer from the nucleophilic Ni center to the bound  $\text{CO}_2$ . The moderate affinity of the  $[\text{Ni}(\text{cyclam})]^+$  species for  $\text{CO}_2$  binding is consistent with the relatively low values of the  $\text{CO}_2$  binding constant ( $K_{\text{CO}_2} \sim 10^0\text{-}10^1 \text{ M}^{-1}$ ) experimentally obtained in various solvents.<sup>214,216,217</sup> In the next step, in the presence of  $\text{H}_3\text{O}^+$  or  $\text{H}_2\text{CO}_3$  as proton donor, the  $\text{Ni-CO}_2$  adduct converts into the  $[\text{Ni}(\text{CO})(\text{cyclam})]^{2+}$  species via a proton-coupled electron transfer concerted to C-O bond cleavage, similar to the mechanism proposed for the Fe porphyrins (Scheme 1). The final exergonic  $\text{CO}$  release step from  $[\text{Ni}(\text{CO})(\text{cyclam})]^{2+}$  completes the catalytic cycle.<sup>215</sup> However, under catalytic conditions the competitive one-electron reduction of  $[\text{Ni}(\text{CO})(\text{cyclam})]^{2+}$  may occur, leading to the formation of the  $[\text{Ni}(\text{CO})(\text{cyclam})]^+$  complex. The endergonic character of the  $\text{CO}$  dissociation step from this species, due to an increased  $\pi$ -backdonation from the more nucleophilic metal center to the bound  $\text{CO}$ , suggests that  $[\text{Ni}(\text{CO})(\text{cyclam})]^+$  may be accumulated during catalysis.<sup>215</sup> Despite the low  $\text{CO}$  solubility in aqueous



Scheme 2 Proposed mechanism for the electrochemical  $\text{CO}_2$ -to- $\text{CO}$  catalyzed by  $[\text{Ni}(\text{cyclam})]^{2+}$  (**40**).<sup>210,215</sup>

and organic solvents, the gaseous  $\text{CO}$  evolved during catalysis may also recombine with  $[\text{Ni}(\text{cyclam})]^+$ , depleting the catalyst at the interface, owing to the high values experimentally obtained for the  $\text{CO}$  binding constant ( $K_{\text{CO}} \sim 10^5 \text{ M}^{-1}$ ).<sup>218,219</sup> At more negative applied potentials,  $[\text{Ni}(\text{CO})(\text{cyclam})]^+$  can be further reduced to produce the unstable neutral  $[\text{Ni}(\text{CO})(\text{cyclam})]^0$  species, which undergoes rapid ligand loss, degrading to the  $\text{Ni}(\text{CO})_4$  deactivation product. The formation of both, the  $[\text{Ni}(\text{CO})(\text{cyclam})]^+$  and  $\text{Ni}(\text{CO})_4$  species was experimentally detected by *in situ* FTIR-spectro-electrochemistry (SEC) on a GC electrode under  $\text{CO}_2$  in  $\text{CH}_3\text{CN}$ , confirming the product inhibition of the catalyst.<sup>217</sup> In order to contrast catalyst poisoning by  $\text{CO}$  coordination, Kubiak and coworkers reported an alternative strategy based on the addition of a sacrificial carbonylation substrate to a solution of **40**.<sup>217</sup> The  $[\text{Ni}(\text{TMC})]^{2+}$  (TMC = 1,4,8,11-tetramethyl-1,4,8,11-tetraazacyclotetra-decane) complex was chosen for this purpose, due to its higher affinity for  $\text{CO}$  binding and lower  $\text{CO}_2\text{RR}$  ability on GC electrodes as compared to **40**.<sup>213</sup> The presence of an excess amount of  $[\text{Ni}(\text{TMC})]^{2+}$  effectively led to an observable current increase under  $\text{CO}_2$ . The role of  $[\text{Ni}(\text{TMC})]^+$  as a  $\text{CO}$  scavenger was further confirmed by FTIR-SEC, demonstrating the formation of  $[\text{Ni}(\text{CO})(\text{TMC})]^+$  during  $\text{CO}_2\text{RR}$  catalyzed by **40**. These results indicate the  $\text{CO}$  dissociation from the  $[\text{Ni}(\text{CO})(\text{cyclam})]^+$  species to be the rate-limiting step of  $\text{CO}_2\text{RR}$  on GC electrodes.

Despite the fact that significant synthetic efforts have been made over the past 30 years, most of the structural modifications to the cyclam macrocycle did not result in any improvement of the  $\text{CO}_2\text{RR}$  catalytic performance of the parent  $\text{Ni}^{\text{II}}$



complex **40**. A plethora of related Ni<sup>II</sup> complexes, comprising tetraaza open-chain ligands, alternative macrocyclic structures or substituted cyclam rings showed poorer CO<sub>2</sub>RR activity, selectivity or durability under electrochemical conditions.<sup>208,210</sup> The origin of the unique electrocatalytic behavior of [Ni(cyclam)]<sup>2+</sup> under CO<sub>2</sub> has been proposed to rely on a combination of structural and experimental factors, such as electrode material and electrolyte. The kinetic inertness of the macrocyclic [Ni(cyclam)]<sup>2+</sup> even in acidic media may explain the unique durability in comparison with other acyclic or cyclic analogous complexes.<sup>210</sup> Moreover, the redox-innocent character of the cyclam backbone increases the nucleophilicity of the Ni<sup>I</sup> center and, thus, its reactivity toward CO<sub>2</sub>. Lower affinity for CO<sub>2</sub> binding was observed for some Ni<sup>II</sup> derivatives bearing unsaturated 14-membered tetraazamacrocycles (“cyclam-like”).<sup>11,220</sup> The *N*-alkylation of the amine group of the cyclam ligand also led to a significant drop in the catalytic activity. This trend has been explained by a progressively diminished reducing power of the electrogenerated Ni<sup>I</sup> species by increasing the *N*-alkylation substitution level, consistent with the positive shift experimentally observed for the *E*<sup>0</sup>(Ni<sup>II/I</sup>) redox potential.<sup>213,215,221</sup> Steric hindrance of the bulky alkyl groups may also hamper the CO<sub>2</sub> binding, as well as influence the adsorption of the catalyst on the electrode surface.<sup>222</sup> Furthermore, the pendant amine functionalities installed on the cyclam moiety have been proposed to play a crucial role in the H-bonding stabilization of the η<sup>1</sup>-CO<sub>2</sub> adduct through an outer coordination sphere effect.<sup>11,213</sup> Notably, the attachment of an additional pendant NH<sub>3</sub><sup>+</sup> group to the cyclam structure provided an enhanced catalytic production of CO for the corresponding Ni<sup>II</sup> complex.<sup>223</sup>

The specific geometrical conformation of the cyclam ring was found to be critical for the efficiency of the catalyst, strongly affecting the stability of key molecular intermediates adsorbed on the electrode surface. In aqueous solution, [Ni(cyclam)]<sup>2+</sup> (**40**) exists as a mixture of two dominant different conformational isomers, namely *Trans-I* and *Trans-III*, respectively in a 15% and 85% equilibrium (see Chart 3).<sup>224</sup> Although the reductive Ni<sup>III/I</sup> process has been proposed to be accompanied by a rapid conformational change of the [Ni(cyclam)]<sup>+</sup> complex adsorbed on the Hg electrode,<sup>212,222,225</sup> the identity of the surface-bound conformer that plays the active role in catalysis is still under debate. Some experimental and computational studies suggested the *Trans-I* isomer of [Ni(cyclam)]<sup>+</sup> to be the preferred geometry for CO<sub>2</sub> binding compared to the *Trans-III* derivative, presumably due to a more favorable spatial orientation of the pendant N-H groups which would contribute to stabilize the Ni-CO<sub>2</sub> adduct by H-bonding interaction.<sup>11,213,215,222</sup> However, DFT optimized geometries of [Ni(CO)(cyclam)]<sup>+</sup> indicate that, in the homogeneous case, the *Trans-I* [Ni(cyclam)]<sup>+</sup> isomer binds CO much more strongly than the *Trans-III* conformer.<sup>217</sup> These findings suggest that a square-planar geometry is desirable to facilitate CO detachment from the carbonyl species, whereas out-of-plane distortions of the [Ni(CO)(cyclam)]<sup>+</sup> structure would contribute to further stabilize the metal-CO bond. In a recent integrated experimental-computational study, Kubiak and coworkers demonstrated that the *Trans-III* [Ni(cyclam)]<sup>+</sup> conformer

is preferentially adsorbed on a Hg surface through dispersive interactions, thus representing the active species involved in CO<sub>2</sub>RR.<sup>226</sup> Importantly, the Hg surface was found to facilitate the CO desorption kinetics of the adsorbed *Trans-III* [Ni(CO)(cyclam)]<sup>+</sup> complex, by weakening the Ni-CO σ interactions. The origin of this effect was ascribed to the flattened geometry of the adsorbed Ni macrocycle, which reduces the CO binding affinity. These findings shed light on the decisive role played by the catalyst-electrode interactions to explain the catalytic efficiency of [Ni(cyclam)]<sup>2+</sup> (**40**) on Hg under CO<sub>2</sub>, suggesting that the stability of the adsorbed [Ni(CO)(cyclam)]<sup>+</sup> intermediate influences the efficiency of the overall process.

Only a few molecular Ni derivatives containing tetraazamacrocyclic ligands have been reported to outperform the parent complex **40**. Among them, the *RRSS*-[Ni(HTIM)]<sup>2+</sup> (HTIM = 2,3,9,10-tetramethyl-1,4,8,11-tetraazacyclotetradecane) (**41**) and [Ni(MTC)]<sup>2+</sup> (MTC = 2,3-*trans*-cyclohexano-1,4,8,11-tetraazacyclotetradecane) (**42**) complexes described by Fujita *et al.* revealed to be excellent electrocatalysts for selective CO production on a Hg pool electrode at pH 5 and -0.96 V vs. NHE (Chart 3).<sup>216,225</sup> At very low pH values (pH < 2), CO/H<sub>2</sub> mixtures were produced depending on the applied potential. Analogously to the parent [Ni(cyclam)]<sup>2+</sup> complex, the remarkable activity of these systems was ascribed to their favorable geometry and stereochemistry. For instance, the *RRSS* isomer of the [Ni(HTIM)]<sup>2+</sup> complex (**41**) features a flat geometry analogous to the *Trans-III* conformer of [Ni(cyclam)]<sup>2+</sup>, suggesting an optimal ligand structure for adsorption on Hg. Moreover, the *RRSS* isomer was considerably more active than the *RSSR* isomer, since an unfavorable orientation of the bulky methyl groups in the latter hinders CO<sub>2</sub> binding at the Ni center. More recently, the functionalization of the reference [Ni(cyclam)]<sup>2+</sup> catalyst with a carboxylic acid led to a more efficient electrocatalyst, **43**, for selective CO<sub>2</sub>-to-CO conversion in aqueous media over a wide pH range.<sup>70</sup> The most remarkable aspect of this system consists in its significant selectivity toward CO production (FE<sub>CO</sub> = 66%; FE<sub>H<sub>2</sub></sub> = 15%) at -0.99 V vs. NHE in very acidic aqueous conditions (pH < 2), while the parent **40** catalyst predominantly produced H<sub>2</sub> (FE<sub>CO</sub> = 13%; FE<sub>H<sub>2</sub></sub> = 73%). Finally, it is worth mentioning that a number of di-<sup>211,227</sup> or trinuclear<sup>228</sup> Ni macrocyclic systems have been reported for CO<sub>2</sub>RR so far, showing comparable or inferior catalytic properties than **40**. However, a remarkable activity was recently shown for a dinuclear Ni<sup>II</sup> macrocycle complex (**44**, Chart 3),<sup>229</sup> displaying a synergistic cooperative effect between the two Ni centers analogous to a previously mentioned iron porphyrin system.<sup>100,136</sup> The catalyst exhibited an almost exclusive selectivity toward CO production on a GC electrode in a CH<sub>3</sub>CN:H<sub>2</sub>O (4:1) mixture as well as in pure water, outperforming both, a mononuclear Ni<sup>II</sup> derivative and a synthetic dinuclear system featuring a longer spatial distance between the Ni centers.

In addition to the electrode material, the catalytic CO<sub>2</sub>RR performances of Ni<sup>II</sup> tetraazamacrocyclic complexes were found to be extremely sensitive to the reaction medium. For [Ni(cyclam)]<sup>2+</sup>, a proper choice of solvent and electrolyte is vital to achieve an efficient and selective process, with water being a





Fig. 14 Cyclic voltammograms showing  $[\text{Ni}(\text{cyclam})]^{2+}$  (**40**, 1 mM) under Ar (black dashed line) and under  $\text{CO}_2$  (colored lines) with 0–5 equivalents of bis(3,5-trifluoromethyl)-phenylurea (Schreiner's urea, see the inset) as an additive. Reprinted with permission from ref. 230. Copyright 2019 American Chemical Society.

particularly suitable solvent. In an early report, the stability of the  $[\text{Ni}(\text{CO})(\text{cyclam})]^+$  complex was found to be significantly lower in aqueous media compared to DMF, suggesting that water may play an active role in promoting a fast decomposition of the deactivation carbonyl species.<sup>210</sup> Furthermore, the solvation properties of water molecules are crucial to stabilize the Ni– $\text{CO}_2$  adduct by H-bonding interactions. Recently, an electron-deficient organo-urea additive was reported to act as a multipoint H-bond donor, boosting the electrocatalytic  $\text{CO}_2\text{RR}$  of  $[\text{Ni}(\text{cyclam})]^{2+}$  in wet  $\text{CH}_3\text{CN}$  (up to 1 M  $\text{H}_2\text{O}$ ), without altering the exclusive selectivity of the catalyst to CO over  $\text{H}_2$  (Fig. 14).<sup>230</sup> In this system, the added urea acts as a co-catalyst rather than a stoichiometric additive, contributing to stabilize the key intermediates involved in the  $\text{CO}_2\text{RR}$  process. The superior promotional catalytic effect observed for the Schreiner's urea additive (two-point H-bond donor) compared to other single-point H-bond donors or acids, indicates that the effect is not due to acidity alone.

The use of different electrolytes or buffer systems in aqueous media also led to drastic changes in activity and selectivity of  $[\text{Ni}(\text{cyclam})]^{2+}$ .<sup>210</sup> The influence of the buffer identity on the catalytic  $\text{CO}_2\text{RR}$  activity of  $[\text{Ni}(\text{cyclam})]^{2+}$  was recently studied, revealing the buffer charge to be the main factor affecting the activity and selectivity of the reaction.<sup>231</sup> In particular, small-sized non-coordinating cationic buffers were found to be beneficial for  $\text{CO}_2\text{RR}$  over HER, suggesting the involvement

of pseudo outer coordination sphere effects (electrostatic, protonation, H-bonding interactions, *etc.*) on the key reaction intermediates. Albeit more disordered than the local effect previously discussed for molecular catalysts, the role of the electrolyte or buffer should be carefully taken into account for the optimization of a catalytic system, offering the opportunity to design local microenvironments for efficient  $\text{CO}_2\text{RR}$ . The catalytic behavior of  $[\text{Ni}(\text{cyclam})]^{2+}$  was also explored in ionic liquids, showing better activity and selectivity for CO production by using the hydrophilic 1-butyl-3-methylimidazolium tetrafluoroborate ( $\text{BMImBF}_4$ ) solvent/electrolyte system.<sup>232</sup> On the other hand, an unexpected change of selectivity was observed by using DMF with low water content as reaction medium, resulting in the production of  $\text{CO}/\text{HCOO}^-$  mixtures depending on the applied potential ( $\text{FE}_{\text{HCOO}^-}$  up to 75%).<sup>211</sup> This apparently counterintuitive behavior was ascribed to the formation of an alternative Ni– $\eta^1\text{-OCO}$  adduct, which however was predicted to be energetically less favored than the  $\eta^1\text{-CO}_2$  one.<sup>215</sup>

Although  $[\text{Ni}(\text{cyclam})]^{2+}$  is a very efficient and low-cost electrocatalyst for CO production operating in aqueous media, the need for hazardous mercury pool-based electrodes strongly limits its usage for practical applications. As above mentioned, owing to the key role played by the electrode material in the catalytic reaction, the replacement of Hg with more environmentally friendly solid electrodes while maintaining a comparable catalytic performance is a challenge. In this perspective, some attempts have been described in order to covalently attach Ni tetrazamacrocycle molecular systems to carbon-based electrodes<sup>233</sup> or metal oxide-based photoelectrodes.<sup>234</sup> For example, some  $[\text{Ni}(\text{alkynyl-cyclam})]^{2+}$  catalysts anodically electrografted to the surface of a GC electrode, displayed a predominant  $\text{H}_2$  evolution activity ( $\text{FE}_{\text{H}_2} = 89\%$ ;  $\text{FE}_{\text{CO}} = 7\%$ ) in a  $\text{CO}_2$  saturated  $\text{CH}_3\text{CN}/\text{water}$  solution, attributing the low performance to a possible steric hindrance of the catalyst conformation detrimental for  $\text{CO}_2\text{RR}$ .<sup>233</sup> A more efficient system was obtained by incorporating the  $[\text{Ni}(\text{cyclam})]^{2+}$  complex into a poly(allylamine) (PALA) matrix, through Schiff's base condensation *via* axial coordination of 4-pyridinecarboxaldehyde.<sup>235</sup> Both, the axial pyridine coordination and the encapsulation into the polymer backbone contributed to lower the overpotential, enabling a durable CO production with high faradaic yields (79–92%) over 24 h at  $-0.78$  V *vs.* Ag/AgCl (pH 8, 50 mM Tris buffer). As previously discussed, analogous beneficial effects of pyridine coordination and/or polymer encapsulation on  $\text{CO}_2\text{RR}$  have been observed for several cobalt phthalocyanine or porphyrin systems (see Section 3). This approach is particularly attractive to incorporate molecular catalysts into biological scaffolds for the synthesis of bioinspired systems that can be used for catalytic purposes. In particular, proteins are robust platforms featuring a well-defined hosting environment which offers the opportunity to modulate the activity/selectivity of molecular catalysts through secondary coordination sphere interactions. As an example, the axial coordination of the Ni-cyclam catalyst at a pendant histidine residue of azurin led to an artificial metalloenzyme active for  $\text{CO}_2\text{RR}$ , displaying a



positive shift in the onset catalytic potential under CO<sub>2</sub> compared to free [Ni(cyclam)]<sup>2+</sup>.<sup>236</sup> Although bulk electrolysis data were not reported, photocatalytic quantitative data showed an increased selectivity to CO for the azurin-[Ni(cyclam)]<sup>2+</sup> scaffold in comparison with free [Ni(cyclam)]<sup>2+</sup>, suggesting a critical role played by the protein environment. Moreover, the presence of the redox-active Cu center also had a remarkable impact on improving the selectivity towards CO<sub>2</sub>RR, mimicking the role of iron-sulfur clusters in CODH. Owing to the extremely conformation-sensitive CO<sub>2</sub>RR process mediated by [Ni(cyclam)]<sup>2+</sup>, it was also speculated that the protein environment may induce constraints to geometrical distortions of the cyclam ligand, favoring CO<sub>2</sub>RR over HER.<sup>236</sup>

Finally, Machan and co-workers demonstrated the possible implementation of homogeneous systems for CO<sub>2</sub>RR using a flow-cell technology.<sup>237</sup> More specifically, [Ni(cyclam)]<sup>2+</sup> was employed as a benchmark homogeneous electrocatalyst in a non-aqueous electrolyzer for CO<sub>2</sub>RR to CO based on a continuous flow-cell configuration (Fig. 15). In this setup, ferrocene served as a sacrificial electron donor, whereas NH<sub>4</sub>PF<sub>6</sub> was used as both exogenous proton donor and supporting electrolyte. The flow-cell system afforded CO production with FE > 80% and current densities up to 50 mA cm<sup>-2</sup> using a graphite felt cathode in CH<sub>3</sub>CN in the presence of 0.5 M NH<sub>4</sub>PF<sub>6</sub>. Compared to the behavior in a conventional H-type cell setup, the [Ni(cyclam)]<sup>2+</sup> homogeneous catalyst showed extended durability and better selectivity in the flow-cell configuration. Moreover, it was found that the solvent plays a key role in the efficiency of the process, with CH<sub>3</sub>CN providing the best results

owing to its high CO<sub>2</sub> solubility and favorable H-bonding ability (compared to DMF, as aforementioned for Fe porphyrins<sup>122</sup>). As expected, the system was limited by the formation of inactive [Ni(CO)(cyclam)]<sup>+</sup> and Ni(CO)<sub>4</sub> species, which were detected by UV-Vis and FTIR spectroscopy.<sup>237</sup> Albeit achieving lower current densities compared to the flow-cell setups developed for immobilized molecular catalysts in aqueous media, this approach holds promise and, together with further engineering optimization, can be extended to other types of molecular catalysts, or used to pair CO<sub>2</sub>RR with oxidative processes using organic substrates.

**4.1.2 Cobalt.** Analogously to the Ni derivatives, the Co tetraamacycle complexes have been widely studied. However, while the Ni-cyclam derivatives have received much more attention compared to other macrocycles, several studies have focused on the investigation of Co complexes with cyclam-related ("cyclam-like") 14-membered macrocycles containing unsaturated imine bonds, and, more specifically, on the [Co(HMD)]<sup>2+</sup> system (**45**, HMD = 5,7,7,12,14,14-hexamethyl-1,4,8,11-tetraaza-cyclotetradeca-4,11-diene) (see Chart 3). [Co(cyclam)]<sup>2+</sup> and [Co(HMD)]<sup>2+</sup> complexes were reported as molecular catalysts for the photochemical<sup>238,239</sup> and electrochemical<sup>208,240</sup> CO<sub>2</sub>RR. Nevertheless, lower selectivity was obtained as compared to their Ni analogues, resulting in a mixture of CO, HCOO<sup>-</sup> and H<sub>2</sub> products. In particular, Fisher and Eisenberg reported the electrocatalytic production of a CO/H<sub>2</sub> 1:1 mixture for **45** at -1.6 V vs. SCE in pure water or a H<sub>2</sub>O/CH<sub>3</sub>CN mixed solvent.<sup>208</sup> The lower selectivity for CO<sub>2</sub>RR shown by **45** as compared to **40** is related to the different reactivity of the [Co(HMD)]<sup>+</sup> and



**Fig. 15** Non-aqueous flow cell electrolyzer with [Ni(cyclam)]<sup>2+</sup> (**40**) as homogeneous electrocatalyst for CO<sub>2</sub> electroreduction to CO. (a) Schematic plot of the recirculating flow setup. (b) Picture of the flow electrolyzer during operation. (c) FE with various catalyst concentrations at 1.6 V cell potential; (d) current density profiles at various cell potentials; (e) current density contribution measured by gaseous products at various cell potentials. Conditions: 5 cm<sup>2</sup> of graphite felt as electrode, 10 mM [Ni(cyclam)]<sup>2+</sup> (**40**) or varied as noted in (d) and (e)), 0.5 M NH<sub>4</sub>PF<sub>6</sub> as supporting electrolyte in CH<sub>3</sub>CN, 0.1 M Fc as sacrificial electron donor, flow rate 8.0 mL min<sup>-1</sup>, three layers of Celgard film. All experiments in a two-electrode configuration with cathode and anode electrodes made of graphite felt (SIGRACELL, GFD4.6 EA, 4.6 mm thickness, 5 cm<sup>2</sup> area). Current density is calculated as the average of the first hour of electrolysis, and the measured faradaic efficiency corresponds to the product analysis after 1 h of electrolysis. Adapted with permission from ref. 237. Copyright 2020 American Chemical Society.



$[\text{Ni}(\text{cyclam})]^+$  active species towards  $\text{H}^+$ . As derived by a comparison of the  $\text{CO}_2/\text{H}^+$  binding constants for the two complexes, the protonation of the  $[\text{Co}(\text{HMD})]^+$  complex is favored over  $\text{CO}_2$  binding at considerably higher pH values than  $[\text{Ni}(\text{cyclam})]^+$ , resulting in the ability for the latter to selectively catalyze  $\text{CO}_2\text{RR}$  in a wider pH range.<sup>214,241</sup>

Due to the flexibility of the macrocyclic ligand, the  $[\text{Co}(\text{HMD})]^{2+}$  complex exists in the *N-rac* and *N-meso* isomeric forms. At room temperature, the isomerization reaction was found to occur slowly for the  $\text{Co}^{\text{II}}$  complexes but much faster for the singly reduced  $\text{Co}^{\text{I}}$  species, rapidly converting the *N-meso* into the *N-rac* isomer.<sup>11</sup> The proposed mechanism for  $\text{CO}_2\text{RR}$  is analogous to the one previously discussed for the  $[\text{Ni}(\text{cyclam})]^{2+}$  catalyst, involving the  $\text{CO}_2$  binding at the electrogenerated  $\text{Co}^{\text{I}}$  species. However, the  $[\text{Co}(\text{HMD})]^+$  complex exhibited a much higher affinity for  $\text{CO}_2$  in DMSO as compared to the Ni analogue.<sup>220</sup> In contrast to the latter, the reversible  $\text{CO}_2$  binding to  $[\text{Co}(\text{HMD})]^+$  resulted in an observable positive shift of the voltammetric  $\text{Co}^{\text{II/I}}$  wave, which allowed the estimation of a  $K_{\text{CO}_2}$  as high as  $7 \times 10^4 \text{ M}^{-1}$ . Owing to the large value of the  $\text{CO}_2$  binding constant, Fujita and co-workers afforded to isolate the  $[\text{Co}(\text{CO}_2)(\text{HMD})]^+$  adduct and thoroughly investigated its electronic structure in  $\text{CH}_3\text{CN}$  by using a number of spectroscopic techniques, including UV-Vis, FTIR,  $^1\text{H-NMR}$ , XANES, laser-flash photolysis and pulse radiolysis.<sup>11,241–246</sup> Unlike the case of the similar  $[\text{Ni}(\text{CO}_2)(\text{cyclam})]^+$  adduct, spectroscopic evidences of a strong charge transfer from the  $\text{Co}^{\text{I}}$  center to the bound  $\text{CO}_2$  were found for  $[\text{Co}(\text{CO}_2)(\text{HMD})]^+$ , suggesting a  $[\text{Co}^{\text{II}}(\text{CO}_2\cdot^-)(\text{HMD})]^+$  structure.<sup>11,246</sup> At low temperature, as an effect of *trans* axial coordination of a solvent  $\text{CH}_3\text{CN}$  molecule to form the six-coordinate  $[\text{Co}(\text{CH}_3\text{CN})(\text{CO}_2)(\text{HMD})]^+$  adduct, an even stronger metal-to-ligand charge transfer was observed, suggesting the formation of the  $[\text{Co}^{\text{III}}(\text{CH}_3\text{CN})(\text{CO}_2^{2-})(\text{HMD})]^+$  complex.<sup>11,246</sup> The stereochemical features of the  $\text{Co}-\text{CO}_2$  adduct were found to be critical for the  $\text{CO}_2$  binding step, including the conformational geometry of the macrocyclic ligand and the steric hindrance provoked by the methyl groups.<sup>242</sup> Furthermore, an additional stabilization due to intramolecular H-bonding interaction with pendant NH groups was proposed to have a remarkable impact on the  $\text{CO}_2$  binding properties of the  $\text{Co}^{\text{I}}$  species.<sup>245</sup> The pivotal role of H-bonding stabilization of the  $\text{Co}-\text{CO}_2$  intermediate is also consistent with the experimental observation that polar solvents, and in particular water, favorably impact the value of the  $\text{CO}_2$  binding constant.<sup>241,247</sup>

As aforementioned for the Ni derivatives,  $\text{Co}^{\text{I}}$  tetraazamacrocycles also generally show higher affinity for CO than for  $\text{CO}_2$ , owing to a strong  $\pi$ -backdonation from the metal to coordinating CO. The  $[\text{Co}(\text{CO})(\text{HMD})]^+$  complex was isolated and characterized, featuring a five-coordinated square-pyramidal geometry with a significant out-of-plane distortion of the Co center.<sup>248</sup> As previously discussed for  $[\text{Ni}(\text{CO})(\text{cyclam})]^+$ , the flexibility of the HMD ligand contributes to further stabilize the  $\text{Co}-\text{CO}$  bond. It is worth mentioning that diluted  $\text{CH}_3\text{CN}$  solutions of freshly prepared  $[\text{Co}(\text{CO}_2)(\text{HMD})]^+$  partially decomposed after several days, resulting in the formation of traces of CO and  $\text{H}_2$

(derived from adventitious water) in the vessel headspace.<sup>243</sup> A binuclear Co species containing a  $\text{Co}-\text{COOH}-\text{Co}$  motif was isolated from the solution and characterized by X-ray crystallography, thus suggesting the possibility that the cooperative effect of a second Co center may be involved in the  $\text{CO}_2$  binding step.<sup>249</sup>

## 4.2 Pyridyl-based macrocyclic ligands

This section focuses on the main reported molecular catalysts for  $\text{CO}_2\text{RR}$  based on non-cyclam macrocyclic ligands, highlighting some fundamental electronic and structural aspects related to the role of the ligand framework in the catalytic  $\text{CO}_2\text{RR}$  process. A first representative example is given by the Co systems with the N4H ligand (N4H = 2,12-dimethyl-3,7,11,17-tetraazabicyclo-[11.3.1]-heptadeca-1(7),2,11,13,15-pentaene), which contains the potentially redox-active pyridyldiimine platform (see Chart 4). In some early studies, Co and Ni complexes of the N4H ligands were found to be relatively poor catalysts for  $\text{CO}_2\text{RR}$ , suffering from low efficiencies toward CO production and/or a severe HER competition.<sup>208,240,250</sup> Several years later, Peters and co-workers investigated the electrocatalytic behavior of the  $[\text{Co}^{\text{III}}(\text{N4H})(\text{Br})_2]^+$  complex (**46**, see Chart 4), with voltammetric data showing a catalytic current for  $\text{CO}_2$  reduction upon the formal  $\text{Co}^{\text{I/0}}$  wave.<sup>251</sup> Bulk electrolysis under  $\text{CO}_2$  in aqueous  $\text{CH}_3\text{CN}$  (10 M  $\text{H}_2\text{O}$ ) resulted in moderate faradaic yields for CO production ( $\text{FE}_{\text{CO}} = 45\%$ ) together with  $\text{H}_2$  evolution ( $\text{FE}_{\text{H}_2} = 30\%$ ). Albeit non selective for  $\text{CO}_2\text{RR}$  to CO, this result is remarkable since the same complex was well-known to efficiently catalyze HER in the absence of  $\text{CO}_2$ .<sup>252,253</sup> The five-coordinated  $[\text{Co}(\text{N4H})(\text{CH}_3\text{CN})]^+$  complex, containing a formal  $\text{Co}^{\text{I}}$  state was chemically generated and found to be a pre-catalyst for  $\text{CO}_2\text{RR}$ . Owing to the redox non-innocent character of the N4H moiety,<sup>254</sup> DFT calculations suggested its electronic structure to be best described as a low-spin  $\text{Co}^{\text{II}}$  antiferromagnetically coupled to a ligand radical anion, which was hypothesized to contribute in steering the selectivity towards  $\text{CO}_2\text{RR}$  over HER.<sup>251</sup> In a later study, *in situ* FTIR spectroscopy was used to detect the  $[\text{Co}^{\text{I}}(\text{N4H})(\text{CO}_2)]^+$  species, selectively generated upon visible-light irradiation of the starting  $[\text{Co}^{\text{II}}(\text{N4H})(\text{CH}_3\text{CN})]^{2+}$  complex in the presence of a sacrificial electron donor and a  $[\text{Ru}(\text{bpy})_3]^{2+}$  photosensitizer.<sup>255</sup> Intramolecular H-bonding interaction between the N-H of the macrocycle ligand and the oxygen atom of bound  $\text{CO}_2$  was proposed to strongly contribute to the stabilization of this adduct, whose formation was found to be critical for the selectivity of the overall  $\text{CO}_2\text{RR}$  process. This shed light on the crucial role played by the metal-ligand cooperation for  $\text{CO}_2$  activation. Moreover, a photochemical treatment of the initial  $[\text{Co}^{\text{II}}(\text{N4H})(\text{CH}_3\text{CN})]^{2+}$  complex with  $[\text{Ir}(\text{ppy})_3]$  sensitizer, which has stronger reducing power than  $[\text{Ru}(\text{bpy})_3]^{2+}$ , led to the formation of the transient two-electron-reduced  $[\text{Co}^{\text{I}}(\text{N4H})(\text{CO}_2^-)]$  intermediate, detected by using rapid-scan FTIR spectroscopy.<sup>256</sup> This adduct underwent spontaneous CO dissociation and catalyst regeneration on the timescale of seconds at room temperature, allowing to monitor the bond breaking step leading to CO evolution.



In an effort to rationalize the second coordination sphere effect of pendant amines on the CO<sub>2</sub>RR capability of Co macrocycles, Marinescu and co-workers recently investigated a series of Co complexes based on the macrocyclic azacalix[4](2,6)pyridine framework with different alkyl substituents on the four pendant N-H groups (Chart 4).<sup>119,257</sup> In DMF solution, the complex **47**, which contains four secondary amines, showed a catalytic current increase under CO<sub>2</sub> atmosphere upon the Co<sup>I/0</sup> wave, resulting in an excellent faradaic yield for CO production (98%) at -2.8 V vs. Fc<sup>+0</sup> in the presence of 1.2 M TFE as exogenous proton source.<sup>119</sup> In sharp contrast, the *N*-alkylated derivatives (methyl and allyl groups, respectively) containing only tertiary amines displayed negligible catalytic current for CO<sub>2</sub> reduction, despite the fact that the presence of the electron-donating alkyl groups causes a negative shift of the Co<sup>I/0</sup> redox potential as compared to **47**. Bulk electrolysis data confirmed the latter to be poor CO<sub>2</sub>RR electrocatalysts with low CO faradaic efficiencies, probing the crucial effect of the secondary N-H macrocycle groups on both, the catalytic overpotential and efficiency. An additional experimental-theoretical kinetic analysis on a series of Co complexes featuring varying secondary and tertiary (*N*-methyl substituents) macrocyclic amines (**47**–**52**, see Chart 4), was carried out to further investigate the origin of such boosting effect (Fig. 16a).<sup>257</sup> Unlike **52**, the complexes **47**–**51** showed high CO current densities and FEs (≥90%), resulting in a linear correlation between the catalytic rate constant and the number of secondary amines across the series (Fig. 16b). An analogous rate measured for isomers **49** and **50** indicates that the spatial orientation of the pendant N-H groups has only a minimal effect on the rate, suggesting a non-cooperative effect of the pendant amines. The first step of the proposed catalytic mechanism consists in the two-electron reduction of the initial Co<sup>II</sup> state to form the formal Co<sup>0</sup> species responsible for CO<sub>2</sub> binding (Fig. 16c). This aspect, which was confirmed by both experimental and theoretical data, is in contrast with the behavior shown by the cyclam-like Co systems, whereby the nucleophile Co<sup>I</sup> species is able to bind

to the substrate.<sup>11</sup> Moreover, owing to the conformational strain of the azacalix[4](2,6)pyridine macrocycle, the pendant N-H groups were predicted to exert an unfavorable intramolecular H-bonding to the bound CO<sub>2</sub> molecule. Instead, the steric repulsion of the *N*-methyl groups was found to have a major effect on CO<sub>2</sub> binding. In analogy with the tetrazamacrocycle Co systems,<sup>246</sup> DFT calculations suggest that an intramolecular charge transfer from the Co center to CO<sub>2</sub> stabilizes the Co-CO<sub>2</sub> adduct. The CO<sub>2</sub> binding is followed by two sequential protonation steps (EECC mechanism), with the latter being the rate-limiting step, forming H<sub>2</sub>O and a Co<sup>II</sup>-CO intermediate, which undergoes a facile release of CO. Theory confirmed the involvement of the secondary pendant amines in the second rate-limiting protonation step, assisting the intermolecular H<sup>+</sup> transfer from the acid to the bound COOH, rather than *via* an intramolecular H<sup>+</sup> transfer from the N-H group to COOH.<sup>257</sup>

As previously discussed for heme and tetrazamacrocycle complexes, a planar and rigid geometry of the ligand framework is particularly suitable for a molecular catalyst to promote an efficient CO<sub>2</sub>RR. In particular, the beneficial role of macrocyclic platforms, also known as “macrocyclic effect”, generally results in an improved catalyst durability and overall efficiency of the process. Jurss and co-workers have recently investigated the effect of structural rigidity on the electronic and catalytic properties of the metal center in a series of Co and Ni complexes bearing redox-active ligands based on bipyridyl-*N*-heterocyclic carbene (NHC) moieties (Chart 4 and Fig. 17).<sup>258,259</sup> In these studies, Ni and Co complexes based on 16- and 15-membered macrocyclic ligands (**53-X** and **54-X** with X = Ni, Co, respectively, see Chart 4) displaying different rigidity were explored for electrocatalytic CO<sub>2</sub>RR and compared with the corresponding non-macrocyclic analogues (indicated as bpy-NHC-X, X = Ni, Co, see Fig. 17). In the Ni series, the bpy-NHC-Ni complex exhibited the most flexible geometry, whereas distorted square-planar configurations were observed for **53-Ni** and **54-Ni**, with the smaller **54-Ni** macrocycle being the most planar.<sup>258</sup> A marked difference was shown when comparing the



Chart 4 Structures of selected molecular Ni, Co and Fe catalysts for CO<sub>2</sub>RR supported by pyridyl-based macrocyclic ligands.





**Fig. 16** (a) Sketch of the Co complexes **47–52**. (b) Experimental catalytic rate constants,  $k_{\text{obs}}$  (s<sup>-1</sup>), as a function of the number of pendant secondary amines for complexes **47–52** measured in the presence of 1.5 M TFE and under CO<sub>2</sub> saturation at a scan rate of 0.1 V s<sup>-1</sup>. Rates are obtained from the plateau current. A linear fit ( $R^2 = 0.97$ ) is shown in gray for complexes **47–52**. (c) Proposed EEC catalytic cycle illustrated with complex **1<sup>(0)</sup> = 47** where E = electrochemical, and C = chemical step. Adapted with permission from ref. 257. Copyright 2018 American Chemical Society.

long-term electrocatalytic CO<sub>2</sub>RR-to-CO performances in wet CH<sub>3</sub>CN across the series, following the order bpy-NHC-Ni < **53-Ni** < **54-Ni**: the most rigid 15-membered **54-Ni** derivative

exhibited high faradaic yields for CO production (87%) while the bpy-NHC-Ni system predominantly produced H<sub>2</sub> (Fig. 17b). The different catalytic behavior was rationalized in terms of the

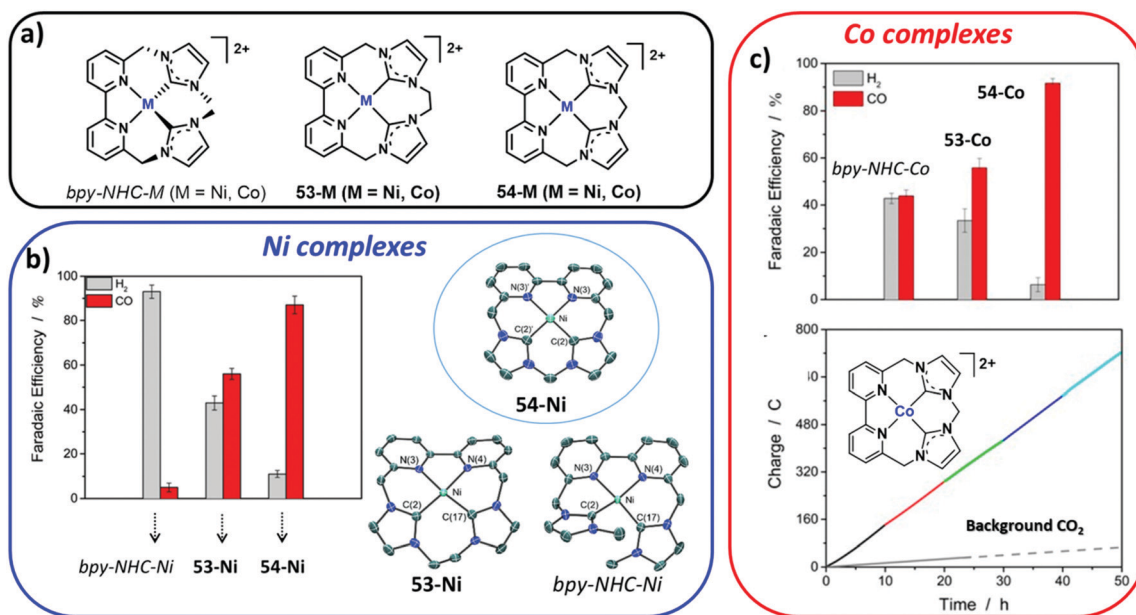


**Fig. 17** (a) Sketch of the families of Ni<sup>II</sup> and Co<sup>II</sup> catalysts supported by non-macrocylic and macrocylic bipyridyl-NHC ligands. (b) FEs for H<sub>2</sub> (grey) and CO (red) obtained during controlled-potential electrolysis with 0.2 mM of **53-Ni**, **54-Ni**, **bpy-NHC-Ni**, respectively. Electrolyte: CO<sub>2</sub>-saturated CH<sub>3</sub>CN/0.1 M *n*-Bu<sub>4</sub>NPF<sub>6</sub> solutions containing 2% H<sub>2</sub>O at a GC rod. The inset shows the ORTEP diagrams of cations in **53-Ni**, **54-Ni** and **bpy-NHC-Ni**. (c) (top) FEs for H<sub>2</sub> (grey) and CO (red) from electrolysis experiments with 10 μM Co catalyst in CO<sub>2</sub>-saturated H<sub>2</sub>O/0.1 M NaClO<sub>4</sub> at a Hg pool (4 cm dia.) working electrode. On the bottom, a charge vs. time plot of consecutive CPEs is reported with 10 μM **54-Co** (see inset) in CO<sub>2</sub>-saturated aqueous 0.1 M NaClO<sub>4</sub>. Conditions:  $E_{\text{appl}} = -1.04$  V vs. NHE, Hg pool. CO<sub>2</sub> was re-saturated every 10 h. Adapted with permission from ref. 258 and 259. Copyright 2018–2019 Royal Society of Chemistry and American Chemical Society, respectively.



nature of the  $1e^-$  reduced species, which was calculated to be metal-centered for the flexible bpy-NHC-Ni system and ligand-based for the more constrained **54-Ni** complex. In other words, the flexible open platform leads to a more nucleophilic Ni center upon the first electron uptake, favoring the formation of a Ni-hydride intermediate responsible for the observed selectivity loss.<sup>258</sup>

The same reactivity trend was also observed for the Co series, with enhanced FE, TOF and activity for CO production found for more rigid macrocyclic platforms.<sup>259</sup> In particular, a stark difference was observed by comparing the bulk electrolysis data obtained in aqueous media (pH 4.2) on a Hg pool electrode (Fig. 17c). The more planar **54-Co** system exhibited excellent CO selectivity over HER, in contrast to the open-chained bpy-NHC-Co catalyst which resulted in the production of an approximately 1:1 CO:H<sub>2</sub> gas mixture. In a similar fashion as [Ni(cyclam)]<sup>2+</sup>, a reductive adsorption of the molecular catalysts over the Hg electrode surface was found to occur. As for the Ni congeners, the structural features of the ligand scaffolds directly affected the electronic structure and reactivity of the reduced Co complexes, allowing to build-up a structure-reactivity relationship. However, unlike the Ni counterparts, the first electron uptake was found to be ligand-based for all of the Co complexes. On the contrary, the nature of the second reduction markedly differs across the series, being ligand-based for bpy-NHC-Co and metal-centered for **54-Co**. Thus, for the Co series, more rigid ligand frameworks contribute to increase the nucleophilicity of the Co center in the  $2e^-$  reduced species, thus favoring the CO<sub>2</sub> binding step and increasing the selectivity towards CO<sub>2</sub>RR. In contrast with the trend observed for the Ni and Co tetraazamacrocycles, the Co derivatives with bipyridyl-NHC ligands revealed to be better catalysts for CO<sub>2</sub>RR to CO compared to their Ni analogues in terms of overpotential, activity and selectivity in the presence of H<sub>2</sub>O. From one side, these examples highlight the crucial role of the redox non-innocent character and geometry of the ligand in catalysis. On the other hand, the differences in the electronic structure observed for Ni and Co macrocycles bearing the same ligand platform suggests that the nature of the metal center also has a strong influence on the reactivity towards CO<sub>2</sub>RR. In some cases, a simple change of the metal center may lead to a drastic change in the product distribution for CO<sub>2</sub>RR. For example, the Co complex bearing a pentadentate N5 pyridine-diimine macrocycle (**55-Co**) was reported as a selective catalyst for CO<sub>2</sub> electroreduction to CO in DMF, whereas the Fe counterpart (**55-Fe**) produced HCOO<sup>-</sup> in high faradaic yields.<sup>260</sup> The origin of such a drastic change of selectivity was ascribed to the poor  $\pi$ -donating properties of the active Fe site, which stabilizes a  $\eta^1$ -OCOH adduct.

### 4.3 Non-macrocyclic tetradentate nitrogen ligands

In addition to the heme and non-heme macrocyclic systems, some representative classes of Fe, Co and Ni organometallic complexes based on non-macrocyclic N4 ligands have been recently reported to be competent catalysts for CO<sub>2</sub>RR.

Lu and co-workers recently described a non-cyclam Ni<sup>II</sup> tripodal homogeneous electrocatalyst (**56**, see Chart 5) exhibiting

a remarkable selectivity toward CO production in DMF/H<sub>2</sub>O mixtures even in the presence of relevant amounts of added water.<sup>261</sup> The origin of the high intrinsic affinity for CO<sub>2</sub> over H<sup>+</sup> and robustness of **56** compared to other analogous molecular complexes, was ascribed to the strong basicity of the ligand, containing the methylated benzimidazole donors. The redox-innocent character of the ligand strongly enhances the nucleophilicity of the Ni<sup>I</sup> center which readily binds CO<sub>2</sub>, as suggested by an observable positive shift of the voltammetric Ni<sup>III/I</sup> wave under CO<sub>2</sub>-saturated conditions. The product distribution could be tuned in a controlled manner by modulating the applied potential, affording syngas mixtures with a CO:H<sub>2</sub> ratio of 1:1 or 1:2 at more negative potentials, likely due to the partial contribution of the less CO<sub>2</sub>RR selective Ni<sup>I/0</sup> wave.<sup>261</sup>

The majority of the non-heme Fe electrocatalysts studied for CO<sub>2</sub>RR displayed high or moderate faradaic efficiencies for formate production, including a highly selective iron carbonyl cluster catalyst<sup>69,262,263</sup> and Fe complexes with bipyridine-containing Schiff base ligands,<sup>264,265</sup> phenanthroline derivatives<sup>266</sup> or macrocyclic nitrogen platforms.<sup>260</sup> Recently, a series of Fe<sup>II</sup> complexes supported by polydentate bipyridyl-based platforms bearing different functional groups in the second coordination sphere, were explored for CO<sub>2</sub>RR.<sup>267</sup> Among them, the only system showing a high selectivity for CO production in aqueous CH<sub>3</sub>CN (FE<sub>CO</sub> = 81%; FE<sub>H<sub>2</sub></sub> = 11%) was a derivative featuring a pendant secondary amine group (**57**). An increased acidity of the intramolecular proton relay (phenolic functionality) was found to dramatically enhance the H<sub>2</sub> evolution process. It is noteworthy that changes in the CO<sub>2</sub>RR selectivity induced by appended groups in the second coordination sphere have been recently reported also for molecular Mn catalysts.<sup>268–271</sup> Moreover, a non-heme Fe complex with a tetradentate dicarboxamide N4 in-plane ligand (**58**), recently showed a high selectivity for CO<sub>2</sub> electroreduction to CO as a homogeneous electrocatalyst in DMF/2% H<sub>2</sub>O solvent mixture.<sup>272</sup> In addition, the complex was immobilized on N-doped graphene (N-G) by refluxing a DMF solution of **58** in the presence of suspended N-G platelets. It was suggested that this procedure induced immobilization of **58** on N-G *via* axial coordination by N dopants of the graphene support to the Fe centers, promoted by the  $\pi$ - $\pi$  stacking interaction between the planar ligand framework of the complex and the graphene layer. The heterogeneous catalyst supported on a GC electrode resulted in an efficient and selective CO<sub>2</sub> conversion to CO (FE<sub>CO</sub> = 90%) in aqueous media (pH = 7.3) at  $-0.58$  V *vs.* RHE.<sup>272</sup>

Among the earth-abundant transition metal molecular catalysts containing alternative polydentate platforms, the polypyridyl, aminopyridyl or tripodal cobalt complexes are perhaps the most widely studied systems. In general, the reported activity and selectivity of these catalysts strongly varies depending on the ligand framework and the specific operating reaction conditions. For instance, Che and co-workers recently reported a series of Co complexes with tetradentate N donor ligands for the electro- and photocatalytic CO<sub>2</sub>RR.<sup>273</sup> Among those systems, only the *cis*-[Co(PDP)Cl<sub>2</sub>] complex (**59**, PDP = 1,1'-bis(2-pyridinylmethyl)-2,2'-bipyridine) displayed a selective electrocatalytic CO production





Chart 5 Structures of selected molecular Ni, Co and Fe catalysts for CO<sub>2</sub>RR supported by non-macrocyclic tetradentate nitrogen ligands.

in CH<sub>3</sub>CN, albeit the FE<sub>CO</sub> was found to progressively decrease over time during electrolysis. Contrariwise, the other complexes of the series supported by similar ligands displayed very poor electrocatalytic properties for CO<sub>2</sub>RR, resulting in the formation of only traces of CO.<sup>273</sup> In another comparative study, a family of tripodal Co<sup>II</sup> complexes containing pyridyl or less basic quinolyl groups displayed variable ability for a selective CO<sub>2</sub>-to-CO conversion under electrochemical conditions, with the complexes **60** and **61** showing the best performances (FE<sub>CO</sub> = 58–72% and 84%, respectively).<sup>274</sup> Furthermore, a number of polypyridyl Co complexes were reported to suffer from very low faradaic yields for CO production (≤30%),<sup>275,276</sup> which are not related to competitive HER or to alternative CO<sub>2</sub>RR pathways. In addition, moderate durability in long-term electrolysis is generally reported even for some CO-selective Co systems, suggesting a possible CO deactivation pathway.<sup>119</sup>

In an effort to rationalize the electrocatalytic CO<sub>2</sub>RR behaviour of aminopyridyl Co catalysts, Lloret-Fillol and co-workers recently reported a compelling experimental–computational mechanistic study on the model [Co(L<sup>N4</sup>)](OTf)<sub>2</sub> complex (**62**, L<sup>N4</sup> = 1-[2-pyridylmethyl]-4,7-dimethyl-1,4,7-triazacyclononane), elucidating its reactivity towards CO<sub>2</sub> at different redox potentials.<sup>277</sup> Owing to the highly basic character of the L<sup>N4</sup> ligand, both experimental and computational data indicate that the nucleophilic Co<sup>I</sup> species is able to undergo CO<sub>2</sub> binding and C–O bond cleavage steps at the Co<sup>III/I</sup> redox potential in anhydrous CH<sub>3</sub>CN, leading to the formation of the key [Co(CO)(L<sup>N4</sup>)]<sup>+</sup> complex. This pivotal intermediate, analogously to the deactivating carbonyl species observed in the case of [Ni(cyclam)]<sup>2+</sup>

(*vide supra*), was *in situ* detected under electrochemical conditions and thoroughly characterized by a combination of spectroscopic and SEC techniques (UV-Vis, FTIR). However, the endergonicity of the CO release step from [Co(CO)(L<sup>N4</sup>)]<sup>+</sup> prevented the observation of an electrocatalytic CO<sub>2</sub>RR behavior at low overpotentials. Under pure electrochemical conditions, a catalytic CO production can be achieved only at more negative potentials (close to the formal Co<sup>I/0</sup> couple), required for further reduction of [Co(CO)(L<sup>N4</sup>)]<sup>+</sup>, giving rise to a proposed alternative pathway based on the binding of another CO<sub>2</sub> molecule at the Co center (Fig. 18, blue). In contrast, an efficient catalysis was observed at the Co<sup>III/I</sup> redox potential under photochemical conditions, in which the more favorable CO release from the [Co(CO)(L<sup>N4</sup>)]<sup>2+</sup> intermediate was proposed to be kinetically favored over the competitive diffusion-controlled electron transfer to form [Co(CO)(L<sup>N4</sup>)]<sup>+</sup> (Fig. 18, green).<sup>277</sup> The beneficial effect of visible-light irradiation on catalysis was further demonstrated by a substantial improvement of the observed FE for CO production during bulk electrolysis upon irradiation, suggesting that light-assisted electrocatalysis is an effective strategy to alleviate CO inhibition limitation. It is also worth noting that several reported Co aminopyridyl catalysts showed optimal performances under photochemical<sup>273,274,278,279</sup> or photoelectrochemical<sup>280</sup> conditions compared to pure electrochemical conditions.

A strikingly similar CO inhibition process has been reported to affect also the electrocatalytic performances of the non-heme [Fe(qpy)]<sup>2+</sup> complex (**63-Fe**, qpy = 2,2':6',2'':6'',2''':6'''-quaterpyridine).<sup>281</sup> In CH<sub>3</sub>CN, the electrochemically generated Fe<sup>I</sup> species engages a





**Fig. 18** Proposed unified mechanism for photo- and electrochemical CO<sub>2</sub> reduction to CO catalyzed by the molecular **1**<sup>(III)</sup> = [Co(L<sup>N4</sup>)(CH<sub>3</sub>CN)<sub>2</sub>]<sup>2+</sup> complex. The labile triflate ligands of compound **62** shown in Chart 5 are rapidly exchanged with coordinating solvent molecules in CH<sub>3</sub>CN, forming the doubly charged [Co(L<sup>N4</sup>)(CH<sub>3</sub>CN)<sub>2</sub>]<sup>2+</sup> complex. The picture shows the main proposed catalytic intermediates based on experimental evidence (dotted boxes) and DFT calculations. CPE: Controlled-potential electrolysis. Adapted with permission from ref. 277. Copyright 2020 American Chemical Society.

fast and irreversible CO<sub>2</sub> binding and, after protonation and reductive C–O bond cleavage, leads to the formation of a [Fe(CO)(qpy)]<sup>+</sup> adduct. Analogously to **62**, the CO release from [Fe(CO)(qpy)]<sup>+</sup> was found to compete with its further one-electron reduction to form the inactive neutral [Fe(CO)(qpy)]<sup>0</sup> species, detected by UV-Vis and FTIR-SEC. Such a deactivation process led to a low FE<sub>CO</sub> (48%) obtained during controlled-potential electrolysis at –1.2 V vs. SCE in the presence of 1 M PhOH, even though the system displayed an excellent CO selectivity over HER. A substantial improvement of the faradaic yield (70%) was gathered by using the light-assisted strategy.<sup>281</sup> Moreover, **63-Fe** revealed to be a very efficient and selective catalyst for visible light-driven CO<sub>2</sub> conversion to CO in pure homogeneous photochemical conditions<sup>282</sup> as well as in a hybrid system mixed with mesoporous graphitic carbon nitride.<sup>283</sup>

Notably, the Co quaterpyridine derivative, [Co(qpy)]<sup>2+</sup> (**63-Co**), displayed excellent electrocatalytic performances without any evidence of inhibition by CO poisoning.<sup>281</sup> In the presence of a large excess of added exogenous acid (3 M PhOH), the one-electron reduced Co<sup>I</sup> species reversibly binds two molecules of PhOH in axial position, forming the [Co<sup>I</sup>(qpy)(PhOH)<sub>2</sub>]<sup>+</sup> complex. Further reduction of the latter leads to the doubly-reduced active [Co<sup>I</sup>(qpy<sup>•-</sup>)(PhOH)<sub>2</sub>] species (the second electron is likely to be delocalized on the qpy moiety), responsible for a selective CO production (FE<sub>CO</sub> = 94%) at a very low overpotential (–1.1 V vs. SCE, η = 140 mV). Owing to the high observed catalytic rates and low overpotential, **63-Co** favorably compares with the most active reported molecular catalysts for CO<sub>2</sub>RR to CO and closely matches the performance of the highly efficient Fe<sup>0</sup> porphyrins (see Fig. 19).<sup>281</sup> In a related study, the use of high scan-rate cyclic voltammetry (up to 500 V s<sup>-1</sup>) shed light on the presence of an alternative reaction pathway dominant at low PhOH concentrations (<1.5 M).<sup>284</sup>

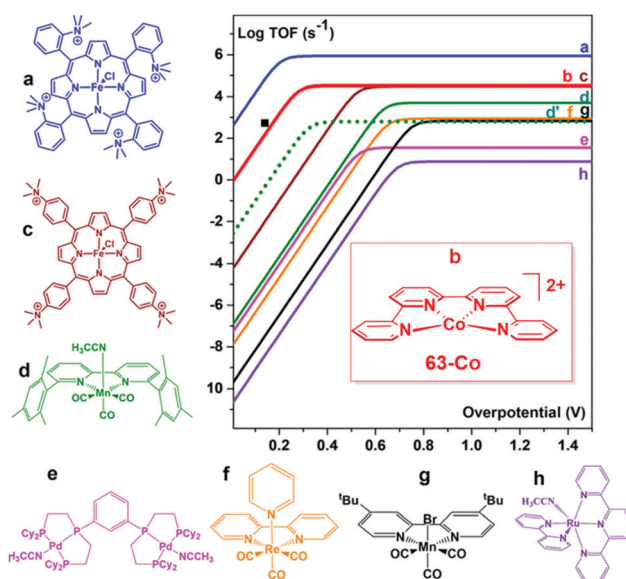


**Fig. 19** Catalytic Tafel plots of selected heme and non-heme molecular catalysts reported in the literature for the CO<sub>2</sub>-to-CO electrochemical conversion in DMF or CH<sub>3</sub>CN (a,<sup>112</sup> c,<sup>112</sup> d/d',<sup>289</sup> e,<sup>290</sup> f,<sup>291</sup> g,<sup>292</sup> h<sup>293</sup>). The catalysts a and c correspond to the catalysts **20** and **18** shown in Chart 1, respectively. The data for catalyst b (**63-Co**) refer to ref. 281 (■: TOF value for **63-Co** obtained from electrolysis data). Adapted with permission from ref. 281. Copyright 2018 American Chemical Society.

This mechanism, occurring at higher overpotential (η = 600 mV), is based on the formation of the active three-electron reduced [Co(qpy)]<sup>-</sup> species, which may undergo hydride formation with subsequent selectivity loss. Furthermore, the precursor [Co<sup>I</sup>(qpy<sup>•-</sup>)] species readily adsorbed on the electrode surface, as already reported in earlier studies.<sup>285</sup> Overall, high concentrations of added PhOH were found to enhance CO selectivity



over HER, decrease the overpotential and prevent intermediate adsorption on the electrode surface. An analogous beneficial effect of the added proton source on the catalyst stability was also observed for other classes of molecular Co catalysts.<sup>286</sup> Owing to the flat, conjugated geometry of the qpy ligand, [Co(qpy)]<sup>2+</sup> was successfully immobilized on MWCNTs, leading to one of the most efficient heterogenized molecular catalysts reported so far for CO<sub>2</sub>RR to CO in aqueous media.<sup>287</sup> At close to neutral pH (7.3), the [Co(qpy)]<sup>2+</sup>/MWCNTs electrode was able to quantitatively produce CO from CO<sub>2</sub> with excellent durability and at a very low applied overpotential (−0.35 V *vs.* RHE,  $\eta = 240$  mV).

The examples of macrocyclic and non-macrocyclic molecular systems discussed in this section suggest that both, electronic and structural factors should be taken into consideration to avoid CO inhibition, since flexible ligand geometries and electron-rich metal centers both contribute to stabilize CO adducts. In a recent study, McCrory and co-workers explored the catalytic behavior of a series of Co complexes with bis-(pyridylmonoimine)-based ligands of varying degrees of flexibility, suggesting a direct correlation between structural flexibility and catalytic CO<sub>2</sub>RR activity.<sup>288</sup> In particular, a structurally rigid and quasi-planar catalyst (complex **64** in Chart 5) was shown to feature a more negative onset potential for the catalytic wave but also the highest efficiency toward CO production in the presence of high amounts of an added proton source. On the other hand, derivatives with structurally more flexible architectures (**65–67**) resulted in a more positive onset potentials for catalysis, but at the expense of considerably lower FE<sub>CO</sub> values. As indicated by the higher CO binding equilibrium constants, lower CO dissociation constants and decreased activity under CO<sub>2</sub>/CO gas mixtures, the flexible Co systems were found to be more prone to CO poisoning during catalysis through the formation of stable Co<sup>I</sup>–CO carbonyl species, which was ascribed as the origin of the diminished overall activity.<sup>288</sup>

## 5. Single-atom catalysts

Single-atom catalysts (SACs) typically define a class of materials based on highly dispersed monometallic active sites embedded on a 2D conductive surface. The active site of SACs comprises not only the isolated single transition metal atom but also its three- or four-fold anchoring sites (typically C or N atoms), which mimic the role of the first coordination shell in molecular catalysis.<sup>294</sup> So far, the overwhelming majority of the SACs reported for CO<sub>2</sub>RR are based on M–N–C materials, whereby atomically dispersed 1st row transition metals are incorporated onto N-doped carbon supports.<sup>295</sup> The nature of the metal center and the structural features of the coordinative environment were found to strongly affect the CO<sub>2</sub>RR performance in terms of activity, selectivity and overpotential. The compact M–N<sub>3</sub> or M–N<sub>4</sub> configurations confined on a single carbon plane are the most commonly proposed moieties for the catalytic site of SACs, being reminiscent of the structures of molecular complexes with macrocyclic ligands employed as

efficient catalysts for CO<sub>2</sub> conversion to CO (Chart 6). However, although the effect of the surrounding carbon matrix has received considerably less attention, some groups have hypothesized a non-innocent role of the carbon atoms spatially close to the active site in the catalytic process.<sup>296,297</sup>

Hence, the SAC approach represents a promising strategy to tailor the electronic structure of the active site as means of controlling the reactivity toward CO<sub>2</sub>RR. In comparison with the corresponding metal-based bulk materials or NPs,<sup>14,298–300</sup> SAC systems generally possess unique catalytic properties, selectively promoting CO<sub>2</sub>RR over the competing HER in aqueous media. Recently, single-metal porphyrin-like sites were predicted to hinder the HER by forcing an on-top \*H adsorption as compared to the more energetically favorable hollow site binding of hydrogen on a bulk metal catalyst surface.<sup>301</sup> Mixing bulk materials and SACs can even be exploited to controllably adjust the H<sub>2</sub>/CO ratio, which could be used as further feed-stock for the Fischer–Tropsch process.

Despite the major benefits of SACs revealing high selectivity with maximal metal atom utilization, challenges related to the synthesis and structural characterization emerge. The availability, exclusivity and distribution of the SAC motifs on the prepared sample are critical for the development of SACs. Advanced characterization techniques like electron microscopy, X-ray absorption spectroscopy (XAS), Fourier-transform infrared (FTIR) spectroscopy or scanning tunneling microscopy (STM) can assist the design and the investigation of single-atom structures. In particular, aberration corrected TEM and high-angle annular dark-field STEM (HAADF-STEM) are common techniques used for the determination of the size and distribution of isolated metal atoms and to extract the local structural information.<sup>36</sup> Moreover, synchrotron radiation techniques allow the investigation of the overall chemical environment of the single metal atoms. A further challenge is the possible non-uniform functionalization of the carbon structure, which leads to a variety of active sites and their irregular distribution on the support.<sup>302</sup> In the case of M–N–C materials, a number of different nitrogen atom functionalities (*e.g.* pyrrolic, pyridinic, graphitic, *etc.*) are potential competitive coordination sites for the metal or may act themselves as metal-free catalytic sites for CO<sub>2</sub>RR, changing neutrality, altering charge and spin densities and promoting thermodynamic stability.<sup>296,303–305</sup> Furthermore, aggregation phenomena should be considered in the investigation of SACs. Indeed, SACs tend to aggregate into clusters or NPs during the catalytic process or storage due to their thermodynamic instability, high surface free energies and low coordination. Therefore, their stability under reaction conditions should be demonstrated. Other factors related to the reaction conditions, such as pH and electrolyte, may also have a strong influence on their catalytic response.

In a recent study, a series of M–N–C model catalysts with different earth-abundant transition metals (M = Mn, Fe, Co, Ni, Cu) have been explored for CO<sub>2</sub>RR in aqueous media, in order to systematically rationalize the effect of the nature of the metal center on the catalytic activity and selectivity.<sup>306</sup> All the materials featured atomically dispersed in-plane M–N<sub>4</sub> moieties, with negligible structural and morphological differences across the series.





Chart 6 Schematics of the main  $M-N_x-C_x$  coordinative configurations explored for single-site catalysts for  $CO_2RR$  to CO atomically dispersed catalysts on a 2D carbon support.

This allowed a direct correlation between the  $CO_2RR$  performances and the type of metal (alternative configurations with one or two adsorbed axial  $H_2O$  molecules have also been considered,  $M-N_4-H_2O$ ). The catalytic  $CO_2RR$  tests at  $-0.5$  V and  $-0.6$  V vs. RHE (pH 6.7), resulted in a volcano-like diagram, with the Fe-N-C and Co-N-C catalysts being the most active

(partial  $j_{CO}$ ), depending on the applied potential (Fig. 20a and b). However, the Fe-, Mn- and Ni-N-C catalysts revealed to be the most selective toward CO production across the series ( $FE_{CO} > 80\%$ ), whereas the high current densities for the Co-N-C counterpart predominantly accounted for  $H_2$  evolution (Fig. 20a). *Operando* XANES was also performed to monitor the changes in



Fig. 20 (a) FE at  $-0.6$  V (up) and  $-0.5$  V (bottom) vs. RHE obtained over the  $M-N-C$  catalysts ( $M = Mn, Fe, Co, Ni, Cu$ ) for 90 min electrolysis under  $CO_2$ -saturated  $0.1$  M  $KHCO_3$  aqueous electrolyte (pH 6.7) at room temperature. (b) Comparison of experimental CO partial current density at  $-0.6$  V vs. RHE for pyrolyzed  $M-N-C$  materials and DFT calculated trends ( $U = -0.6$  V vs. RHE).  $E_{RDS}$  is the calculated free reaction energy at the specific RDS of  $CO_2RR$  to CO for each active site. (c) Octahedral, square pyramid and square planar symmetry (orange indicates the antibonding states). (d) The experimental selectivity at  $-0.6$  V vs. RHE over Fe-N-C, Co-N-C, and Ni-N-C vs. the DFT-simulated  $E(*CO_2^-) - E(*H)$ .<sup>306</sup> Adapted with permission from ref. 306. Copyright 2019 American Chemical Society.



the oxidation state under catalytic conditions, suggesting that it remained unchanged during CO<sub>2</sub>RR for Co(2+) and Mn. It was partially reduced for Fe and Ni (from 3+/2+ to 2+ for Fe, and from 2+ to 1+ for Ni), while it was strongly reduced to Cu<sup>0</sup> in the case of Cu.<sup>306</sup> The experimental results were rationalized by using DFT calculations, which modeled the binding energies of the key intermediates involved in the CO<sub>2</sub>RR process, according to four elementary steps: (i) CO<sub>2</sub> + e<sup>-</sup> → \*CO<sub>2</sub><sup>-</sup>; (ii) \*CO<sub>2</sub><sup>-</sup> + H<sup>+</sup> → \*COOH; (iii) \*COOH + H<sup>+</sup> + e<sup>-</sup> → \*CO + H<sub>2</sub>O; (iv) \*CO → CO. The rate-determining step (RDS) was found to be highly dependent on the nature of the metal center, being the \*CO desorption step (step iv) for Mn-N<sub>4</sub> and Fe-N<sub>4</sub> moieties or the CO<sub>2</sub> activation and first electron transfer for Ni-N<sub>4</sub> and Cu-N<sub>4</sub> (step i). In the series, the Co-N<sub>4</sub> sites showed an optimum balance between the energy barriers for CO<sub>2</sub> activation and CO desorption. In particular, the CO<sub>2</sub>RR activity across the series was rationalized in terms of the Gibbs free energy change at the rate-determining step (*E*<sub>RDS</sub>), resulting in a volcano trend analogous to the experimental one (Fig. 20b).<sup>306</sup> According to this diagram, M<sup>2+</sup>-N<sub>4</sub>-H<sub>2</sub>O sites were proposed as the most active centers in Fe-N-C and Co-N-C, whereas the Ni<sup>1+</sup>-N<sub>4</sub> configuration was predicted to be the most active in Ni-N-C, in analogy to the macrocyclic Ni molecular catalysts (see Section 4.1.1). Moreover, the difference between the binding energies for \*CO<sub>2</sub><sup>-</sup> and \*H was proposed as a suitable descriptor to predict selectivity toward CO production, showing a direct correlation to the number of d-antibonding electrons, which is determined by the basic principles of coordination chemistry according to the crystal field splitting theory (Fig. 20c and d).<sup>306</sup> Following this approach, the high selectivity experimentally observed for Fe and Ni catalysts could be reproduced, as well as the more favourable HER promoted by Co-N-C.<sup>306</sup>

This representative example shows the crucial role played by the metal center in determining the catalytic activity and selectivity of a series of single-site catalysts featuring similar coordinative environments. In the next paragraphs, we aim to explore the different types of metal coordination proposed for the main families of SACs (Chart 6).

### 5.1 Ni-N-C catalysts

An indicator of the growing interest in Ni-N-C catalysts is given by the increasing amount of studies published in the last years. Most of these reports mainly focus on the development of novel synthetic procedures to obtain efficient Ni-N-C catalysts, aiming to preserve coordinatively unsaturated Ni-N sites confined into N-doped 2D materials.<sup>307–309</sup> The most common synthetic approach consists in a simple pyrolysis of a Ni salt with N-doped carbon materials obtained from N-rich organic molecules. For instance, the dispersion of Ni sites in a N-doped carbon matrix obtained from dicyandiamide and 2-methylimidazole led to a catalyst displaying maximum FE<sub>CO</sub> 97% at -0.9 V vs. RHE.<sup>309</sup> In another study, an increased content of pyrrolic-N centers in N-doped carbon hollow spheres was obtained by modulating the concentration of the melamine precursor, remarkably increasing the density of Ni sites and, in turn, the catalytic CO<sub>2</sub>RR activity.<sup>310</sup> Metal-organic Ni complexes containing nitrogen ligands, such as [Zn(Ni)-bidppz]

(bidppz = 11,11'-bis(dipyrido[3,2-*a*:2',3'-*c*]phenazinyl))<sup>308</sup> or Ni(NH<sub>3</sub>)<sub>6</sub>I<sub>2</sub>,<sup>311</sup> were also employed as suitable precursors to achieve robust Ni-N-C SACs for selective CO<sub>2</sub>-to-CO reduction. Remarkably, Wu and coworkers recently reported a Ni SAC containing well-defined Ni-N<sub>4</sub> sites synthesized through a topochemical transformation of a Ni-doped g-C<sub>3</sub>N<sub>4</sub> sample with a carbon layer. A combination of XAS data and TEM/HAADF-STEM images proved the retention of the preformed Ni-N<sub>4</sub> structures (Ni units coordinated to pyridinic-N) upon the thermal treatment and the lack of agglomeration of the Ni atoms to form particles.<sup>312</sup> The Ni-N<sub>4</sub> moieties, which are reminiscent of the structure of the Ni cyclam molecular catalyst, were supposed to be responsible for the excellent CO<sub>2</sub>RR activity, producing CO in high faradaic yields (99%) at -0.81 V vs. RHE.

Further research provided a more in-depth structural characterization of the Ni-N<sub>4</sub> active site and their role in the CO<sub>2</sub>RR, revealing several similarities with the molecular Ni-based N<sub>4</sub> macrocyclic systems. Recently, a detailed XAS and XPS study allowed the elucidation of the structural features of the active moiety in a robust and highly CO-selective Ni SAC dispersed on an N-doped graphene matrix (A-Ni-NG, see Fig. 21).<sup>313</sup> The isolated Ni-N<sub>4</sub> moieties displayed a distorted square-planar geometry which deviates from the canonical D<sub>4h</sub> symmetry typical of the NiPc molecular derivative. Moreover, XAS and EPR measurements confirmed the presence of monovalent paramagnetic Ni<sup>I</sup> centers with a 3d<sup>9</sup>, S = 1/2 electronic configuration, which possess a high intrinsic reactivity due to the partially filled 3d<sub>x<sup>2</sup>-y<sup>2</sup></sub> orbitals. In analogy with the molecular Ni cyclam-like derivatives, the initial Ni<sup>I</sup> state is responsible for the CO<sub>2</sub> binding step, as confirmed by *operando* XAS data, Fig. 21. Just by adding CO<sub>2</sub> to the electrolyte solution at open-circuit voltage (OCV), the Ni K-edge was found to shift to higher energy, ca. 0.4 eV with respect to the spectrum recorded under Ar atmosphere, indicating an increase of the Ni oxidation state, Fig. 21a. These results are consistent with a charge transfer from the Ni<sup>I</sup> center to the C 2p orbital of the bound CO<sub>2</sub> molecule to form an adsorbed \*CO<sub>2</sub><sup>δ-</sup> species, similarly to what it was observed for Co cyclam-like complexes (Fig. 21c).<sup>246</sup> Nonetheless, there was no clear evidence of charge transfer from the Ni center to CO<sub>2</sub> in the case of the [Ni(CO<sub>2</sub>)(cyclam)]<sup>+</sup> adduct (see above).<sup>11</sup> When a bias potential (at -0.7 V vs. RHE) is applied under CO<sub>2</sub>, a shift of the Ni K-edge back to lower energies was observed, suggesting the regeneration of the starting Ni<sup>I</sup> state after the completion of a single two-electron CO<sub>2</sub>-to-CO turnover, Fig. 21a. Interestingly, an observable shift of the main EXAFS peak to longer lengths during CO<sub>2</sub>RR (at -0.7 V vs. RHE) is indicative of an out-of-plane distortion from the planar Ni-N<sub>4</sub> graphene configuration, probably due to a redistribution of the electron density in the 3d orbitals of Ni between the 4 Ni-N bonds and the Ni-C bond, Fig. 21b. As previously discussed, significant distortions in the macrocyclic geometry have been predicted to stabilize the axial Ni-CO bond and disfavor CO dissociation from the [Ni(cyclam)(CO)]<sup>+</sup> intermediate, and are supposed to be at the origin of the CO inhibition phenomenon affecting the homogeneous Ni-cyclam system.<sup>217</sup> The geometrical constraints forced by the graphene framework may prevent an excessive distortion of the square-planar cyclam-like Ni active site,



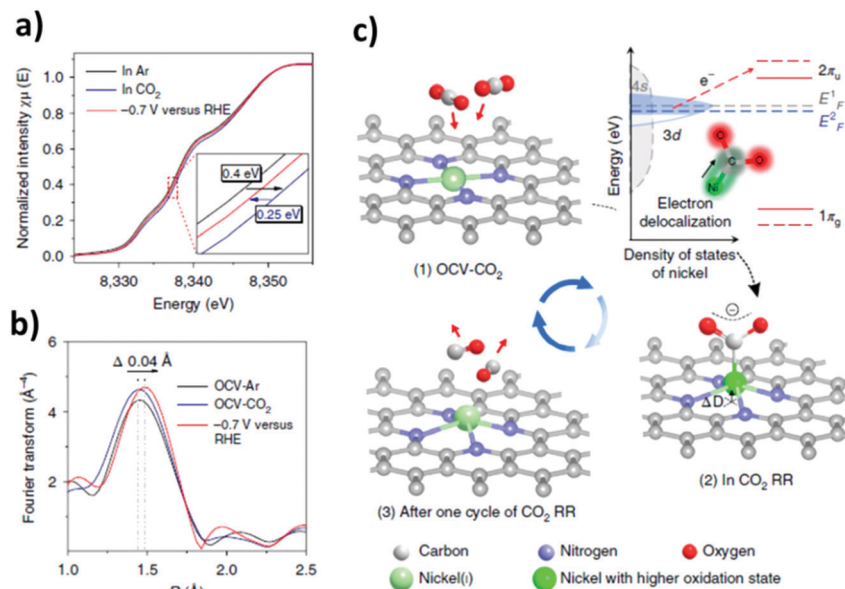


Fig. 21 *Operando* XAS data from ref. 313. (a) Normalized Ni K-edge XANES spectra (enlarged in the inset) and (b) Fourier transform magnitudes of EXAFS spectra (without phase correction) of A-Ni-NG. (c) Dynamic structural changes of the active site during CO<sub>2</sub> activation and electroreduction.  $\Delta D$ : out-of-plane displacement of Ni atom resulting from charge transfer from the Ni<sup>I</sup> atom to CO<sub>2</sub>.  $E_F^1$  and  $E_F^2$ : Fermi levels of A-Ni-NG before and after formation of Ni-CO<sub>2</sub><sup>δ-</sup>, respectively.  $1\pi_g$  and  $2\pi_u$ : CO<sub>2</sub> molecular orbitals.<sup>321</sup> Adapted with permission from ref. 313. Copyright 2018 Nature Publishing Group.

ensuring a more efficient CO release step as compared to the Ni-cyclam homogeneous counterpart. As above mentioned, the electrode-flattened cyclam structure of the adsorbed [Ni(cyclam)-(CO)]<sup>+</sup> complex has been proposed to be responsible for the enhanced catalytic rates observed for [Ni(cyclam)]<sup>2+</sup> on a Hg electrode in comparison with the homogeneous derivative.<sup>217,226</sup> Analogous trends correlating the planarity of the ligand scaffold to a more efficient CO release step were also previously discussed for other families of molecular catalysts (see Section 4).<sup>288</sup>

The unique properties of Ni-N<sub>4</sub> motifs in promoting an efficient CO<sub>2</sub>RR have been demonstrated in several other recent reports. These materials are generally obtained by facile adsorption of Ni<sup>2+</sup> ions on N-doped graphene<sup>314</sup> or a porous carbon matrix.<sup>315</sup> However, well-defined organometallic Ni complexes containing pre-formed Ni-N<sub>4</sub> coordination units can be adopted as single-site precursors of SACs, being the source of both, metal and nitrogen at a time. Notably, the local coordination environment of the active site in the Ni SAC is highly dependent on the structure of the original complex precursor and the type of support material. For instance, the annealing of a Ni complex with a flexible tripodal nitrogen ligand led to a SAC containing distorted square-planar Ni<sup>II</sup>-N<sub>4</sub> species uniformly dispersed over GO sheets, which displayed superior CO<sub>2</sub>RR performance than the molecular derivative.<sup>316</sup> The presence of GO in the synthetic process was found to play an essential role in preventing the formation of metallic bulk NPs which reduce the catalytic activity.

In another study, a Ni SAC synthesized by C-C coupling of a Ni phthalocyanine precursor (NiTAPc) with CNTs served as a model system to investigate the mechanism for electrochemical CO<sub>2</sub>RR.<sup>317</sup> This approach resulted in the formation of uniformly distributed Ni-N<sub>4</sub> moieties with a canonical *D*<sub>4h</sub> symmetry and

Ni<sup>II</sup> oxidation state, almost identical to the original sites of the NiTAPc precursor. A combination of *operando* XAS, *operando* Raman and NAP-XPS provided insights into the dynamic changes of the electronic state of Ni during CO<sub>2</sub>RR, indicating that the initial Ni<sup>II</sup> species does not interact with CO<sub>2</sub>, yet the low-valent reduced Ni<sup>I</sup> state is the species responsible for CO<sub>2</sub> activation. These results are consistent with those previously discussed for another Ni SAC (*vide supra*) and establish a direct correlation with the behavior of molecular Ni cyclam-like systems whereby the Ni<sup>I</sup> state is the catalytically active species.<sup>11</sup> The proposed pathway for CO<sub>2</sub>RR to CO on the Ni SAC is analogous to the one proposed for molecular Ni catalysts with N<sub>4</sub> macrocyclic ligands (see Scheme 2).<sup>215</sup> This involves the initial reduction of Ni<sup>II</sup> to Ni<sup>I</sup>, which then undergoes an electrophilic addition of CO<sub>2</sub> to form the adsorbed \*CO<sub>2</sub><sup>-</sup> intermediate, with electron delocalization from the Ni center to the bound CO<sub>2</sub> molecule. As aforementioned, only moderate charge transfer from the Ni<sup>I</sup> center to coordinated CO<sub>2</sub> was observed for the molecular [Ni(CO<sub>2</sub>)(cyclam)]<sup>+</sup> adduct.<sup>11</sup> In agreement with the experimental Tafel slope and the reaction orders for H<sup>+</sup>/CO<sub>2</sub>, the next hydrogenation step, \*CO<sub>2</sub><sup>-</sup> + H<sup>+</sup> → \*COOH, was found to be rate-limiting, followed by the formation of the adsorbed \*CO intermediate and the final release of gaseous CO from the surface.

The control over the coordination environment of the Ni-N-C material has been suggested to be critical to achieve an efficient CO<sub>2</sub>RR. Although “cyclam-like” macrocyclic Ni-N<sub>4</sub> moieties are generally proposed as the active sites in several reported Ni-N-C SACs, alternative configurations have been recently predicted to display high intrinsic CO<sub>2</sub>RR activity. Moreover, the high annealing temperature usually required for the synthesis of Ni-N-C materials may generate defects in the carbon matrix, making the identification of the active site



even more challenging. In particular, the role of C species in the coordination of the Ni atoms has been considered. Wang and co-workers explored the CO<sub>2</sub>RR performances of different Ni sites in graphene vacancies containing various Ni–C/Ni–N coordination environments.<sup>318</sup> They observed that the incorporation of N-dopants induced remarkable changes in the morphology of the Ni sites but also greatly improved the selectivity towards CO production. More recently, a general host–guest cooperative protection strategy based on the introduction of polypyrrole into bimetallic MgNi–MOF-74, followed by a pyrolysis step, allowed to obtain Ni SACs with tunable N/C coordination by controlling the annealing temperature.<sup>319</sup> The hybrid Ni<sub>SA</sub>–N<sub>2</sub>–C material with the lowest N coordination number (2) showed the best performance across the series, affording a maximum FE<sub>CO</sub> 98% at –0.8 V vs. RHE. By using theoretical and experimental tools, Yamauchi and co-workers systematically investigated a series of hybrid Ni–N<sub>x</sub>C<sub>4–x</sub> (x = 0–4) moieties containing different combinations of coordinating N or C atoms in an attempt to elucidate the role of C atoms on the structural and catalytic properties of Ni N–C SACs.<sup>320</sup> For each configuration, the thermodynamic barrier associated to each of the three elementary steps of the CO<sub>2</sub>RR pathway were compared, *i.e.* the \*COOH formation (\* + CO<sub>2</sub> + H<sup>+</sup> + e<sup>–</sup> → \*COOH), the \*CO formation (\*COOH + H<sup>+</sup> + e<sup>–</sup> → \*CO + H<sub>2</sub>O) and CO desorption (\*CO → \* + CO). Looking at the electronic structure, it was found that C-rich configurations tend to lead to an increase in the electron density over the Ni atom, favouring the CO<sub>2</sub> activation step at the expense of a stronger interaction with adsorbed CO. On the other hand, an increase in the N coordination number facilitates the CO desorption step, yet limiting the nucleophilicity of the Ni center. Overall, the Ni–N<sub>4</sub> sites are limited by the first electrochemical step, showing the highest barrier for \*COOH formation, whereas CO desorption is energetically unfavorable for Ni–C<sub>4</sub> moieties. Therefore, the Ni–N<sub>2</sub>C<sub>2</sub> configuration was predicted to be the optimum structure for CO<sub>2</sub>RR, displaying the best compromise between these opposite tendencies. The experimental data corroborated the theoretical predictions, since Ni–N–C materials containing mixed N/C coordination synthesized at intermediate carbonization temperatures provided the best results in terms of activity and selectivity towards CO production.<sup>320</sup> Interestingly, the coordinative motif of Ni–N<sub>2</sub>C<sub>2</sub> moieties homogeneously dispersed on a 2D graphene layer shows structural analogies with an efficient homogeneous Ni catalyst bearing a macrocyclic ligand based on a redox-active 2,2′-bipyridyl core and electron-rich N-heterocyclic carbene (NHC) donors (**54-Ni**), previously discussed in the Section 4.2.<sup>258</sup> In particular, the optimal 15-membered macrocyclic configuration forced the molecular Ni system **54-Ni** to a distorted square-planar arrangement which is consistent with synchrotron-based experimental data on analogous Ni–N<sub>2</sub>C<sub>2</sub> SACs.<sup>320</sup> For the molecular Ni derivative **54-Ni**, the contribution of the quasi-planar ligand environment to extra-electron delocalization revealed to be decisive to prevent the formation of a metal-hydride species.

The question on the optimal coordination structure in Ni–N–C SACs is however still under debate, due to the possible heterogeneities that can be found in the real materials, as well

as the extreme difficulty to unambiguously characterize experimentally the local coordinative environment of a catalyst and to precisely control its structure/composition through synthetic parameters. Moreover, DFT calculations based on the so called Computational Hydrogen Electrode (CHE) model may also lead to an oversimplified description of the system.<sup>322</sup> Recently, the kinetic barriers for the CO<sub>2</sub>RR pathway promoted by several hybrid Ni–N/C coordination sites were calculated by using *ab initio* molecular dynamics (AIMD), proposing the mixed Ni–N<sub>1</sub>C<sub>3</sub> configuration to be the most active and selective site for CO<sub>2</sub>RR.<sup>322</sup> Importantly, the study shed light on the site charge capacity and the H-bonding interactions as the crucial factors determining the activity and selectivity of a given SAC. The former describes the number of charges the site can carry and contributes to lower the barrier for the electrochemical steps, yet might be detrimental for an efficient CO desorption. Furthermore, the H-bonding interactions with water molecules of the medium are essential to assist the initial chemisorption of CO<sub>2</sub> on the surface, stabilize the intermediates and facilitate the protonation steps. It is remarkable to note that the beneficial effect of cooperative H-bonding interactions on CO<sub>2</sub>RR was demonstrated for the [Ni(cyclam)]<sup>2+</sup> molecular catalyst in water and in organic electrolytes (Section 4.1).<sup>230</sup> In particular, the presence of an urea-based exogenous additive led to a significant enhancement of the catalytic response of [Ni(cyclam)]<sup>2+</sup> due to its ability to form cooperative multipoint hydrogen-bond interactions (Fig. 14), without altering the selectivity of the process. Moreover, we have already discussed the beneficial role of water or polar solvents on CO<sub>2</sub> binding, activation and conversion observed for Ni and Co tetraazamacrocyclic complexes (Section 4.1).<sup>11,210,243,247</sup>

In contrast with the predominant literature on Ni N–C SACs, some reports have suggested that coordinatively unsaturated Ni–N moieties are preferential catalytic sites for CO<sub>2</sub> binding and conversion, decreasing the affinity for HER.<sup>323,324</sup> For example, some Ni–N active sites confined on porous carbon with different coordination numbers were synthesized by pyrolysis of a Zn/Ni bimetallic zeolitic imidazolate framework-8 (ZIF-8), displaying a high CO selectivity (FEs 92–98%) over a broad potential window (–0.53 V to –1.03 V vs. RHE). In agreement with the low Ni coordination numbers experimentally observed by EXAFS analysis, computational data suggested that unsaturated Ni–N<sub>2</sub>V<sub>2</sub> (V stands for coordination vacancy) possess a lower free energy for the formation of the \*COOH intermediate as compared to the Ni–N<sub>4</sub> sites.<sup>324</sup> An impregnation-pyrolysis method using a highly-defective sponge-templated GO support was suggested to favor the formation of analogous coordinatively unsaturated Ni sites, due to the trapping of Ni atoms in the material defects.<sup>325</sup> In another study, a pyrrolic Ni–N<sub>3</sub> moiety was proposed as the catalytically relevant configuration for a highly active Ni SAC confined within a porous N-doped carbon sheath.<sup>326</sup> Nakanishi and co-workers adopted a Covalent Triazine Framework (CTF), consisting of microporous conjugated polymers with 1,3,5-triazine linker units, as a suitable platform to favor the formation of coordinatively unsaturated metal SACs.<sup>327</sup> Upon the impregnation of Ni<sup>2+</sup> ions into the reticular structure, the resulting porous



material (Ni-CTF) displayed a lower Ni–N coordination number (close to 3) than the Ni-TPP reference, with Ni sites analogous to terpyridyl or iminopyridyl molecular Ni units embedded into a polymeric matrix.<sup>328–330</sup> As corroborated by DFT calculations, which suggest a more favorable free energy barrier for \*COOH formation for Ni–N<sub>3</sub> sites as compared to Ni–N<sub>4</sub> moieties, Ni-CTF was found to outperform Ni-TPP for CO<sub>2</sub>RR, leading to a FE<sub>CO</sub> ca. 90% at –0.8 V vs. RHE.<sup>327</sup>

The influence of the carbon matrix should be also taken into account to rationalize the CO<sub>2</sub>RR performances of Ni–N–C materials. For instance, pendant residues located in the second or outer coordination sphere may actively participate in the catalytic CO<sub>2</sub>RR pathway of the SAC, as widely demonstrated for several enzymatic systems and artificial molecular electrocatalysts (see Sections 3 and 4).<sup>48</sup> In this regard, Ni–N<sub>2+2</sub>–C<sub>8</sub> structures located at the edge between two adjacent carbon sheets were predicted to promote an energetically more favorable pathway for CO<sub>2</sub> reduction to CO, as compared to the isolated bulk-hosted Ni–N<sub>4</sub>–C<sub>10</sub> sites confined within a single graphitic layer.<sup>296</sup> This is due to the capability of uncoordinated carbon atoms with dangling bonds close to the catalytic site to assist the dissociation of the \*COOH intermediate. Moreover, the optimization of the physicochemical properties of the support material revealed to be an effective approach to enhance the catalytic performance of Ni–N–C catalysts. More specifically, an increased porosity and a high density of defects on the carbon support have been shown to facilitate fast CO<sub>2</sub> mass transport and enhance the incorporation of the single metal atoms, contributing to boost the catalytic activities of the Ni–N–C catalysts.<sup>323,331–333</sup> Yang and co-workers explored a top-down strategy *via* thermal atomization to prepare N–C materials enriched with Ni single atoms, by trapping the latter on the surface defects of the N-doped carbon matrix. This approach was found to improve the atomic distribution of the active sites on the support surface, positively impacting the CO<sub>2</sub>RR activity, selectivity to CO (FE<sub>CO</sub> > 90% between –0.6 V and –1.0 V vs. RHE) and durability of the catalyst.<sup>331</sup> In another report, a highly porous and surface defect-rich microwave exfoliated graphene oxide was used as support to disperse N-coordinated Ni atoms.<sup>332</sup> The abundant defects on the pore edges favored the anchoring of the Ni atoms, leading to high selectivity and mass activity.

By virtue of the promising catalytic properties of Ni SACs, some efforts have been recently done to implement them in real devices by using Gas Diffusion Electrodes (GDE) in order to achieve commercially relevant current densities. A reactive three-phase interface is prepared by feeding gaseous CO<sub>2</sub> from the back of a GDE to optimize the accessibility of CO<sub>2</sub> to the catalyst surface. This setup overcomes the limitation of the low CO<sub>2</sub> solubility and mass transfer in aqueous electrolyte. A few recent reports afforded high current densities over 300 mA cm<sup>–2</sup> with selective CO production,<sup>334–336</sup> reaching a maximum of FE<sub>CO</sub> 90% between 100 and 200 mA cm<sup>–2</sup>.<sup>334</sup> Albeit exhibiting similar performances as the benchmark AgO<sub>x</sub> catalyst in an H-type cell (Fig. 22a), the Ni–N–C catalysts showed higher current densities and less dramatic FE decrease for CO production in the

electrolyzer setup (Fig. 22b). Recently, commercially relevant current densities for CO production (308 mA cm<sup>–2</sup>) with excellent selectivity (FE<sub>CO</sub> 88%) could be sustained for up to 120 hours by using a flexible and robust Ni SAC-decorated porous carbon membrane as GDE.<sup>315</sup> The highly hydrophobic structure was found to favor CO<sub>2</sub> adsorption and possess higher electrochemical active surface area as well as low electric resistance.

## 5.2 Fe–N–C catalysts

Due to its extreme earth-abundance, the utilization of catalysts based on Fe for efficient CO<sub>2</sub> conversion to CO is highly desirable. Jaouen, Fontecave and co-workers studied the effect of different ratios of Fe-SACs and Fe-NPs on the catalytic performance in a series of Fe–N–C materials, establishing a correlation between the catalyst structure and CO<sub>2</sub>RR activity/selectivity.<sup>298</sup> Depending on the synthesis, different amounts of atomically dispersed Fe atoms or particles were obtained in the N–C materials, which was found to strongly affect the CO<sub>2</sub>RR performance. In particular, isolated square-planar Fe–N<sub>4</sub> moieties were found to be the active species for a selective CO production (FE<sub>CO</sub> up to 80% at –0.5 V vs. RHE), whereas heterogeneous Fe-based species (*e.g.* NPs or carbides) mainly produced H<sub>2</sub> under similar conditions. Interestingly, the higher the fraction of crystalline Fe, the higher the FE for H<sub>2</sub>. These results showed that the Fe speciation within the Fe–N–C material strongly affects the CO/H<sub>2</sub> ratio, being attractive in the perspective of using non-expensive catalysts to produce CO/H<sub>2</sub> mixtures useful for Fischer–Tropsch technologies. Although the crucial role of Fe on CO<sub>2</sub>RR in Fe–N–C catalysts has been verified by passivating the metal center with the coordinative SCN<sup>–</sup> ion leading to a decreased activity,<sup>337</sup> the identification of the real active site responsible for the catalytic behavior of Fe–N–C systems is still under debate. For instance, some studies reported that a high CO selectivity can be even achieved by using metal-free N–C materials, albeit exhibiting considerably lower current densities than those obtained in the presence of Fe.<sup>338</sup> Moreover, the mismatch experimentally observed between the CO<sub>2</sub>RR activity trends for a series of M–N–C (M = Fe, Co, Ni) and the corresponding molecular metalloporphyrins, suggests that ideal M–N<sub>4</sub> active sites are only a rough approximation of the real catalytic units in M–N–C materials and that the interactions with the surrounding carbon matrix may play a relevant role in catalysis.<sup>338</sup>

By using a combined experimental and theoretical approach, Pan *et al.* investigated the structural features of isolated Fe–N<sub>4</sub> moieties on a carbon matrix synthesized by thermal activation of Fe-doped ZIF-8.<sup>297</sup> Synchrotron-based XAS measurements confirmed the presence of discrete Fe–N<sub>4</sub> sites containing Fe centers predominantly in 3+ oxidation state. However, Mössbauer spectroscopy suggested the co-existence of two different types of Fe–N<sub>4</sub> structures within the Fe–N–C sample: planar bulk-hosted Fe–N<sub>4</sub>–C<sub>10</sub> units fully embedded in a 2D graphitic layer, and out-of-plane distorted edge-hosted Fe–N<sub>2+2</sub>–C<sub>8</sub> sites (see Chart 6). The latter bridge two armchair-like N-doped graphitic layers through the coordination between a Fe atom and 2 N heteroatoms exposed at





Fig. 22 (a) Catalytic performance (geometric CO current density) and product analysis (FE) of N-C (black), Fe-N-C (red), Ni-N-C (blue) and AgO<sub>x</sub> (cyan) catalysts measured in a H-type cell displayed as a function of the applied electrode potential. (b) Electrolyzer test results under controlled current densities (galvanostatic operation). The CO partial current density as a function of the electrode potential and the faradaic CO efficiency as a function of the applied electrolyzer current density are shown. All tests were performed in a CO<sub>2</sub>-saturated 1 M KHCO<sub>3</sub> electrolyte and 1 mg cm<sup>-2</sup> catalyst loading. Adapted with permission from ref. 334. Copyright 2019, Royal Society of Chemistry.

the edges. According to computational DFT data, CO<sub>2</sub>RR is predicted to occur more favorably at the edge-hosted Fe-N<sub>2+2</sub>-C<sub>8</sub> configuration, due to the beneficial role of the neighboring C atoms with dangling bonds to facilitate the key \*COOH dissociation step.<sup>297</sup> These data emphasize the importance of the specific interaction between the active site and the hosting environment in controlling the activity and selectivity of Fe-N-C SACs, suggesting analogous outer coordination sphere effects observed in homogeneous Fe systems with heme<sup>112,120,124-126,131</sup> or non-heme ligands<sup>267</sup> (see Sections 3 and 4).

An *in situ* infrared spectroscopy study in attenuated total reflection mode (ATR-IR) on a model Fe-N-C catalyst containing Fe-N<sub>4</sub> sites provided useful insights into the nature of the catalytically relevant units in Fe-N-C materials and the main factors limiting their activity (Fig. 23a).<sup>339</sup> When the applied potential matched the foot of the catalytic wave, an absorption band near 1900 cm<sup>-1</sup> started to grow, indicating the formation of a \*CO species adsorbed on the surface, as further confirmed by control experiments under CO atmosphere (Fig. 23b). In agreement with a \*CO inhibition process, its intensity did not decrease significantly after purging the solution with Ar and applying more negative potentials, suggesting the formation of a spectator deactivation species rather

than an on-cycle intermediate (Fig. 23c and d). In order to determine which sites could be affected by \*CO poisoning, DFT calculations suggested that bulk-hosted Fe-N<sub>4</sub> and edge-hosted Fe-N<sub>2+2</sub> structures are catalytically inactive, since both of them displayed a prohibitively strong \*CO adsorption. Contrariwise, Fe-N<sub>4</sub> units within graphitic pores of a defect-rich Fe-N-C material are considered the active sites for CO<sub>2</sub>RR to CO, due to a local electronic effect of the pore environment which contributes to weaken the Fe-C bond.<sup>339</sup> As previously discussed (Section 4), the formation of stable metal carbonyl deactivating species during CO<sub>2</sub>RR has been experimentally detected for several homogeneous Ni and Co systems based on non-heme N<sub>4</sub> macrocyclic<sup>217</sup> or aminopyridyl<sup>277,288</sup> ligands. A molecular CO scavenger<sup>217</sup> or light irradiation<sup>277</sup> were successfully used as alternative strategies to alleviate the CO inhibition and favor catalyst regeneration in molecular systems (see Section 4). In a similar fashion, the formation of an inactive Fe carbonyl species (detected by *in situ* UV-Vis and FTIR SEC) was also found to limit the electrocatalytic CO<sub>2</sub>RR performance of the 63-Fe homogeneous catalyst in organic electrolytes at low overpotentials, leading to low faradaic efficiencies for CO production (Section 4.3). It is worth noting that this complex contains a well-defined Fe-N<sub>4</sub> moiety, which is structurally





Fig. 23 (a) Scheme of the setup. (b) Real-time ATR-IR spectra recorded while stepping the potential of the Fe–N–C-loaded Au/Si prism in the CO<sub>2</sub>-saturated 0.5 M KHCO<sub>3</sub>. (c) Real-time IR spectra and (d) the evolution of the integrated \*CO band intensity when switching the CO/Ar atmosphere and potential. IR references were taken at 0 V for panel (b) and 0.1 V for panel (c). Adapted with permission from ref. 339. Copyright 2019 American Chemical Society.

similar to the sites accessible in the Fe–N–C SACs.<sup>281</sup> Similarly to other molecular systems, visible-light irradiation significantly improved the catalytic performance.<sup>281–283</sup>

A recent experimental study carried out by Chen, Hu and co-workers provided a significant improvement in the elucidation of the structure–activity relationship in Fe–N–C SACs, establishing a direct correlation between coordinative environment, metal oxidation state and catalytic CO<sub>2</sub>RR activity.<sup>340</sup> In this work, a Fe–N–C material featuring a porphyrin-like Fe<sup>3+</sup>–N<sub>4</sub> pyrrolic coordination environment, displayed an outstanding activity for CO<sub>2</sub>RR to CO in a flow-cell setup, affording  $j_{\text{CO}} = 94 \text{ mA cm}^{-2}$  at  $-0.45 \text{ V vs. RHE}$  with FE<sub>CO</sub> > 90%. *Operando* XAS at  $-0.4 \text{ V vs. RHE}$  revealed that the oxidation state of Fe remained unchanged during sustained CO<sub>2</sub>RR, likely due to a strong electronic coupling with the conductive support, as recently reported for some electrode-conjugated molecular sites.<sup>341,342</sup> However, at more negative applied potentials ( $< -0.5 \text{ V vs. RHE}$ ) a decreased stability of the catalytic system was observed concomitantly with an apparent shift to lower energies of the Fe K-edge, indicating a Fe<sup>3+/2+</sup> reduction. Moreover, the EXAFS spectra also revealed that the catalyst deactivation was accompanied by a drastic change in the local structure of the first coordination shell of the Fe atom, resulting in a decreased nitrogen coordination number (from 4 to 3) due to the loss of a pyrrolic N. It is worth noting that a partial hydrogenation or carboxylation of porphyrin rings under electrochemical conditions has been reported in several

Fe molecular systems.<sup>72,93</sup> The crucial role of the coordinative environment on the CO<sub>2</sub>RR performance was further demonstrated by the dramatic activity loss and faster deactivation observed for a reference Fe<sup>2+</sup>–N<sub>4</sub> sample containing 4 pyridinic N atoms, synthesized from the [Fe(phen)<sub>3</sub>]<sup>2+</sup> precursor. Importantly, unlike the case of the Fe<sup>3+</sup>–N<sub>4</sub> catalyst, the CO<sub>2</sub>RR reaction at Fe<sup>2+</sup>–N<sub>4</sub> sites was found to be rate-limited by CO desorption at high overpotentials. Taken together, these results show that the Fe<sup>3+</sup>–N<sub>4</sub> (pyrrolic) configuration is able to promote an extremely durable and efficient CO<sub>2</sub>RR to CO: the pyrrolic N atoms stabilize the high Fe<sup>3+</sup> oxidation state, which reduces the  $\pi$ -backdonation to adsorbed CO, resulting in a weaker CO binding. On the other hand, the Fe<sup>2+</sup>–N<sub>4</sub> (pyridinic) sites catalyze CO<sub>2</sub>RR less efficiently due to stronger CO binding on Fe<sup>2+</sup> center stabilized by pyridinic N.<sup>340</sup> Notably, these findings match well with the different catalytic behavior commonly reported for homogeneous Fe catalysts bearing heme and non-heme ligands, suggesting an intimate correlation between some specific local metal-coordinative features in Fe–N–C SACs and the corresponding structurally similar Fe-based homogeneous counterparts. For instance, Fe porphyrin molecular systems, whose structure is reminiscent of the Fe<sup>3+</sup>–N<sub>4</sub> (pyrrolic) sites, are known to be very efficient electrocatalysts for CO<sub>2</sub>RR to CO in organic electrolytes as well as in water, and are not generally affected by severe CO poisoning under CO<sub>2</sub>RR. On the other hand, in analogy with Fe<sup>2+</sup>–N<sub>4</sub> (pyridinic) single sites, the Fe quaterpyridine homogeneous catalyst (63-Fe) suffers



from CO deactivation under pure electrocatalytic conditions with the formation of stable Fe carbonyl species.<sup>281</sup> Such a fascinating comparison between Fe SACs and molecular systems is a clear example that unveiling the relationships between structural features of a molecular ligand framework (*e.g.* rigidity *vs.* flexibility, macrocyclic *vs.* open structures) and the electronic properties of key intermediates involved in CO<sub>2</sub>RR may pave the way for a rational design of both, homogeneous and heterogeneous catalysts.

Another recurrent topic in the available literature on Fe–N–C SACs is the beneficial effect of additional nitrogen doping on the CO<sub>2</sub>RR catalytic performances.<sup>305,343–345</sup> An increase in the level of N doping was first predicted by first-principle calculations to facilitate the \*COOH formation and \*CO desorption steps in Fe–N<sub>4</sub> SACs.<sup>346</sup> In a similar fashion, the presence of additional N atoms near the Fe–N<sub>4</sub> was calculated to exert a synergistic effect which contributes to lower the barrier for the protonation of the bound \*CO<sub>2</sub><sup>–</sup>, resembling the stabilizing effect of pendant amine,<sup>245,257,267</sup> amide<sup>125</sup> or urea<sup>126</sup> groups in the second coordination sphere in molecular catalysis (see Sections 3 and 4).<sup>339</sup> From an experimental perspective, Yang *et al.* studied the effect of the oxidation treatment and found improved CO<sub>2</sub>RR activity resulting from an increased amount of pyrrolic N.<sup>345</sup> In another recent investigation, the annealing of hemin (Fe source) in the presence of an excess of melamine (N-rich additive) and defective graphene led to atomically dispersed Fe–N<sub>5</sub> sites stabilized by pyrrolic N-doped graphene, acting as an additional axial ligand coordinated to Fe–N<sub>4</sub> moieties (Fig. 24a).<sup>344</sup> This unique configuration was found to outperform a Fe–N<sub>4</sub> catalyst in terms of robustness and selectivity to CO (FE 97% at –0.46 V *vs.* RHE, Fig. 24b).



Fig. 24 (a) Scheme of the FeN<sub>4</sub> and FeN<sub>5</sub> catalysts. CO<sub>2</sub>RR catalytic performance of the as-synthesized catalysts. (b) Faradaic efficiency and partial current density for FeN<sub>5</sub>, FeN<sub>4</sub>, and the precursors hemin (H) and melamine with graphene (M–G). Adapted with permission from ref. 344. Copyright 2019, Wiley–VCH.

Theory and the analysis of the local density of states (LDOS) suggested that the additional axial ligand contributes to reduce the electron density from the 3d orbitals of the metal center, alleviating the  $\pi$ -backdonation to coordinating CO and favoring the rapid CO release step. Following a similar concept, Yang and co-workers developed an alternative core–shell strategy to improve the \*CO desorption step in Fe–N–C SACs, based on the encapsulation of Fe nitride nanoparticles (Fe<sub>x</sub>N) with graphene layers containing atomically dispersed Fe–N<sub>4</sub>–C units.<sup>347</sup> Owing to the additional coordination to the N atom of the Fe<sub>x</sub>N core, the surface single-site assumed a Fe–N<sub>5</sub>–C configuration, displaying a much more efficient \*CO desorption step as compared to the bare Fe–N<sub>4</sub>–C configuration. An analogous *trans* effect, based on the influence of a *trans* donor ligand on the CO<sub>2</sub> activation bond, was recently observed for a homogeneous Ru catalyst bearing a 2,2':6',2''-terpyridine and an asymmetric pyridyl-N-heterocyclic carbene (NHC) ligands.<sup>348</sup> A stereochemical control was found to be essential to efficiently catalyze CO<sub>2</sub>RR to CO, since the presence of the strong  $\sigma$ -donating NHC ligand in *trans* to the site for CO<sub>2</sub> bonding significantly boosted the kinetics of the CO dissociation step. Owing to the extreme versatility of this effect, *trans* coordination of a tertiary amine led to a change in the selectivity of the Fe porphyrins towards formate production, contributing to facilitate the protonation of reduced CO<sub>2</sub> as well as the formate release step (*vide supra*).<sup>106</sup> It is worth noting that, as discussed above, a beneficial effect of a pyridine or oxygen donor axial coordination was experimentally observed for electrode-functionalized molecular Co complexes with macrocyclic ligands.<sup>161,192–195</sup> In a Fe–N–C single-site catalyst, the presence of a H<sub>2</sub>O molecule axially adsorbed on Fe–N<sub>4</sub> moieties was found to lower the reaction barrier for the first electron transfer to form \*CO<sub>2</sub><sup>–</sup>.<sup>306</sup> Moreover, in a tetraazamacrocyclic Co molecular complex, the *trans* axial coordination of a solvent CH<sub>3</sub>CN molecule to a five-coordinated Co–CO<sub>2</sub> adduct led to an increase of the observed metal-to-ligand charge transfer (Section 4.1.2).<sup>11,246</sup>

In spite of the numerous studies focusing on the effect of the coordinative environment of the Fe center on the CO<sub>2</sub>RR activity of Fe–N–C catalysts, the number of systematic reports concerning the influence of the reaction conditions (other than the applied potential) on catalysis is relatively scarce. In this regard, Strasser and co-workers investigated the role of the pH and electrolyte on CO<sub>2</sub>RR activity and selectivity of Fe–N–C catalysts, containing Fe–N<sub>x</sub> moieties.<sup>349</sup> Unlike H<sub>2</sub> evolution, which was strongly favored at acidic pH values, the catalytic CO production was found to be independent of the pH on the normal hydrogen electrode (NHE) potential scale. This implies that the CO/H<sub>2</sub> ratio may be fine-tuned by controlling the electrolyte pH, achieving high CO selectivity at high pH values. Moreover, the CO formation rate as a function of the pH on the RHE scale suggested a decoupled electron–proton transfer (DEPT) mechanism for CO production (Fig. 25a), whereby the rate-determining step is the formation of the key (Fe–N–C)–CO<sub>2</sub><sup>–</sup> intermediate, followed by an irreversible protonation step (Fig. 25b). Notably, an analogous mechanism has been





Fig. 25 (a) pH dependence of the CO formation rate at a constant potential on the RHE scale (black,  $-0.5 V_{\text{RHE}}$ ; red,  $-0.65 V_{\text{RHE}}$ ); (b) scheme of the proposed catalytic cycle of the  $\text{CO}_2\text{RR}$  on Fe-N-C catalysts. Adapted with permission from ref. 349. Copyright 2018 American Chemical Society.

described for an immobilized Co protoporphyrin catalyst by Koper and co-workers (see Section 3.2.1), in which the formation of the key  $[\text{Co}(\text{P})(\text{CO}_2)]^-$  adduct occurs after the initial one-electron reduction to form the active  $[\text{Co}^{\text{I}}(\text{P})]^-$  species.<sup>51,154</sup> Analogous reaction pathways have also been proposed for homogeneous macrocyclic catalysts,<sup>215</sup> strongly suggesting that the molecularly defined solid-state Fe-N<sub>x</sub> motifs are the primary active sites in Fe-N-C. These moieties may contribute to stabilize the  $(\text{Fe-N-C})-\text{CO}_2^-$  intermediate giving rise to a solid-state heterogeneous charge-transfer reaction mechanism strikingly similar to that occurring in macrocyclic metal-N<sub>x</sub> molecular catalysts complexes.<sup>349</sup> The  $\text{K}^+$  cations were also proposed to provide an additional stabilization of this intermediate,<sup>349,350</sup> exerting a beneficial effect on catalysis which resembles the synergistic boosting effect observed upon the addition of Lewis acids in several heme<sup>93,94</sup> (see Section 3.1.1) and non-heme<sup>289,351,352</sup> molecular catalysts. However, it is worth noting that the mechanism can be affected by the pH.<sup>353</sup> These results are extremely important since they contribute to unify some fundamental concepts of the fields of heterogeneous and homogeneous catalysis.

An interesting aspect of Fe-N<sub>x</sub> moieties in Fe-N-C SACs relies in their ability to promote the reduction of  $\text{CO}_2$  to beyond 2e products, representing one of the few reported examples of solid-state non-Cu-based electrocatalysts able to produce hydrocarbons. In this perspective, it is supposed that the strong CO binding occurring at the Fe sites plays an important role, and that moderate \*H adsorption may favor further protonation of the adsorbed \*CO to generate >2e products. The rate for  $\text{CH}_4$  production was found to increase at low pH, suggesting that CO protonation is the rate-limiting step. Nevertheless, the concomitant enhancement of HER resulted in low FEs for  $\text{CH}_4$  production (<1%).<sup>349</sup> In agreement with theoretical predictions,<sup>57,301</sup> Fe-N<sub>x</sub> sites of Fe-N-C materials were found to produce small amounts of  $\text{CH}_4$  in addition to the predominant CO. Moreover, *operando* EXAFS data revealed that an unusual change in the Fe oxidation state from  $\text{Fe}^{2+}$  to  $\text{Fe}^{1+}$  is likely involved in the  $\text{CH}_4$  production process.<sup>354</sup> Interestingly, a molecular iron porphyrin system (complex 18, see Chart 1)

was recently shown to catalytically generate  $\text{CH}_4$  from  $\text{CO}_2$  and CO under homogeneous photochemical conditions in the presence of a photosensitizer and a sacrificial electron donor.<sup>355</sup> In this report, CO is a key intermediate in the  $\text{CO}_2$ -to- $\text{CH}_4$  process and the  $\text{Fe}^{\text{III}}$  process is pivotal, *via* the formation of a Fe-formyl intermediate. It is worth noting also that the Fe quaterpyridine complex 63-Fe was used as a molecular precursor for the electrochemical conversion of  $\text{CO}_2$  to  $\text{CH}_4$  (FE *ca.* 2%) in  $\text{CH}_3\text{CN}$  in the presence of TEOA as a proton source.<sup>356</sup> In this case, *in situ* formed Fe particles derived from the electrochemical decomposition of the starting molecular complex are likely the responsible species for  $\text{CH}_4$  production. In a recent integrated experimental-computational study, Ju *et al.* also elucidated the possible pathways for  $\text{CO}_2\text{RR}$  to  $\text{CH}_4$  at the Fe-N<sub>x</sub> sites as well as the role of the possible intermediate products formed during the  $\text{CO}_2$ -to- $\text{CH}_4$  cascades.<sup>357</sup> As a result, CO was found to be the key intermediate toward  $\text{CH}_4$ ,  $\text{CH}_3\text{OH}$  and  $\text{CH}_2\text{O}$  production, yet  $\text{CH}_2\text{O}$  (but not  $\text{CH}_3\text{OH}$ ) could be further reduced to  $\text{CH}_4$ . Moreover, the isolated nature of atomically dispersed Fe-N<sub>x</sub> units was identified as the main origin for low hydrocarbon selectivity, suggesting “dual-site” or “hybrid-tandem” catalysts, featuring cooperative sites for \*CO and \*H adsorption, as viable promising strategies.

### 5.3 Co-N-C catalysts

In contrast to the superior  $\text{CO}_2\text{RR}$  performances displayed by the heterogenized molecular Co phthalocyanine complexes in comparison with derivatives containing other metals,<sup>204</sup> Co-N-C SACs (especially Co-N<sub>4</sub> sites) are typically intrinsically less selective for  $\text{CO}_2\text{RR}$  than their Ni and Fe analogs, resulting in lower faradaic yields for CO production.<sup>297,337</sup> This behavior is generally due to the predominant competitive HER process on Co-N-C catalysts,<sup>316,358</sup> related to unfavorable \*H adsorption energies and higher energetic barriers for \*CO desorption as compared to the Fe and Ni analogues.<sup>306,314,318</sup> Notably, the lower selectivity displayed by atomically dispersed Co-N<sub>4</sub> sites *versus* the Ni counterparts reflects the different reactivity of molecular Ni and Co systems based on tetraazamacrocyclic ligands. As previously discussed in Section 4.1, the molecular  $[\text{Ni}(\text{cyclam})]^{2+}$  catalyst is



able to promote a selective CO<sub>2</sub>-to-CO conversion in aqueous media over a wide pH range, due to the unfavorable protonation of the active Ni<sup>I</sup> species even at very acidic pH under CO<sub>2</sub>-saturated conditions.<sup>214</sup> On the contrary, macrocyclic Co<sup>I</sup> species are generally protonated much easier, forming Co hydride intermediates which favor the competitive HER process over CO<sub>2</sub>RR (see Section 4.1).<sup>11</sup> Furthermore, albeit CO inhibition has been experimentally observed also for the [Ni(cyclam)]<sup>2+</sup> homogeneous system,<sup>217</sup> Co<sup>I</sup> non-heme macrocycles are known to possess a great affinity for CO binding.<sup>11</sup> The *in situ* formation of stable Co carbonyl species, hindering an efficient CO<sub>2</sub>RR, has been reported also for homogeneous Co systems bearing tetradentate aminopyridyl nitrogen ligands (see Section 4.3).<sup>277</sup>

Nevertheless, the catalytic properties of Co–N–C materials towards CO<sub>2</sub>RR have been reported to be extremely dependent on the local coordination environment of the Co centers, with promising results obtained for alternative configurations respect to the conventional Co–N<sub>4</sub> sites. A common strategy to control the nitrogen coordination number of single Co atoms consists in the variation of the pyrolysis temperature, since increasing annealing temperatures tend to favor a progressive disruption of the Co–N bonds. Following this approach, the CO<sub>2</sub> electroreduction behavior of a series of Co–N–C SACs containing Co–N<sub>2</sub>, Co–N<sub>3</sub> and Co–N<sub>4</sub> moieties, respectively, was systematically investigated (Fig. 26a–c).<sup>359</sup> As a general trend, the selectivity towards CO production was found to increase upon progressively decreasing the Co–N coordination number from 4 to 2, with Co–N<sub>2</sub> showing the highest value for maximum FE<sub>CO</sub> (95% at –0.68 V vs. RHE, Fig. 26d and e). In agreement with these results, the Co–N<sub>2</sub> configuration showed the lowest charge-transfer resistance from the catalyst to the CO<sub>2</sub> molecule, thereby favoring the activation of the latter to form CO<sub>2</sub><sup>•–</sup>. Interestingly, first-principles calculations suggest that a strong \*CO binding occurs at the Co–N<sub>2</sub>

moieties. It was proposed that the coordination of a second CO molecule on the unsaturated Co site would help to promote the \*CO desorption step.<sup>359</sup>

Nonetheless, an opposite trend was reported for some Co–N–C catalysts, suggesting that an increase in the N coordination number is beneficial for CO<sub>2</sub>RR. For example, atomically dispersed Co–N<sub>5</sub> sites embedded into polymer-derived hollow N-doped porous carbon spheres exhibited remarkable CO<sub>2</sub>RR activity and stability, reaching a FE<sub>CO</sub> 99% at –0.79 V vs. RHE.<sup>360</sup> *In situ* XAS measurements further confirmed the catalytic relevance of the Co–N<sub>5</sub> units during CO<sub>2</sub> electroreduction. Under similar conditions, the molecular CoPc metal precursor, containing well-defined planar Co–N<sub>4</sub> moieties, resulted in lower efficiencies and current densities for CO production. In an attempt to decrease the Co–N coordination number in the original Co–N<sub>5</sub> sample, the latter was pyrolyzed at increasingly higher temperatures, leading to a progressive drop in the observed FE<sub>CO</sub>, partly due to formation of inactive Co NPs. The unique Co–N<sub>5</sub> configuration was predicted to favor the \*COOH formation and the \*CO desorption steps.<sup>361</sup> As mentioned above, analogous positive effects on catalysis due to the presence of axial nitrogen donors were found for Co molecular systems with heme macrocyclic ligands<sup>192,194</sup> and in Fe–N–C SACs.<sup>344,347</sup> In another study, a Co–N–C SAC containing isolated Co–N<sub>4</sub> moieties provided a considerably improved selectivity for CO<sub>2</sub>-to-CO conversion in comparison with a Co–N<sub>4–x</sub>–C<sub>x</sub> derivative accommodating Co sites with lower Co–N coordination number (FEs 82% vs. 47% at –0.8 V vs. RHE for Co–N<sub>4</sub> and Co–N<sub>4–x</sub>–C<sub>x</sub>, respectively).<sup>362</sup>

#### 5.4 Other transition metals (Zn, Cu, Mn, Sn, Bi)

Albeit less studied than the Ni, Fe and Co analogs, a few single-atom M–N–C materials containing transition metals such as Zn, Cu, Mn, Sn or Bi, have been employed as efficient catalysts



Fig. 26 (a) Schemes of Co–N<sub>4</sub> and Co–N<sub>2</sub>. (b) XANES (c) EXAFS spectra suggesting the atomic dispersion of Co atoms in Co–N<sub>2</sub>, Co–N<sub>3</sub>, and Co–N<sub>4</sub>, and the lowest N coordination number in Co–N<sub>2</sub>. (d) LSV of Co–N<sub>2</sub>, Co–N<sub>3</sub>, Co–N<sub>4</sub>, and Co NPs and pure carbon paper as background. (e) CO faradaic efficiencies at different applied potentials. Adapted with permission from ref. 359. Copyright 2018, Wiley-VCH.



for CO<sub>2</sub>RR. Among them, the Mn–N–C systems have attracted growing interest due to the earth-abundant character of Mn, but also to the promising results shown by molecular Mn complexes bearing polypyridyl ligands.<sup>42,363–365</sup> Mn–N–C catalysts were first reported in comparative studies on a series of M–N<sub>x</sub>–C catalysts containing different transition metals, showing limited catalytic performances for the Mn–N–C materials as compared with the Ni and Fe counterparts.<sup>366,367</sup> However, high-performance for CO<sub>2</sub>RR was subsequently reported for atomically dispersed Mn sites on an N-doped carbon matrix with a halogen and nitrogen dual-coordination, namely (X, N)–Mn/G (X = Cl, Br, I).<sup>368</sup> More specifically, the (Cl, N)–Mn/G catalysts exhibited an excellent selectivity to CO with a maximum FE of 97% at –0.6 V vs. RHE, representing one of the best-performing heterogeneous catalysts reported so far for CO<sub>2</sub>RR. X-ray absorption spectroscopy analysis of (Cl, N)–Mn/G revealed a unique out-of-plane distorted Mn–N<sub>4</sub>Cl configuration for the active site, in which the low-valent Mn center (<2+) is coordinated to four N atoms and to one axial Cl atom. Under CO<sub>2</sub>-saturated atmosphere, *in situ* XAS spectra showed a higher energy shift for the Mn K-edge of (Cl, N)–Mn/G, consistent with an increased oxidation state of the Mn centers due to charge transfer from the low-valent Mn to the 2p orbitals of CO<sub>2</sub> to generate adsorbed \*CO<sub>2</sub><sup>δ-</sup>. As mentioned above for the *operando* XAS data on a Ni–N–C catalyst,<sup>313</sup> during CO<sub>2</sub>RR at –0.6 V vs. RHE, the Mn K-edge shifted back to lower energy. Notably, only little changes were observed for the Cl-free N–Mn/G sample, suggesting that the halogen atom plays a crucial role in the CO<sub>2</sub> activation process. The computational data shed light on the crucial role played by the axial Cl coordination in the catalytic reaction. First, it was predicted to promote a distortion of the Mn site structure in agreement with the experimental results, facilitating the adsorption of CO<sub>2</sub> and \*COOH formation. Moreover, it displayed a stabilizing electronic effect on the \*COOH intermediate increasing the electron density at the Mn–C bond, as well as facilitating the \*CO desorption step. As previously discussed, analogous effects have been observed for several molecular systems<sup>192,194</sup> and atomically dispersed M–N<sub>x</sub> active sites<sup>344,347,361</sup> coordinated to axial nitrogen donors.

Copper is another interesting metal for heterogeneous CO<sub>2</sub>RR catalysis, widely studied for its unique ability to produce C<sub>2</sub>/C<sub>3</sub> chemicals.<sup>39,369,370</sup> However, in contrast with bulk heterogeneous Cu-based materials, Cu–N–C single-atom catalysts have been predicted to be quite unstable under electrochemical conditions. In particular, DFT calculations have shown low thermodynamic stability of the Cu–N<sub>x</sub> sites under strongly reducing conditions (<–0.7 V vs. RHE) resulting in spontaneous decomposition of the N-coordinated Cu ions into metallic Cu NPs.<sup>367</sup> Furthermore, the d-orbital of the Cu atom is filled with 9 (one singly occupied orbital) or 10 (fully occupied) electrons, indicating that the covalent bonds between copper and nitrogen are quite unlikely.<sup>57,302</sup> In spite of these considerations, unsaturated Cu–N<sub>2</sub> coordinated moieties anchored into a graphene matrix (Cu–N<sub>2</sub>/GN) have been recently reported to efficiently convert CO<sub>2</sub> to CO with FE<sub>CO</sub> 81% at –0.5 V vs. RHE.<sup>371</sup>

The high selectivity was attributed to the unsaturated environment of copper, as suggested by a relatively low calculated potential barrier between CO<sub>2</sub> and the Cu–N<sub>2</sub> moieties. However, the structural changes of the active sites occurring during the catalytic reaction remain unclear.

Zn has been studied in bulk materials for CO production but with limited performance and unclear underlying reaction mechanism.<sup>372</sup> In contrast, some Zn–N–C materials prepared by different synthetic methods have been reported as highly selective catalysts towards CO production.<sup>373,374</sup> From XPS and EXAFS analysis, the active site was suggested to involve Zn–N<sub>x</sub> moieties, with pyridinic N atoms as possible Zn-coordination sites.<sup>374</sup> The presence of Zn–N<sub>4</sub> moieties as active sites was further corroborated by experimental and DFT results, showing a lower free energy barrier for the rate-limiting formation of \*COOH than the comparing Zn–C<sub>4</sub> and N<sub>4</sub>/C structures.<sup>373</sup> Lastly, a few examples of SACs based on Sn and Bi have been reported. In particular, atomically dispersed Sn in N-doped catalysts were found to switch their selectivity at low overpotentials from HCOO<sup>–</sup> to CO with a FE of 91% at –0.6 V vs. RHE.<sup>375</sup> Another interesting study revealed an excellent CO selectivity for Bi–N<sub>4</sub> sites on carbon networks, reaching a FE<sub>CO</sub> of 97% at –0.5 V vs. RHE.<sup>376</sup>

## 6. Metal nanoparticles for CO<sub>2</sub>RR

In order to develop heterogeneous metal catalysts for highly efficient and selective CO<sub>2</sub>RR, a rational design of the catalytic surface is required to control the stability of surface-bound intermediate species. In this scenario, by controlling the morphological, electronic, and surface chemical properties of metal nanoparticles (NPs) (or nanoclusters (NCs)), it is possible to understand the key factors influencing the performance of nanostructured CO<sub>2</sub>RR catalysts.<sup>369,377–383</sup> For example, the size and shape of NPs can be used to control the number of low-coordinated sites and the ratio between the different crystal facets on the surface, which can affect the binding strength of the reaction intermediates (Section 6.1). In addition to structural effects related to the metal NP itself, the interaction between the NP surface and either the support material or small surface-bonded molecular stabilizers may play a role in determining the adsorption properties and electron transfer kinetics of the catalysts, thus influencing the stability of the intermediates involved in the catalytic reaction. These effects will be discussed in the Sections 6.2 and 6.3, respectively.

### 6.1 Size and shape effects

A systematic investigation of the metal NP size-dependence of CO<sub>2</sub>RR was carried out for Au NPs. Sun *et al.*<sup>384</sup> explored the electrocatalytic CO<sub>2</sub>RR behavior of monodispersed Au NPs with various sizes (4, 6, 8 and 10 nm, respectively), showing that the selectivity of CO<sub>2</sub>RR to CO tends to decrease with decreasing NP size. To account for this effect, DFT was used to calculate the free energies of reaction steps for CO and H<sub>2</sub> production on certain crystal sites (*i.e.* Au(111), Au(211) and a 13-atom Au cluster)





**Fig. 27** Size-dependent effects in CO<sub>2</sub>RR for (a–c) Au, (d) Zn, (e) Sn, and (f) Cu NPs. (a) Catalytic site density on closed-shell cuboctahedra Au clusters as a function of the particle diameter. Reproduced with permission from ref. 384. Copyright 2013 American Chemical Society. (b) CO<sub>2</sub>RR current densities at –1.2 V vs. RHE as a function of the Au NP size. (c) Molar ratio of H<sub>2</sub> and CO produced at –1.2 V vs. RHE as a function of the Au NP size. Panels b and c reproduced with permission from ref. 385. Copyright 2014 American Chemical Society. (d) Faradaic selectivity toward CO measured as a function of the Zn NP size at –1.1 V vs. RHE. The inset displays an AFM image and *operando* EXAFS data of 6.8 nm Zn NPs. Reproduced with permission from ref. 389. Copyright 2018 American Chemical Society. (e) *Operando* Raman spectra tracking the surface oxidation state of Sn NPs as a function of the potential. Reproduced with permission from ref. 390. Copyright 2015 American Chemical Society. (f) Faradaic selectivity toward H<sub>2</sub>, CO, CH<sub>4</sub> and C<sub>2</sub>H<sub>4</sub> measured at –1.1 V vs. RHE as a function of Cu NP size. Reproduced with permission from ref. 391. Copyright 2014 American Chemical Society.

present on the NPs surface (Fig. 27a). The results revealed that catalytic CO evolution preferentially occurs at the Au(211) sites (denoted as “edge sites”), while Au(111) and 13-atom Au clusters (denoted as “corner sites”) are more active sites for H<sub>2</sub> production. Hence, the increase in the H<sub>2</sub> selectivity observed with decreasing NP size was ascribed to an increased content of corner sites on the NP surface. Analogous results were also obtained for micellar Au NPs within the size range of 1–8 nm.<sup>385</sup> Specifically, small Au NPs (1.1 nm in size) displayed an activity that is more than two orders of magnitude higher than larger Au NPs (7.7 nm in size) (Fig. 27b). However, the higher activity was mainly associated to HER rather than CO production (Fig. 27c), consistent with the weaker binding of the COOH\* intermediates and the presence of large H\* coverages on the small Au NPs.

In addition to Au NPs, various other metal NPs such as Bi,<sup>386</sup> Sn,<sup>387</sup> Ag,<sup>388</sup> and Zn<sup>389</sup> have shown a similar structural effect on CO<sub>2</sub>RR, displaying a significant drop of CO<sub>2</sub>RR efficiency below a certain NP size. However, depending on the specific metal NPs, a variety of different sizes showed the optimal catalytic performances for CO<sub>2</sub> reduction to CO (or formate for Sn NPs). For instance, size-controlled Zn NPs ranging from 3 to 5 nm exhibited high CO<sub>2</sub>RR activity and selectivity to CO (FE ~ 70%), whereas a drastic increase of H<sub>2</sub> evolution was observed for NPs smaller than 3 nm, presumably due to a larger content of low-coordinated sites.<sup>389</sup> In a similar fashion, the maximum FE for CO<sub>2</sub> conversion to formate on Sn NPs was achieved for ~5 nm NPs, representing a balance between surface stabilization of the CO<sub>2</sub>\*<sup>–</sup> intermediate and its activation *via* further

protonation/reduction steps.<sup>387</sup> As indicated by *operando* spectroscopic studies (XAS, Raman), oxidized/hydroxylated species were found to be stable during CO<sub>2</sub>RR for pre-oxidized Zn and Sn NPs. These cationic species are likely involved in the catalytic reaction and may lead to differences in the adsorption strength of the reaction intermediates (Fig. 27d and e).<sup>389,390</sup> Moreover, it is worth noting that other factors related to the preparation method of the NPs (presence of surface-anchored organic agents, surface oxidation degree, defects, *etc.*) or the reaction conditions were found to have a strong influence of the CO<sub>2</sub>RR activity, contributing to alter the electronic structure and the physicochemical properties of the metal NPs (see next paragraph). A representative example is given by mono-dispersed Bi NPs with average sizes of 36 nm and 7 nm, whose catalytic properties for CO<sub>2</sub>RR to CO were explored in non-aqueous 1-butyl-3-methylimidazolium trifluoromethane-sulfonate ([bmim][OTf])/CH<sub>3</sub>CN electrolyte.<sup>386</sup> After a hydrazine-based surface activation treatment, the Bi NPs showed an excellent catalytic activity, reaching a FE<sub>CO</sub> ~ 96% for the 36 nm NPs. Furthermore, a negligible size or morphology effect was observed on CO<sub>2</sub>RR efficiency in these conditions, likely due to a change of the CO<sub>2</sub>RR mechanism in aprotic media, which occurs *via* a direct H<sup>+</sup> transfer between the adsorbed CO<sub>2</sub> molecule and the electrolyte rather than *via* pre-adsorbed protons on the catalyst surface.<sup>386</sup> On the other hand, the Bi NPs displayed a size-dependent behaviour after air exposure, resulting in a decreased efficiency for CO production with smaller NPs. These results suggest that the reduction of surface



metal oxides to the metallic state is dependent on the size and morphology of the particle, being much faster for larger NPs.

In the case of Cu NPs,<sup>391</sup> an increased population of low-coordinated sites also results in a preferred H<sub>2</sub> production. However, for large Cu NPs and due to the unique multi-electron CO<sub>2</sub>RR properties of Cu, the product distribution is mainly based on the formation of hydrocarbons rather than CO (or formate) (Fig. 27f).<sup>391</sup> While the adsorbed \*CO and \*COOH on the NP surface are considered as the key intermediates to form CO (or formate), Cu NPs possess the ability to further protonate \*CO to form \*HCO or \*COH species, due to the fact that \*CO is not easily desorbed from the Cu NPs.<sup>392–394</sup> Thus, the studies on Cu catalysts have been focused on producing higher yields of hydrocarbons by exploring the way to efficiently stabilize \*HCO or \*COH intermediates. Indeed, the inherent selectivity of Cu has been considered as one of the main research topics of CO<sub>2</sub>RR, and many reviews and research articles are available.<sup>40,380,395–401</sup> Further investigation of nanostructured Cu catalysts for CO<sub>2</sub>RR is outside of the scope of the present work.

In contrast with the reports mentioned above, an opposite trend for size-dependent CO<sub>2</sub>RR has been observed for a series of Pd NPs<sup>402</sup> ranging from ~2 to 10 nm. The efficiency and selectivity towards CO production was found to increase upon decreasing the NP size, leading to faradaic efficiencies between

5.8% (10.3 nm NPs) and 91.2% (3.7 nm NPs) at –0.89 V vs. RHE. In order to explain the experimental results, computational data highlighted that CO<sub>2</sub> reduction is considerably favored at the corner and edge sites in comparison with the terrace sites, whereas the H<sub>2</sub> evolution process is similar over all the three types of sites.

In addition to the size-dependence, shape modifications of NPs can also influence their CO<sub>2</sub>RR catalytic performance by controlling the preferential exposure of specific surface sites. In an attempt to design a catalyst with more exposed edges on the surface (Fig. 28a),<sup>403</sup> Au nanowires (2 nm wide and 500 nm in length) were synthesized and found to display very low onset potentials (–0.2 V vs. RHE) and high FE for CO production (94%) (Fig. 28b). DFT calculations suggested that the high density of edge sites in the Au nanowires stabilizes the \*COOH intermediate and facilitates the \*CO release step. The catalytic performance for CO<sub>2</sub>RR has also been shown to be strongly dependent on the crystal facet located on the NP surface. For instance, triangular Ag nanoplates showed selective CO formation with a FE of 96.8% at –0.86 V vs. RHE,<sup>404</sup> outperforming the spherical NPs with similar size as well as the bulk metallic Ag surface. These results were interpreted with the aid of theoretical data in terms of an optimum edge-to-corner ratio and predominant Ag(100) facets in the nanoplates

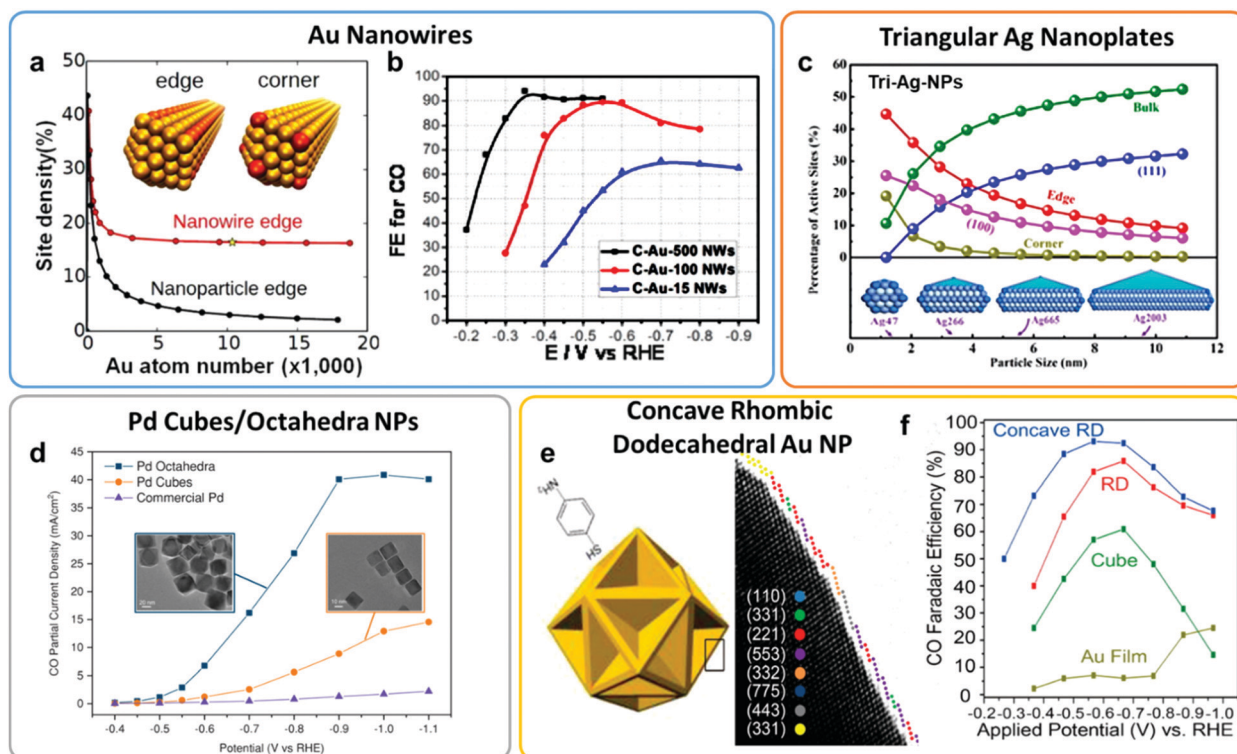


**Fig. 28** Shape-effect on CO<sub>2</sub>RR: (a and b) Au nanowires, (c) triangular Ag nanoplates, (d) Pd cubes and octahedra NPs, and (e and f) concave rhombic dodecahedral Au NP. (a) Edge site weight percentage for a 2 nm wide Au NW and an Au NP as a function of the number of Au atoms. (b) CO FE of 500, 100, and 15 nm-long Au nanowires. Panels a and b reproduced with permission from ref. 403. Copyright 2014 American Chemical Society. (c) Active adsorption site density on triangular Ag nanoplates as a function of the NP size. Reproduced with permission from ref. 404. Copyright 2017 American Chemical Society. (d) CO partial current density of Pd cubes and octahedra NPs and their TEM images. Reproduced with permission from ref. 405. Copyright 2019 Wiley-VCH. (e) Schematic illustration and atomic structures of a concave rhombic dodecahedron Au NP. (f) CO FE of Au film, Au cube, Au RD, and Au concave RD as a function of applied potential. Panels e and f reproduced with permission from ref. 406. Copyright 2015 American Chemical Society.



(Fig. 28c). Shape engineering was also successfully adopted by Chen and co-workers<sup>405</sup> to increase the catalytic CO<sub>2</sub>RR-to-CO activity and stability of Pd NPs. In this study, Pd octahedra dominated by (111) facets showed higher CO selectivity (FE up to 95%) and improved activity compared to Pd cubes with (100) facets (Fig. 28d). Interestingly, *in situ* XAS revealed that regardless of the original facet, a Pd hydride species (PdH) is formed under reaction conditions. Based on DFT calculations, the PdH(111) species was proposed as the active site, being able to promote CO desorption.

Lastly, nanoparticles enclosed by high-index facets have been experimentally reported to further inhibit H<sub>2</sub> production during CO<sub>2</sub>RR. As an example, concave rhombic dodecahedron (RD) Au NPs with various high-index surfaces<sup>406</sup> including (331), (221) and (553) were found to exhibit an onset potential for CO<sub>2</sub>RR to CO at  $-0.23$  V vs. RHE, 200 mV positively shifted relative to that of an Au film. A FE<sub>CO</sub>  $\sim 70\%$  was observed at  $-0.37$  V vs. RHE, which is approximately three times higher than that of Au NPs exposing low-index facets (Au nanocubes) (Fig. 28e and f).

## 6.2 Support effect

Since the electrochemical CO<sub>2</sub> reduction process over heterogeneous catalysts takes place at a solid/liquid interface, a control over the charge transfer between the catalyst and the surface intermediate species is critical to enhance the efficiency of the process. In this sense, the selection of a suitable support material is essential to ensure fast CO<sub>2</sub>RR reaction kinetics and to adjust the binding strength of intermediates species. For example, the CO production over Ag NPs deposited on carbon

black can be doubled by using a TiO<sub>2</sub> support.<sup>407</sup> Based on the analysis of the CV curves, the TiO<sub>2</sub> support was found to stabilize the reaction intermediates through the involvement of Ti<sup>IV/III</sup> redox couples, also acting as a redox carrier to improve the CO<sub>2</sub> reduction kinetics (Fig. 29a). Recently, Au NPs on a C<sub>3</sub>N<sub>4</sub> support were also reported to exhibit a better performance than carbon-supported Au NPs.<sup>408</sup> The strong interaction between the Au NPs and the C<sub>3</sub>N<sub>4</sub> support was predicted to induce the formation of a negatively charged Au surface, which could stabilize the key \*COOH intermediate. Along this line, the effect of the C<sub>3</sub>N<sub>4</sub> support can be further improved by incorporating carbon quantum dots (CDots), as demonstrated by the enhanced performances shown by the ternary Au NPs-CDots-C<sub>3</sub>N<sub>4</sub> configuration<sup>409</sup> (Fig. 29b). In the latter case, DFT calculations revealed that the combination of CDots with C<sub>3</sub>N<sub>4</sub> results in an enhanced conductivity and CO<sub>2</sub>/H<sub>2</sub> adsorption, facilitating the CO<sub>2</sub> reduction to CO. A number of other carbon- or metal oxide-based materials displayed beneficial effect on CO<sub>2</sub>RR when used as supports in combination with Au NPs. Among them, graphene nanoribbons (GNR) decorated with Au NPs improved the performances of Au NPs supported on carbon black (Fig. 29c),<sup>410</sup> likely due to the strong d- $\pi$  interaction that can serve to modulate the electronic structure of the Au NP, leading to the acceleration of the charge transfer from the CNR to the Au NPs. Interestingly, it is worth noting that similar results were observed for the non-covalent functionalization of molecular catalytic systems based on  $\pi$ - $\pi$  stacking and electrostatic interactions.<sup>138</sup> In fact, the strategy of adjusting the electronic structure of the active catalysts to improve the CO<sub>2</sub>RR performance can be widely applied from molecular to

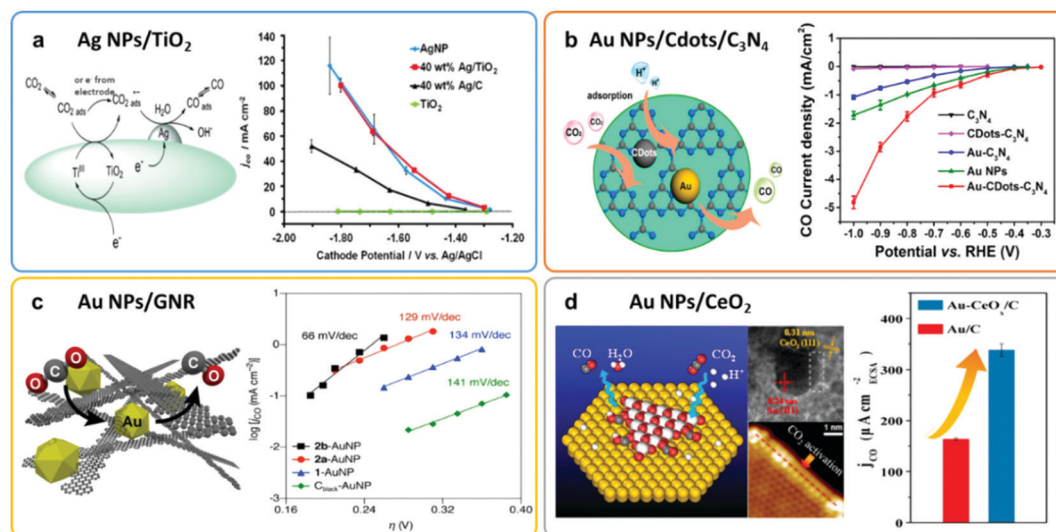


**Fig. 29** Studies on the support effect on (a) Ag NPs/TiO<sub>2</sub>, (b) Au NPs/Cdots/C<sub>3</sub>N<sub>4</sub>, (c) Au NPs/GNR, and (d) Au NPs/CeO<sub>2</sub>. (a) Schematic illustration of the CO<sub>2</sub>RR reaction mechanism to CO on Ag/TiO<sub>2</sub>. Partial current density for CO production as a function of the cathode potential with Ag/TiO<sub>2</sub>, Ag/C, Ag NP, and TiO<sub>2</sub>. Reproduced with permission from ref. 407. Copyright 2014 Wiley-VCH. (b) Schematic illustration of carbon dots (CDots) and Au NPs on C<sub>3</sub>N<sub>4</sub> (Au-CDots-C<sub>3</sub>N<sub>4</sub>) for CO<sub>2</sub>RR. Partial current density for CO production as a function of the applied potential, catalyzed by C<sub>3</sub>N<sub>4</sub> CDots-C<sub>3</sub>N<sub>4</sub>, Au-C<sub>3</sub>N<sub>4</sub>, Au NPs, and Au-CDots-C<sub>3</sub>N<sub>4</sub>. Reproduced with permission from ref. 409. Copyright 2018 American Chemical Society. (c) Schematic illustration of Au NPs embedded in GNR. Tafel slopes for CO activity by GNR- and carbon black-AuNP composite materials. Reproduced with permission from ref. 410. Copyright 2017 American Chemical Society. (d) Schematic illustration of Au NPs supported on CeO<sub>x</sub> for CO<sub>2</sub>RR. Partial current density for CO with Au-CeO<sub>x</sub>/C and Au/C catalysts. Reproduced with permission from ref. 411. Copyright 2017 American Chemical Society.



nanostructured catalysts. Furthermore, an Au NPs/CeO<sub>x</sub> assembly led to a substantial improvement in the efficiency towards CO production in comparison with the single bare components<sup>411</sup> (Fig. 29d). As suggested by *in situ* scanning tunneling microscopy and photoemission spectroscopy, the enhanced reactivity towards CO<sub>2</sub>RR stems from the stabilizing interaction of hydroxyl groups on ceria terraces with key intermediates involved in the catalytic reaction.

The encapsulation of Ag NCs into a reticular MOF structure also revealed to be an effective strategy to enhance the stability and selectivity towards CO<sub>2</sub>RR.<sup>412</sup> This was assigned to the interaction of the catalyst with the porous MOF which favors the electron and mass transfer during CO<sub>2</sub>RR over HER.<sup>412</sup> In particular, the intimate interfacial contact between the Ag NCs and the MOF, brought about by the removal of the native ligands before the encapsulation, was rationalized to be crucial for the improved selectivity toward CO<sub>2</sub>RR.

### 6.3 Surface functionalization with organic molecules

A promising complementary strategy to particle size, shape, composition and support design consists in capping metal NPs with chelating organic molecules.<sup>413–415</sup> This alternative approach applies the concepts and tools of conventional coordination chemistry to design novel metal nanocatalysts with improved catalytic properties. In comparison with the traditional strategies to control the structure of metallic NPs, this approach offers a number of additional advantages: (i) the organic capping agents usually act as NPs stabilizers, preventing or minimizing aggregation phenomena and NP oxidation upon air exposure; (ii) the catalytic properties of metal NPs can be tailored by modifying the electronic and structural features of the organic anchoring agent; (iii) tuning of the local environment around the nanocatalyst surface (*e.g.* increased hydrophobicity, activation of second coordination shell interactions, *etc.*) in order to alter the product distribution of CO<sub>2</sub>RR. A variety of synthetic methods and organic molecules (surfactants, organic ligands based on C, N, P, S or O atoms) have been adopted to functionalize metal NPs.<sup>416</sup> Thiols, amines and NHC ligands represent the main families of organic ligands used to stabilize monometallic NPs for CO<sub>2</sub>RR, and the main advances for each class are discussed in the next paragraphs. NPs or NCs based on late transition metals, such as Au, Ag and Pd, cover the overwhelming majority of the reported organic-stabilized nanocatalysts for CO<sub>2</sub>RR, generally producing CO as the major product. A few specific studies on functionalized flat bulk metallic catalysts will be also discussed in the text, since they provide complementary information for the understanding of the role of the organic ligand on the CO<sub>2</sub>RR activity and selectivity of metallic heterogeneous catalysts. In general, nanomaterials showed enhanced activity compared to polycrystalline surfaces due to their improved reactivity, conductivity and stability under electrochemical conditions.<sup>414</sup>

**6.3.1 Thiols.** Due to their strong binding affinity for metals, thiolate ligands have been widely employed as stabilizing agents for metal nanostructures, especially on Ag and Au. Ligand-protected inherently-charged Au<sub>25</sub>(SC<sub>2</sub>H<sub>4</sub>Ph)<sub>18</sub><sup>−</sup> nanoclusters were



Fig. 30 Schematic illustration of ligand protected Au<sub>25</sub> nanoclusters. LSV and CO formation rate for the various Au catalysts. Reproduced with permission from ref. 417. Copyright 2012 American Chemical Society.

reported to catalyze CO<sub>2</sub> conversion to CO at low overpotentials and higher efficiency as compared to larger NPs and bulk Au catalysts (Fig. 30).<sup>417</sup> The Au–S coordination motifs in the cluster shell were proposed to play a key role in promoting CO<sub>2</sub> adsorption on the NCs. In an effort to rationalize the origin of the observed catalytic activity for CO<sub>2</sub>RR, a follow-up computational study on a series of Au<sub>25</sub>(SR)<sub>18</sub><sup>q</sup> NCs with different charge states ( $q = 0, \pm 1$ ) suggested that, regardless of the initial charge state, CO<sub>2</sub>RR was thermodynamically feasible only upon removal of a ligand (–SR or –R), which occurred under applied bias.<sup>418</sup> In particular, the removal of an –R ligand from the negatively charged NC gave rise to a selective catalyst for CO<sub>2</sub>RR to CO over HER, highlighting the crucial role of the exposed Au and S sites (in particular the latter) in stabilizing the \*COOH intermediate over \*H. The electrochemical stability of the protective organic ligands is a crucial aspect to consider and computational tools are generally extremely important to identify the catalytic sites in ultras-small systems.

The use of cysteamine as anchoring agent has revealed to be beneficial for the CO<sub>2</sub>RR performances of Au NPs and Ag NPs.<sup>388,419,420</sup> For an optimal particle size of 5 nm, Ag NPs on carbon decorated with cysteamine molecules showed a considerably lower overpotential and a 4-fold enhanced CO faradaic efficiency at –0.75 V vs. RHE compared to a polycrystalline Ag foil.<sup>388</sup> While Tafel slope analysis suggested the formation of the \*CO<sub>2</sub><sup>−</sup> adduct to be rate-limiting, DFT calculations highlighted an electronic effect on the Ag surface induced by the Ag–S interaction, which is reminiscent of the through-structure substituent effects observed in molecular catalysts (see Section 3). More specifically, the presence of cysteamine capping agents was predicted to increase the spatial localization of the unpaired electron at the Ag surface, contributing to stabilize the key \*COOH intermediate. Interestingly, the cysteamine molecules had only a small impact on the CO binding energy to the surface, resulting in an overall enhanced catalytic activity.<sup>388</sup>

A follow-up experimental–computational study extended the mechanistic understanding of the cysteamine–Ag NPs system at



a molecular level, proposing that the enhanced activity and selectivity may arise from a synergistic contribution of the electronic effect promoted by the Ag–S interaction and the role of the pendant NH<sub>2</sub> group of anchoring cysteamine molecules, which would assist the CO<sub>2</sub> chemisorption process on the Ag surface.<sup>419</sup> In particular, *ab initio* molecular dynamics (AIMD) simulations suggested that the terminal amine group of the surface ligand may contribute to stabilize the chemisorbed CO<sub>2</sub> molecule by H-bonding interaction (in cooperation with a water molecule, Fig. 31a), exerting an outer coordination sphere effect analogous to that shown by macrocyclic N4 molecular catalysts with pendant amine groups (see Sections 4.1–4.2). In agreement with this interpretation, the length of the alkyl chain of the anchoring ligand was found to be critical for the catalytic performances: Ag NPs functionalized with the 11-amino-1-undecanethiol (C<sub>11</sub>-Ag) did not display an analogous enhancement effect shown by the cysteamine-capped Ag NPs (C<sub>2</sub>-Ag) (Fig. 31b).<sup>419</sup> In this case, the excessive length of the alkyl chain led to an unfavorable geometry which was not suitable to stabilize the surface-bound CO<sub>2</sub> intermediate, being the terminal NH<sub>2</sub> group too far away from the Ag surface. Moreover, unlike for C<sub>11</sub>-Ag, a shift of the N–H band to lower energy was observed by *in situ* ATR-IR spectroscopy for C<sub>2</sub>-Ag, suggesting the involvement of the NH<sub>2</sub> group in the CO<sub>2</sub> chemisorption event.<sup>419</sup>

An analogous boosting effect due to cysteamine capping agents was also recently reported for Au NPs, showing an exclusive CO selectivity at low overpotential and a 110-fold enhanced mass activity in comparison with the naked Au NPs.<sup>420</sup> XAS spectroscopy confirmed the effect of the Au–S interactions on altering the electronic structure of the gold

surface and EXAFS analysis confirmed a lower Au–Au coordination number for cysteamine-Au NPs in comparison with the ligand-free Au NPs. Furthermore, the replacement of cysteamine with 1-propanethiol as a capping agent (terminal CH<sub>3</sub> group) resulted in a significant drop of the CO<sub>2</sub>RR catalytic activity, thereby probing the critical role played by the NH<sub>2</sub> group of the former.<sup>420</sup> Notably, outer coordination sphere effect on CO<sub>2</sub>RR activity and selectivity has been also observed on polycrystalline Au foil functionalized with thio-tethered ligands.<sup>421</sup> Depending on the pK<sub>a</sub> of the terminal group of the thiolate ligand, the activity and faradaic efficiency toward CO, H<sub>2</sub> and HCOO<sup>−</sup> could be tuned. In particular, cysteamine-modified Au electrodes exhibited a 2-fold increase in CO and H<sub>2</sub> production respect to the bare Au foil, whereas the functionalization with 2-mercaptopropionic acid led to exclusive H<sub>2</sub> evolution. Conversely, Au electrodes modified with 4-pyridylethylmercaptan (pK<sub>a</sub> = 5.2) showed a significantly higher production and FE for HCOO<sup>−</sup> as compared to the naked Au foil, owing to the role of the terminal pyridine/pyridinium groups. The latter were proposed to be involved in a proton-induced desorption mechanism leading to HCOO<sup>−</sup> formation.<sup>421</sup> It is interesting to note that in Section 3 we have discussed several examples from molecular catalysis in which pendant pyridine/pyridinium groups in the second coordination sphere exerted a boosting effect for the catalytic CO<sub>2</sub>RR to CO.<sup>168,192,194</sup> Moreover, a selectivity change induced by different groups in the second coordination sphere has been also observed in a number of homogeneous molecular catalysts.<sup>267–271</sup>

Surfactant molecules containing highly hydrophobic long alkyl chains are commonly used as stabilizing agents during metal NPs synthesis. In some cases however, they may partially block the surface active sites limiting the catalyst performance<sup>386</sup> or be easily detached from the surface during prolonged electrolysis. In order to overcome this limitation, the surfactant molecules bound to Au NPs were replaced by chelating porphyrin-like tetradentate ligands with S-terminal anchoring groups.<sup>422</sup> The latter act as hollow scaffolds on Au NPs, interacting with the metal catalyst but without hindering the accessibility of the catalytic sites. This structural modification led to a 110-fold current enhancement in comparison with the parent oleylamine-coated Au NPs, efficiently producing CO (FE up to 93%) at an overpotential of 340 mV (Fig. 32). Importantly, the chelation effect resulted in a remarkable stability, leading to only minor deactivation after 72 h electrolysis. Unlike the classical surfactant-based strategy, this alternative approach ensures a higher number of exposed sites, substantially increasing the current densities. In addition, the tetra-functionalized Au NPs were predicted to be intrinsically more active towards CO<sub>2</sub>RR with respect to both, bare Au(111) and oleylamine-coated Au NPs, showing an energetically more favorable \*COOH formation. The electronic effect due to Au–S interactions was estimated to be negligible.<sup>422</sup> In an earlier study, the same authors used tetrapodal S-terminal porphyrin platforms to functionalize polycrystalline Cu electrodes for electrochemical CO reduction (CORR).<sup>423</sup> Based on DFT calculations, the different selectivity toward oxygenates production experimentally observed for various



Fig. 31 (a) Chemisorbed CO<sub>2</sub> on cysteamine-functionalized (left) and on cysteamine-free (right) Ag(111) surface. Only the water molecules directly forming hydrogen bond (slashed line) are shown. The colors are: Ag in silver, C in gray, O in red, N in blue, S in yellow, and H in white. (b) Influence of the alkyl chain length on CO<sub>2</sub>RR in terms of FE<sub>CO</sub> (left) or *j*<sub>CO</sub> (right) vs. potential. Reproduced with permission from ref. 419. Copyright 2018 American Chemical Society.





Fig. 32 (a) Synthesis of P1-Au NPs. (b) CV scans of OAm-Au NP and P1-Au NP electrodes under  $\text{CO}_2$ -saturated 0.5 M  $\text{KHCO}_3$  at pH 7.3. (c) Controlled-potential electrolysis of OAm-Au NP and P1-Au NP electrodes at  $-0.45$  V vs. RHE over a 72 h time course. Reproduced with permission from ref. 422. Copyright 2018 Wiley-VCH.

cage sizes was tentatively ascribed to a different stabilization of a key ketene intermediate *via* H-bonding interactions with the porphyrin cap.<sup>423</sup> As discussed in Section 3.1.1, stabilizing the H-bonding interaction promoted by pendant amide groups displayed beneficial effects in  $\text{CO}_2\text{RR}$  catalysed by homogeneous Fe porphyrins. Finally, we emphasize that this approach is particularly interesting for the design of bimetallic heterogeneous catalysts by metalation of the porphyrin moiety, merging concepts from molecular catalysis, supramolecular chemistry and surface science.

**6.3.2 Nitrogen- and oxygen-based ligands.** A systematic investigation of the role of the anchoring group on  $\text{CO}_2\text{RR}$  was first carried out by Hwang and coworkers on ligand-stabilized Ag NPs, establishing a direct correlation between the functional group of the capping agent and the  $\text{CO}_2\text{RR}$  activity and selectivity.<sup>424</sup> Capping agents with three different functional groups, *i.e.* amine (oleylamine), carboxylic acid (oleic acid) and thiol (dodecanethiol), were explored, resulting in a striking difference in the product distribution of  $\text{CO}_2\text{RR}$ . The oleylamine-capped Ag NPs showed the highest  $\text{FE}_{\text{CO}}$  (*ca.* 94%), effectively suppressing HER, whereas the dodecanethiol-capped Ag NPs boosted both,  $\text{CO}_2\text{RR}$  and HER, resulting in a poorer CO selectivity, Fig. 33. The general tendency of amine-functionalization to enhance CO selectivity was further probed by the excellent performances obtained by using ethylenediamine (analogous to cysteamine but with two amine groups) as anchoring agent. The experimental results were found to be consistent with the DFT calculations which suggested that amine-capped ligands contribute to destabilize  $^*\text{H}$  adsorption, favoring  $\text{CO}_2\text{RR}$ , while thiol-capped Ag NPs tend to improve indiscriminately both, the HER and  $\text{CO}_2\text{RR}$  rates.<sup>424</sup>



Fig. 33 Schematic illustration of amine- and thiol-capped Ag NPs for  $\text{CO}_2\text{RR}$ . CO faradaic efficiency as a function of the applied potential for oleylamine (OLA)-capped Ag/C, oleic acid (OA)-capped Ag/C, and dodecanethiol (DDT)-capped Ag/C. Reproduced with permission from ref. 424. Copyright 2017 American Chemical Society.

Functionalization with oleylamine, a surfactant commonly used in the wet-chemistry synthesis of metal NPs, displayed an analogous boosting effect on  $\text{CO}_2\text{RR}$  for Au NPs. In this regard, oleylamine-capping was recently reported to drastically enhance the selectivity of small Au NPs toward CO production over HER.<sup>425</sup> The origin of the HER inhibition was ascribed to the preferential binding of oleylamine to the low-coordinated corner sites of the Au NPs, which are the ones favoring  $^*\text{H}$  binding, thus leaving the edge sites free to engage  $^*\text{COOH}$  formation and conversion to CO.<sup>425</sup> The molecular structure of the capping agent was also found to play a role on the catalytic efficiency, resulting in a structure-dependent modification effect: linear amines revealed to be more suitable to promote  $\text{CO}_2\text{RR}$  to CO as compared to the branched amines, with the CO selectivity increasing with the length of the alkyl chain.<sup>426</sup> Across the series, oleylamine provided the best results in terms of either activity and selectivity, suggesting a correlation between the amine structure and the surface coverage. However, the stability of the capping agent under electrochemical conditions should be carefully assessed in order to reliably establish structure–function relationships. In the case of oleylamine-capped Au NPs, some reports indicate that catalyst degradation occurs at negative potentials, likely due to partial ligand detachment,<sup>426</sup> as observed in some molecular systems (see Section 4.1.1).<sup>217</sup> The applied bias-driven loss of surfactant molecules was shown to cause the aggregation of ultrasmall Au NPs, leading to bigger nanostructures that increase the selectivity toward CO production.<sup>427</sup> Contrariwise, dendrimer-encapsulated Au NPs were found to be very stable under electrochemical conditions leading to predominant  $\text{H}_2$  evolution.

In addition to a direct functionalization of metal NPs with organic ligands, the outer coordinative environment of the metal NPs may cooperate with the latter to boost catalysis.



For example, the adsorption of polyvinyl alcohol (PVA) on Au NPs led to a superior selectivity toward CO production compared to the naked Au NPs.<sup>428</sup> It was proposed that the H-bond network at the metal–polymer interface may contribute to stabilize the key \*COOH intermediate, through outer coordination sphere effects analogous to those displayed in homogeneous porphyrin catalysts bearing local phenolic groups (see Section 3.1.1).<sup>120</sup> Moreover, the co-presence of organic molecules on the surface may contribute to the catalytic reaction. Some Au NPs supported on CNTs recently displayed a significantly improved catalytic CO<sub>2</sub>RR performances in the presence of axial pyridine groups covalently grafted on the CNT surface *via* the diazo-reaction.<sup>429</sup> The hybrid catalysts showed excellent faradaic yield for CO production in a wide potential range at low overpotential, which could not be explained by the pyridine alone.<sup>430</sup> Instead, it was proposed that the pyridine group might participate in the rate-limiting \*COOH formation step in a similar manner as previously observed for several molecular systems (Section 3)<sup>168,192,194</sup> and polycrystalline catalysts (see Section 6.3.1).<sup>421</sup>

In an effort to systematically investigate the effect of tailoring the organic component in a hybrid organic/inorganic interface on catalysis, Buonsanti and coworkers recently explored a series of colloidal Ag NCs functionalized with di-substituted imidazolium ligands with varying tail and anchoring groups.<sup>431</sup> This interesting study focused on the key design guidelines to tune the organic component for NP functionalization, dissecting the contribution of each of the three fundamental elements (Fig. 34). The latter are: (i) the anchoring group to the Ag NC, which may affect the electronic structure of the metal surface by direct coordination,

(ii) the imidazolium group, and (iii) the tail group. The probed integrity of the Ag NCs-coordinative organic platform under electrochemical conditions is another remarkable aspect of this study. In these systems, the presence of pendant imidazolium motifs was found to be crucial to achieve high selectivity for CO<sub>2</sub> conversion to CO over HER. This is consistent with the role of co-catalysts in CO<sub>2</sub>RR reported for ionic liquids on metal electrodes<sup>432–435</sup> and in homogeneous molecular catalysis.<sup>97,436</sup> Moreover, in agreement with previous reports,<sup>433</sup> the cationic character of the imidazolium moiety may play an important role in CO<sub>2</sub>RR. We note also that it may help to stabilize negatively charged surface intermediates formed during CO<sub>2</sub>RR *via* Coulombic through-space interactions, in analogy with the reported examples of homogeneous Fe porphyrin catalysts containing pendant imidazolium units<sup>131</sup> or tetramethylammonio groups<sup>112</sup> (Section 3.1.1). Unlike the imidazolium group, the chemical nature of the functional group anchoring on the Ag NC surface showed a less pronounced effect on selectivity.<sup>431</sup> However, XPS analysis provided experimental evidence of an electronic effect of the substituents on the Ag surface, establishing a linear correlation between the specific activity for CO<sub>2</sub>RR to CO with the observed shifts in the Ag 3d<sub>5/2</sub> peaks. As a general trend, electron-withdrawing substituents were found to be beneficial for CO<sub>2</sub>RR, with the NO<sub>2</sub> group providing the best results. Although a reverse effect is generally reported for ligand-stabilized metal NPs (*vide infra*), a possible contribution of the imidazolium moiety may also play a role. Furthermore, the positive impact of electron-poor substituents on CO<sub>2</sub>RR has been reported for several heterogenized heme molecular catalysts (see Section 3.2.2).<sup>183,184</sup> Finally, the tuning of the alkyl tail groups also displayed a strong effect on selectivity, with an intermediate tail length effectively suppressing HER due to a suitable interplay between an increased local hydrophobicity on the catalytic surface and without an excessive steric bulkiness.<sup>431</sup> The steric hindrance of a long tail group reduces the accessibility of the electrolyte and CO<sub>2</sub> to the metal surface, analogously as previously discussed for tetraazamacrocyclic Ni catalysts with *N*-alkyl substituents (see Section 4.1.1).

These findings highlight how traditional concepts of organometallic chemistry (*e.g.*, steric and electronic effects, second coordination sphere interactions, hydrophobic/hydrophilic interaction, *etc.*) can be effectively used to improve the understanding of the organic/inorganic interface at a molecular level and to tailor heterogeneous catalysts. Several representative examples of functional organometallic surfaces, based on bulk metal electrodes chemically interacting with nitrogen-based organic additives (*e.g.* ionic liquids,<sup>432–435</sup> aminoacids,<sup>437</sup> *N*-arylpiperidinium<sup>438–440</sup> or *N,N'*-phenanthroline,<sup>441</sup> benzimidazole,<sup>442</sup> polyamines,<sup>443</sup> polyaniline,<sup>444</sup> triazole,<sup>445</sup> *etc.*) or supramolecular organic assemblies,<sup>446</sup> have been also recently reported for CO<sub>2</sub>RR.<sup>447</sup>

**6.3.3 N-Heterocyclic carbenes (NHC).** N-Heterocyclic carbenes (NHC) also represent an important class of organic molecules effectively employed to improve the CO<sub>2</sub>RR catalytic performances of metal NPs.<sup>448</sup> Chelating multidentate NHC ligands have been successfully used for CO<sub>2</sub> electroreduction in homogeneous



Fig. 34 Overview of the effect of imidazolium ligands on an AgNC surface during the CO<sub>2</sub>RR. Reproduced with permission from ref. 431. Copyright 2019 Royal Society of Chemistry.



molecular catalysts<sup>449–452</sup> and polycrystalline metallic surfaces (*vide infra*).<sup>453</sup> The strong  $\sigma$ -donating character of the NHC ligands is particularly attractive for CO<sub>2</sub>RR, leading to electron-rich metal surfaces with an enhanced reactivity towards CO<sub>2</sub>. Moreover, their ability to form highly stable M–C bonds with transition metal atoms enables to improve the catalyst stability under electrochemical reductive conditions, preventing nano-clustering deactivation effects.

Due to these favorable properties, Au NPs functionalized with monodentate NHC molecules exhibited a substantially improved CO<sub>2</sub>RR behavior as compared to the parent Au NPs in terms of FE (83% *vs.* 53%) and current densities (7.6-fold increase) for CO production at an overpotential of 460 mV, Fig. 35.<sup>454</sup> The NHC ligation was found to alter the electronic structure of the Au surface, affecting the reaction pathway. For the bare Au NPs, kinetics analysis based on Tafel slope was consistent with a rate-determining step based on a single electron transfer to the adsorbed CO<sub>2</sub> to form \*CO<sub>2</sub>\*<sup>•−</sup>. Contrariwise, the lower slope obtained for NHC-stabilized Au NPs suggested that it may undergo a pre-equilibrium one-electron transfer followed by a rate-limiting chemical step. Such a change of the mechanistic pathway was ascribed to the strong  $\sigma$ -donating electronic effect induced by the molecular ligand, which promotes a fast electron transfer prior to the rate-determining step.<sup>454</sup> Notably, it was also proposed that the strong Au–C bond may destabilize the neighboring Au–Au surface bonds, causing a restructuring of the Au surface which resulted in improved CO<sub>2</sub>RR kinetics.

As mentioned above, the reported NHC-functionalized Au NPs<sup>454</sup> or nanoclusters<sup>455</sup> displayed good CO<sub>2</sub>RR selectivity and stability under electrochemical conditions. Recently, the encapsulation of metal NPs into monodentate or polydentate polymeric NHC matrices was explored as an effective strategy to further improve at the same time catalyst selectivity and long-term durability, preventing nano-clustering.<sup>456</sup> The embedded Au NPs exhibited excellent FE<sub>CO</sub> with a *ca.* 86% activity retention over 11 h electrolysis under CO<sub>2</sub> atmosphere at −0.9 V *vs.* RHE, clearly outperforming the bare Au NPs which lost

approximately 90% of their initial activity. The improved performance was ascribed to the electronic effect exerted by NHC ligands and the hydrophobicity of the polymer matrix, the latter helping to suppress HER and control the surface accessibility as observed for polymer-encapsulated molecular catalysts (Section 3). To further confirm the beneficial role played by the NHC polymer on catalysis, an analogous effect was also observed for Pd NPs, which showed an increase in the CO selectivity and stability as compared to commercial Pd/C.<sup>456</sup>

In addition to metal NPs, the functionalization of NHCs was recently reported to affect the catalytic properties of polycrystalline metal surfaces. In particular, Pd electrodes modified with tridentate NHC ligands displayed a 32-fold activity enhancement for CO<sub>2</sub> conversion to C<sub>1</sub> products as compared to an unmodified Pd foil, producing HCOO<sup>−</sup> in high faradaic yields.<sup>457</sup> The electron-rich Pd surface induced by tris-NHC ligation led to a more favorable pathway for HCOO<sup>−</sup> production. While subtle differences were observed in catalysis upon tuning the alkyl *N*-substituents of the ligand, the NHC chelation showed a remarkable effect on the catalyst stability, with Tris-NHC ligands providing considerably higher durability than the bare Pd foil and the monodentate counterpart.<sup>457</sup> Further investigation is needed to fully rationalize the influence of NHC ligands on the catalytic CO<sub>2</sub>RR as a function of the denticity and the type of substituents. Moreover, a spectroscopic investigation of the spatial orientation and coordination mode of NHC moieties on different metallic surfaces will provide useful insights to modulate the reactivity of the organic/inorganic interface towards CO<sub>2</sub>RR.<sup>458–462</sup>

## 7. Conclusions

In this work we have summarized the main advances achieved in the rational design of transition metal-based catalysts for the electrochemical conversion of CO<sub>2</sub> into higher-energy carbon products. With a special focus on structural effects, we have provided a critical comparison of the main design principles directing the development of different types of catalysts, ranging from molecular systems to single-atom and nano-structured catalysts. For molecular systems based on heme and non-heme macrocyclic ligands, we presented detailed studies investigating the effect of the first and second coordination sphere on the catalytic activity, selectivity and overpotential of both, homogeneous and heterogenized catalysts. These studies revealed that molecular systems can be suitable catalysts for scaling-up a selective CO<sub>2</sub>RR under appropriate conditions. In addition to the conventional physical and chemical functionalization methods, alternative approaches for molecular catalyst confinement were explored, including the encapsulation into polymeric matrices, porous organic or metalorganic 3D frameworks and supramolecular assemblies. The main strategies adopted for the design of single-atom and nano-structured catalysts were also discussed. As compared to the corresponding bulk metallic surfaces, molecular-like catalysts show an intrinsically higher selectivity towards CO<sub>2</sub> due to the



Fig. 35 Schematic illustration of NHC-carbene functionalized Au NPs for CO<sub>2</sub>RR to CO. Partial current density and Tafel plot for CO production for Au–Cb NP and Au NP/C. Reproduced with permission from ref. 454. Copyright 2016 American Chemical Society.



specificity of their active site. For molecular and single-atom catalysts, earth-abundant 1st row transition metals (*e.g.* Mn, Fe, Ni, Co) are typically used for efficient and selective CO<sub>2</sub>RR in both, organic and aqueous media.

We have reviewed the electrocatalytic CO<sub>2</sub>RR properties of the main families of molecular, single-atom and nanostructured catalysts on the basis of their specific structure–function relationships as well as in relation with their dependence on a number of experimental factors, including the electrode/support material, pH, buffer, electrolyte or the applied potential. In homogeneous systems, structural effects related to the metalorganic active moiety are predominant, with the electrode surface working as an electron collector and the molecular catalyst being usually dissolved in organic media. Contrariwise, for heterogeneous catalysts, the nature of the support material as well as the support–catalyst interaction strongly affect the catalytic properties.

Taken together, the studies reported herein suggest that a close connection between homogeneous and heterogeneous CO<sub>2</sub>RR electrocatalysis would be beneficial for both fields. From one side, the lessons of traditional coordination chemistry and the concepts developed in molecular catalysis may be extremely helpful to overcome the limits of the current heterogeneous catalysts, especially in terms of selectivity. On the other hand, the application of methods and tools used in materials science and heterogeneous catalysis to molecular systems would contribute to extend their applicability. We are confident that the principles for rational catalyst design summarized above will contribute to the further development of new efficient transition metal-based catalysts for efficient and selective electrochemical reduction of CO<sub>2</sub>.

## 8. Outlook

The studies presented herein serve to shed light on a variety of strategies adopted in the past to improve the efficiency of transition metal-based CO<sub>2</sub>RR catalysts. At different levels of complexity, the CO<sub>2</sub>RR activity and selectivity are extremely sensitive to the catalyst structure. In this regard, further development of electrochemical and *in situ/operando* spectro-electrochemical techniques is needed to improve the mechanistic understanding of the CO<sub>2</sub>RR process and to elucidate structure–function relationships as powerful tools for catalyst optimization. Moreover, new advances in the spectroscopic and microscopic techniques are required to achieve atomic or molecular structural details for the characterization of catalytic materials. In particular, single-atom catalysts show unique physico-chemical properties and an improvement in their structural characterization would allow to more accurately correlate their activity with specific structural features of the active site. This will be a major challenge in the field of energy conversion in the coming decades. Furthermore, an increase of the atomic aggregation level usually leads to a more favorable HER (especially in aqueous electrolyte) or to a catalytic inactivity, as indicated by the deactivation of molecular-like catalysts due to

particle sintering. In this respect, monitoring the dynamic changes of the catalyst structure under operating conditions would also allow to elucidate the deactivation pathway, which is a crucial aspect for catalyst optimization in both homogeneous and heterogeneous catalysis.

Another promising perspective for future research is a more in-depth investigation of the organic/inorganic interface of hybrid materials, by combining the basic principles and concepts of conventional coordination chemistry with the methods traditionally employed in surface science. Several examples reported in this work showed that the electronic properties of metal catalysts can be effectively tuned by modulating the stereo-electronic features of the surrounding organic or heteroatom-rich framework (*e.g.* reticular effect in molecular catalysts encapsulated into porous 3D frameworks or organic molecules anchored to metal NPs or polycrystalline metallic surfaces). However, systematic studies on the nature of these interactions as well as their effect on catalysis are rare, leaving much room for future investigation. The extreme versatility of this approach also offers the opportunity to explore several different strategies for catalyst optimization, based on chemical (coordination) or physical (electrostatic, hydrophobic) interactions at the metal–organic interface. In this scenario, the outer coordination sphere effects, reminiscent of the spatial interactions occurring in the active site of enzymes, deserve to be studied in more detail in both homogeneous and heterogeneous catalysts. For homogeneous molecular systems, they were rationalized to be an effective way to break scaling relationships, leading to an outstanding improvement of the catalytic rates and selectivity. In heterogeneous catalysis, these interactions have been less explored and can be described in terms of matrix effects, as recently reported for molecular catalysts embedded into conductive surfaces.<sup>194</sup> The development of novel model systems and in-depth experimental kinetic analysis would be extremely important to further rationalize and dissect these effects.

In parallel with more detailed mechanistic studies and the investigation of new strategies for catalyst optimization based on structural effects, much effort should be directed to tackle the main technological and physical challenges related to the implementation of the heterogeneous and molecular catalysts into real devices. In particular, the use of standard electrolyzers or flow cell setups for testing the long-term performance of transition metal catalysts is highly encouraged to explore their practical applicability. This would also improve catalyst benchmarking, facilitating a systematic comparison of the different catalysts reported in the literature. For molecular homogeneous catalysts, the development of novel heterogenization strategies needs to be accompanied by their implementation in real devices, as suggested by some promising preliminary studies.<sup>187</sup> At the same time, novel strategies based on the combination of CO<sub>2</sub>RR with other oxidative electro-synthetic processes (*e.g.* organic substrates) should be explored, as well as alternative approaches to utilize the CO<sub>2</sub>RR products (*e.g.* carbon monoxide) as precursors or building blocks for the synthesis of commodity chemicals.



## Conflicts of interest

The authors declare no competing interest.

## Acknowledgements

This work was funded by the European Research Council under grant ERC-OPERANDOCAT (ERC-725915) and the Deutsche Forschungsgemeinschaft (DFG, German Research Foundation) – project no. 406944504 – SPP 2080 and SFB 1316, subproject B1, as well as Germany's Excellence Strategy – EXC 2008/1 (UniSysCat) – 390540038. Open Access funding provided by the Max Planck Society.

## Notes and references

- S. Chu and A. Majumdar, *Nature*, 2012, **488**, 294–303.
- M. Aresta, A. Dibenedetto and A. Angelini, *Chem. Rev.*, 2014, **114**, 1709–1742.
- A. Majumdar and J. Deutch, *Joule*, 2018, **2**, 805–809.
- J. C. Abanades, E. S. Rubin, M. Mazzotti and H. J. Herzog, *Energy Environ. Sci.*, 2017, **10**, 2491–2499.
- E. V. Kondratenko, G. Mul, J. Baltrusaitis, G. O. Larrazábal and J. Pérez-Ramírez, *Energy Environ. Sci.*, 2013, **6**, 3112–3135.
- C. Chen, J. F. Khosrowabadi Kotyk and S. W. Sheehan, *Chem*, 2018, **4**, 2571–2586.
- O. S. Bushuyev, P. De Luna, C. T. Dinh, L. Tao, G. Saur, J. van de Lagemaat, S. O. Kelley and E. H. Sargent, *Joule*, 2018, **2**, 825–832.
- R. Krause, D. Reinisch, C. Reller, H. Eckert, D. Hartmann, D. Taroata, K. Wiesner-Fleischer, A. Bulan, A. Lueken and G. Schmid, *Chem. Ing. Tech.*, 2020, **92**, 53–61.
- Q. Liu, L. Wu, R. Jackstell and M. Beller, *Nat. Commun.*, 2015, **6**, 5933.
- R. Kortlever, J. Shen, K. J. P. Schouten, F. Calle-Vallejo and M. T. M. Koper, *J. Phys. Chem. Lett.*, 2015, **6**, 4073–4082.
- J. Schneider, H. Jia, J. T. Muckerman and E. Fujita, *Chem. Soc. Rev.*, 2012, **41**, 2036–2051.
- J.-M. Savéant, *Chem. Rev.*, 2008, **108**, 2111–2112.
- E. E. Benson, C. P. Kubiak, A. J. Sathrum and J. M. Smieja, *Chem. Soc. Rev.*, 2009, **38**, 89–99.
- J. Qiao, Y. Liu, F. Hong and J. Zhang, *Chem. Soc. Rev.*, 2014, **43**, 631–675.
- M. König, J. Vaes, E. Klemm and D. Pant, *iScience*, 2019, **19**, 135–160.
- H. Takeda, C. Cometto, O. Ishitani and M. Robert, *ACS Catal.*, 2017, **7**, 70–88.
- R. Francke, B. Schille and M. Roemelt, *Chem. Rev.*, 2018, **118**, 4631–4701.
- S. Fukuzumi, Y.-M. Lee, H. S. Ahn and W. Nam, *Chem. Sci.*, 2018, **9**, 6017–6034.
- K. Elouarzaki, V. Kannan, V. Jose, H. S. Sabharwal and J.-M. Lee, *Adv. Energy Mater.*, 2019, **9**, 1900090.
- F. Franco, S. Fernández and J. Lloret-Fillol, *Curr. Opin. Electrochem.*, 2019, **15**, 109–117.
- B. Zhang and L. Sun, *Chem. Soc. Rev.*, 2019, **48**, 2216–2264.
- C. Jiang, A. W. Nichols and C. W. Machan, *Dalton Trans.*, 2019, **48**, 9454–9468.
- L. Zhang, Z.-J. Zhao and J. Gong, *Angew. Chem., Int. Ed.*, 2017, **56**, 11326–11353.
- Z. Yin, G. T. R. Palmore and S. Sun, *Trends Chem.*, 2019, **1**, 739–750.
- G. Zhao, X. Huang, X. Wang and X. Wang, *J. Mater. Chem. A*, 2017, **5**, 21625–21649.
- J.-H. Zhou and Y.-W. Zhang, *React. Chem. Eng.*, 2018, **3**, 591–625.
- W. Zhang, Y. Hu, L. Ma, G. Zhu, Y. Wang, X. Xue, R. Chen, S. Yang and Z. Jin, *Adv. Sci.*, 2018, **5**, 1700275.
- C. W. Machan, M. D. Sampson, S. A. Chabolla, T. Dang and C. P. Kubiak, *Organometallics*, 2014, **33**, 4550–4559.
- T. E. Rosser and E. Reisner, *ACS Catal.*, 2017, **7**, 3131–3141.
- K. J. Lee, N. Elgrishi, B. Kandemir and J. L. Dempsey, *Nat. Rev. Chem.*, 2017, **1**, 0039.
- A. Ge, B. Rudshiteyn, P. E. Videla, C. J. Miller, C. P. Kubiak, V. S. Batista and T. Lian, *Acc. Chem. Res.*, 2019, **52**, 1289–1300.
- C. W. Machan, *Curr. Opin. Electrochem.*, 2019, **15**, 42–49.
- C. S. Diercks, Y. Liu, K. E. Cordova and O. M. Yaghi, *Nat. Mater.*, 2018, **17**, 301–307.
- P. Shao, L. Yi, S. Chen, T. Zhou and J. Zhang, *J. Energy Chem.*, 2020, **40**, 156–170.
- G. Yilmaz, S. B. Peh, D. Zhao and G. W. Ho, *Adv. Sci.*, 2019, **6**, 1901129.
- L. Wang, W. Chen, D. Zhang, Y. Du, R. Amal, S. Qiao, J. Wu and Z. Yin, *Chem. Soc. Rev.*, 2019, **48**, 5310–5349.
- Y. Zhu, W. Peng, Y. Li, G. Zhang, F. Zhang and X. Fan, *Small Methods*, 2019, **3**, 1800438.
- J. A. Trindell, Z. Duan, G. Henkelman and R. M. Crooks, *Chem. Rev.*, 2020, **120**(2), 814–850.
- R. M. Arán-Ais, D. Gao and B. Roldan Cuenya, *Acc. Chem. Res.*, 2018, **51**, 2906–2917.
- D. Gao, R. M. Arán-Ais, H. S. Jeon and B. Roldan Cuenya, *Nat. Catal.*, 2019, **2**, 198–210.
- P. Sebastián-Pascual, S. Mezzavilla, I. E. L. Stephens and M. Escudero-Escribano, *ChemCatChem*, 2019, **11**, 3626–3645.
- D. C. Grills, M. Z. Ertem, M. McKinnon, K. T. Ngo and J. Rochford, *Coord. Chem. Rev.*, 2018, **374**, 173–217.
- N. Elgrishi, M. B. Chambers, X. Wang and M. Fontecave, *Chem. Soc. Rev.*, 2017, **46**, 761–796.
- K. E. Dalle, J. Warnan, J. J. Leung, B. Reuillard, I. S. Karmel and E. Reisner, *Chem. Rev.*, 2019, **119**, 2752–2875.
- N. Corbin, J. Zeng, K. Williams and K. Manthiram, *Nano Res.*, 2019, **12**, 2093–2125.
- X.-M. Hu, S. U. Pedersen and K. Daasbjerg, *Curr. Opin. Electrochem.*, 2019, **15**, 148–154.
- C. Costentin and J.-M. Savéant, *Nat. Rev. Chem.*, 2017, **1**, 0087.
- A. W. Nichols and C. W. Machan, *Front. Chem.*, 2019, **7**, 397.
- Y. Matsubara, *ACS Energy Lett.*, 2019, **4**, 1999–2004.
- B. Das, A. Thapper, S. Ott and S. B. Colbran, *Sustainable Energy Fuels*, 2019, **3**, 2159–2175.



- 51 J. Shen, R. Kortlever, R. Kas, Y. Y. Birdja, O. Diaz-Morales, Y. Kwon, I. Ledezma-Yanez, K. J. P. Schouten, G. Mul and M. T. M. Koper, *Nat. Commun.*, 2015, **6**, 8177.
- 52 E. Boutin, M. Wang, J. C. Lin, M. Mesnage, D. Mendoza, B. Lassalle-Kaiser, C. Hahn, T. F. Jaramillo and M. Robert, *Angew. Chem., Int. Ed.*, 2019, **58**, 16172–16176.
- 53 Y. Wu, Z. Jiang, X. Lu, Y. Liang and H. Wang, *Nature*, 2019, **575**, 639–642.
- 54 S. Mezzavilla, S. Horch, I. E. L. Stephens, B. Seger and I. Chorkendorff, *Angew. Chem.*, 2019, **131**, 3814–3818.
- 55 Y. Hori, in *Modern Aspects of Electrochemistry*, ed. C. Vayenas, R. White and M. Gamboa-Aldeco, Springer New York, 2008, ch. 3, vol. 42, pp. 89–189.
- 56 Y.-J. Zhang, V. Sethuraman, R. Michalsky and A. A. Peterson, *ACS Catal.*, 2014, **4**, 3742–3748.
- 57 A. Bagger, W. Ju, A. S. Varela, P. Strasser and J. Rossmeisl, *ChemPhysChem*, 2017, **18**, 3266–3273.
- 58 X. Liu, J. Xiao, H. Peng, X. Hong, K. Chan and J. K. Nørskov, *Nat. Commun.*, 2017, **8**, 15438.
- 59 Y. Hori, A. Murata, R. Takahashi and S. Suzuki, *J. Chem. Soc., Chem. Commun.*, 1988, 17–19, DOI: 10.1039/C39880000017.
- 60 K. P. Kuhl, E. R. Cave, D. N. Abram and T. F. Jaramillo, *Energy Environ. Sci.*, 2012, **5**, 7050–7059.
- 61 Y. Liu, Y. Zhang, K. Cheng, X. Quan, X. Fan, Y. Su, S. Chen, H. Zhao, Y. Zhang, H. Yu and M. R. Hoffmann, *Angew. Chem., Int. Ed.*, 2017, **56**, 15607–15611.
- 62 Q. H. Low, N. W. X. Loo, F. Calle-Vallejo and B. S. Yeo, *Angew. Chem., Int. Ed.*, 2019, **58**, 2256–2260.
- 63 Y. Huang, A. D. Handoko, P. Hirunsit and B. S. Yeo, *ACS Catal.*, 2017, **7**, 1749–1756.
- 64 C. Reller, R. Krause, E. Volkova, B. Schmid, S. Neubauer, A. Rucki, M. Schuster and G. Schmid, *Adv. Energy Mater.*, 2017, **7**, 1602114.
- 65 C. S. Le Duff, M. J. Lawrence and P. Rodriguez, *Angew. Chem., Int. Ed.*, 2017, **56**, 12919–12924.
- 66 R. M. Bullock, A. K. Das and A. M. Appel, *Chem. – Eur. J.*, 2017, **23**, 7626–7641.
- 67 M. Das Bairagya, R. J. Bujol and N. Elgrishi, *Chem. – Eur. J.*, 2020, **26**, 1–11.
- 68 C. Costentin, M. Robert, J.-M. Savéant and A. Tatin, *Proc. Natl. Acad. Sci. U. S. A.*, 2015, **112**, 6882.
- 69 A. Taheri, E. J. Thompson, J. C. Fettingner and L. A. Berben, *ACS Catal.*, 2015, **5**, 7140–7151.
- 70 G. Neri, I. M. Aldous, J. J. Walsh, L. J. Hardwick and A. J. Cowan, *Chem. Sci.*, 2016, **7**, 1521–1526.
- 71 J. J. Walsh, G. Neri, C. L. Smith and A. J. Cowan, *Organometallics*, 2019, **38**, 1224–1229.
- 72 X.-M. Hu, Z. Salmi, M. Lillethorup, E. B. Pedersen, M. Robert, S. U. Pedersen, T. Skrydstrup and K. Daasbjerg, *Chem. Commun.*, 2016, **52**, 5864–5867.
- 73 S. A. Yao, R. E. Ruther, L. Zhang, R. A. Franking, R. J. Hamers and J. F. Berry, *J. Am. Chem. Soc.*, 2012, **134**, 15632–15635.
- 74 N. Elgrishi, S. Griveau, M. B. Chambers, F. Bedioui and M. Fontecave, *Chem. Commun.*, 2015, **51**, 2995–2998.
- 75 J. D. Blakemore, A. Gupta, J. J. Warren, B. S. Brunshwig and H. B. Gray, *J. Am. Chem. Soc.*, 2013, **135**, 18288–18291.
- 76 N. Kornienko, Y. Zhao, C. S. Kley, C. Zhu, D. Kim, S. Lin, C. J. Chang, O. M. Yaghi and P. Yang, *J. Am. Chem. Soc.*, 2015, **137**, 14129–14135.
- 77 S. Wan, F. Gándara, A. Asano, H. Furukawa, A. Saeki, S. K. Dey, L. Liao, M. W. Ambrogio, Y. Y. Botros, X. Duan, S. Seki, J. F. Stoddart and O. M. Yaghi, *Chem. Mater.*, 2011, **23**, 4094–4097.
- 78 S. Lin, C. S. Diercks, Y.-B. Zhang, N. Kornienko, E. M. Nichols, Y. Zhao, A. R. Paris, D. Kim, P. Yang, O. M. Yaghi and C. J. Chang, *Science*, 2015, **349**, 1208–1213.
- 79 H.-J. Zhu, M. Lu, Y.-R. Wang, S.-J. Yao, M. Zhang, Y.-H. Kan, J. Liu, Y. Chen, S.-L. Li and Y.-Q. Lan, *Nat. Commun.*, 2020, **11**, 497.
- 80 Z. Yang, X. Zhang, C. Long, S. Yan, Y. Shi, J. Han, J. Zhang, P. An, L. Chang and Z. Tang, *CrystEngComm*, 2020, **22**, 1619–1624.
- 81 V. S. P. K. Neti, X. Wu, S. Deng and L. Echegoyen, *Polym. Chem.*, 2013, **4**, 4566–4569.
- 82 H. Liu, J. Chu, Z. Yin, X. Cai, L. Zhuang and H. Deng, *Chem*, 2018, **4**, 1696–1709.
- 83 C. Costentin and J.-M. Savéant, *Curr. Opin. Electrochem.*, 2019, **15**, 58–65.
- 84 K. J. Lee, B. D. McCarthy and J. L. Dempsey, *Chem. Soc. Rev.*, 2019, **48**, 2927–2945.
- 85 C. Costentin, S. Drouet, M. Robert and J.-M. Savéant, *J. Am. Chem. Soc.*, 2012, **134**, 11235–11242.
- 86 C. Costentin, S. Drouet, G. Passard, M. Robert and J.-M. Savéant, *J. Am. Chem. Soc.*, 2013, **135**, 9023–9031.
- 87 C. Costentin, G. Passard, M. Robert and J.-M. Savéant, *J. Am. Chem. Soc.*, 2014, **136**, 11821–11829.
- 88 M. Hammouche, D. Lexa, J. M. Savéant and M. Momenteau, *J. Electroanal. Chem. Interfacial Electrochem.*, 1988, **249**, 347–351.
- 89 C. Costentin, J.-M. Savéant and C. Tard, *Proc. Natl. Acad. Sci. U. S. A.*, 2018, **115**, 9104–9109.
- 90 C. Römel, J. Song, M. Tarrago, J. A. Rees, M. van Gastel, T. Weyhermüller, S. DeBeer, E. Bill, F. Neese and S. Ye, *Inorg. Chem.*, 2017, **56**, 4745–4750.
- 91 C. Römel, S. Ye, E. Bill, T. Weyhermüller, M. van Gastel and F. Neese, *Inorg. Chem.*, 2018, **57**, 2141–2148.
- 92 P. A. Davethu and S. P. de Visser, *J. Phys. Chem. A*, 2019, **123**, 6527–6535.
- 93 M. Hammouche, D. Lexa, M. Momenteau and J. M. Savéant, *J. Am. Chem. Soc.*, 1991, **113**, 8455–8466.
- 94 I. Bhugun, D. Lexa and J.-M. Savéant, *J. Phys. Chem.*, 1996, **100**, 19981–19985.
- 95 I. Bhugun, D. Lexa and J.-M. Savéant, *J. Am. Chem. Soc.*, 1994, **116**, 5015–5016.
- 96 I. Bhugun, D. Lexa and J.-M. Savéant, *J. Am. Chem. Soc.*, 1996, **118**, 1769–1776.
- 97 J. Choi, T. M. Benedetti, R. Jalili, A. Walker, G. G. Wallace and D. L. Officer, *Chem. – Eur. J.*, 2016, **22**, 14158–14161.
- 98 C. Costentin, M. Robert and J.-M. Savéant, *Acc. Chem. Res.*, 2015, **48**, 2996–3006.
- 99 B. Mondal, A. Rana, P. Sen and A. Dey, *J. Am. Chem. Soc.*, 2015, **137**, 11214–11217.



- 100 E. A. Mohamed, Z. N. Zahran and Y. Naruta, *Chem. Commun.*, 2015, **51**, 16900–16903.
- 101 C. Costentin, M. Robert and J.-M. Savéant, *Chem. Soc. Rev.*, 2013, **42**, 2423–2436.
- 102 J. Bonin, A. Maurin and M. Robert, *Coord. Chem. Rev.*, 2017, **334**, 184–198.
- 103 C. Costentin, M. Robert, J.-M. Savéant and C. Tard, *Acc. Chem. Res.*, 2014, **47**, 271–280.
- 104 M. T. Jensen, M. H. Rønne, A. K. Ravn, R. W. Juhl, D. U. Nielsen, X.-M. Hu, S. U. Pedersen, K. Daasbjerg and T. Skrydstrup, *Nat. Commun.*, 2017, **8**, 489.
- 105 D. U. Nielsen, X.-M. Hu, K. Daasbjerg and T. Skrydstrup, *Nat. Catal.*, 2018, **1**, 244–254.
- 106 C. G. Margarit, N. G. Asimow, C. Costentin and D. G. Nocera, *ACS Energy Lett.*, 2019, 72–78, DOI: 10.1021/acsenerylett.9b02093.
- 107 J. M. Barlow and J. Y. Yang, *ACS Cent. Sci.*, 2019, **5**, 580–588.
- 108 K. M. Waldie, A. L. Ostericher, M. H. Reineke, A. F. Sasayama and C. P. Kubiak, *ACS Catal.*, 2018, **8**, 1313–1324.
- 109 C. Costentin and J.-M. Savéant, *J. Am. Chem. Soc.*, 2017, **139**, 8245–8250.
- 110 I. Azcarate, C. Costentin, M. Robert and J.-M. Savéant, *J. Phys. Chem. C*, 2016, **120**, 28951–28960.
- 111 J. D. B. Koenig, J. Willkomm, R. Roesler, W. E. Piers and G. C. Welch, *ACS Appl. Energy Mater.*, 2019, **2**, 4022–4026.
- 112 I. Azcarate, C. Costentin, M. Robert and J.-M. Savéant, *J. Am. Chem. Soc.*, 2016, **138**, 16639–16644.
- 113 M. L. Pegis, B. A. McKeown, N. Kumar, K. Lang, D. J. Wasylenko, X. P. Zhang, S. Raugai and J. M. Mayer, *ACS Cent. Sci.*, 2016, **2**, 850–856.
- 114 Y.-H. Wang, M. L. Pegis, J. M. Mayer and S. S. Stahl, *J. Am. Chem. Soc.*, 2017, **139**, 16458–16461.
- 115 C. M. Klug, A. J. P. Cardenas, R. M. Bullock, M. O'Hagan and E. S. Wiedner, *ACS Catal.*, 2018, **8**, 3286–3296.
- 116 D. L. DuBois, *Inorg. Chem.*, 2014, **53**, 3935–3960.
- 117 C. Costentin and J.-M. Savéant, *J. Am. Chem. Soc.*, 2018, **140**, 16669–16675.
- 118 W. J. Shaw, M. L. Helm and D. L. DuBois, *Biochim. Biophys. Acta, Bioenerg.*, 2013, **1827**, 1123–1139.
- 119 A. Chapovetsky, T. H. Do, R. Haiges, M. K. Takase and S. C. Marinescu, *J. Am. Chem. Soc.*, 2016, **138**, 5765–5768.
- 120 C. Costentin, S. Drouet, M. Robert and J.-M. Savéant, *Science*, 2012, **338**, 90–94.
- 121 C. Costentin, G. Passard, M. Robert and J.-M. Savéant, *Proc. Natl. Acad. Sci. U. S. A.*, 2014, **111**, 14990–14994.
- 122 S. Sinha and J. J. Warren, *Inorg. Chem.*, 2018, **57**, 12650–12656.
- 123 B. Zhao, H. Lei, N. Wang, G. Xu, W. Zhang and R. Cao, *Chem. – Eur. J.*, 2020, **26**, 4007–4012.
- 124 C. G. Margarit, C. Schnedermann, N. G. Asimow and D. G. Nocera, *Organometallics*, 2019, **38**, 1219–1223.
- 125 Eva M. Nichols, J. S. Derrick, S. K. Nistanaki, P. T. Smith and C. J. Chang, *Chem. Sci.*, 2018, **9**, 2952–2960.
- 126 P. Gotico, B. Boitrel, R. Guillot, M. Sircoglou, A. Quaranta, Z. Halime, W. Leibl and A. Aukauloo, *Angew. Chem., Int. Ed.*, 2019, **58**, 4504–4509.
- 127 P. Sen, B. Mondal, D. Saha, A. Rana and A. Dey, *Dalton Trans.*, 2019, **48**, 5965–5977.
- 128 T. R. Cundari, A. K. Wilson, M. L. Drummond, H. E. Gonzalez, K. R. Jorgensen, S. Payne, J. Braunfeld, M. De Jesus and V. M. Johnson, *J. Chem. Inf. Model.*, 2009, **49**, 2111–2115.
- 129 M. L. Pegis, J. A. S. Roberts, D. J. Wasylenko, E. A. Mader, A. M. Appel and J. M. Mayer, *Inorg. Chem.*, 2015, **54**, 11883–11888.
- 130 Y. Matsubara, D. C. Grills and Y. Kuwahara, *ACS Catal.*, 2015, **5**, 6440–6452.
- 131 A. Khadhraoui, P. Gotico, B. Boitrel, W. Leibl, Z. Halime and A. Aukauloo, *Chem. Commun.*, 2018, **54**, 11630–11633.
- 132 A. Maurin and M. Robert, *Chem. Commun.*, 2016, **52**, 12084–12087.
- 133 A. Maurin and M. Robert, *J. Am. Chem. Soc.*, 2016, **138**, 2492–2495.
- 134 J.-H. Jeoung and H. Dobbek, *Science*, 2007, **318**, 1461–1464.
- 135 F. Liu, T. Cardolaccia, B. J. Hornstein, J. R. Schoonover and T. J. Meyer, *J. Am. Chem. Soc.*, 2007, **129**, 2446–2447.
- 136 E. A. Mohamed, Z. N. Zahran and Y. Naruta, *Chem. Mater.*, 2017, **29**, 7140–7150.
- 137 A. Tatin, C. Comminges, B. Kokoh, C. Costentin, M. Robert and J.-M. Savéant, *Proc. Natl. Acad. Sci. U. S. A.*, 2016, **113**, 5526–5529.
- 138 J. Choi, P. Wagner, R. Jalili, J. Kim, D. R. MacFarlane, G. G. Wallace and D. L. Officer, *Adv. Energy Mater.*, 2018, **8**, 1801280.
- 139 J. Choi, J. Kim, P. Wagner, S. Gambhir, R. Jalili, S. Byun, S. Sayyar, Y. M. Lee, D. R. MacFarlane, G. G. Wallace and D. L. Officer, *Energy Environ. Sci.*, 2019, **12**, 747–755.
- 140 I. Hod, M. D. Sampson, P. Deria, C. P. Kubiak, O. K. Farha and J. T. Hupp, *ACS Catal.*, 2015, **5**, 6302–6309.
- 141 B.-X. Dong, S.-L. Qian, F.-Y. Bu, Y.-C. Wu, L.-G. Feng, Y.-L. Teng, W.-L. Liu and Z.-W. Li, *ACS Appl. Energy Mater.*, 2018, **1**, 4662–4669.
- 142 P. L. Cheung, S. K. Lee and C. P. Kubiak, *Chem. Mater.*, 2019, **31**, 1908–1919.
- 143 P. T. Smith, B. P. Benke, Z. Cao, Y. Kim, E. M. Nichols, K. Kim and C. J. Chang, *Angew. Chem., Int. Ed.*, 2018, **57**, 9684–9688.
- 144 H. Kazuya, T. Katsuhiko, S. Hideo and T. Shinobu, *Chem. Lett.*, 1977, 1137–1140.
- 145 T. Katsuhiko, H. Kazuya, S. Hideo and T. Shinobu, *Chem. Lett.*, 1979, 305–308.
- 146 D. Behar, T. Dhanasekaran, P. Neta, C. M. Hosten, D. Ejeh, P. Hambright and E. Fujita, *J. Phys. Chem. A*, 1998, **102**, 2870–2877.
- 147 B. Hu, W. Xie, R. Li, Z. Pan, S. Song and Y. Wang, *Electrochim. Acta*, 2019, 135283, DOI: 10.1016/j.electacta.2019.135283.
- 148 S. Aoi, K. Mase, K. Ohkubo and S. Fukuzumi, *Chem. Commun.*, 2015, **51**, 10226–10228.
- 149 J. Grodkowski, P. Neta, E. Fujita, A. Mahammed, L. Simkhovich and Z. Gross, *J. Phys. Chem. A*, 2002, **106**, 4772–4778.



- 150 A. Ogawa, K. Oohora, W. Gu and T. Hayashi, *Chem. Commun.*, 2019, **55**, 493–496.
- 151 A. Ogawa, K. Oohora and T. Hayashi, *Inorg. Chem.*, 2018, **57**, 14644–14652.
- 152 X.-M. Hu, M. H. Rønne, S. U. Pedersen, T. Skrydstrup and K. Daasbjerg, *Angew. Chem., Int. Ed.*, 2017, **56**, 6468–6472.
- 153 K. Leung, I. M. B. Nielsen, N. Sai, C. Medforth and J. A. Shelnutz, *J. Phys. Chem. A*, 2010, **114**, 10174–10184.
- 154 J. Shen, M. J. Kolb, A. J. Göttle and M. T. M. Koper, *J. Phys. Chem. C*, 2016, **120**, 15714–15721.
- 155 G. Zhu, Y. Li, H. Zhu, H. Su, S. H. Chan and Q. Sun, *ACS Catal.*, 2016, **6**, 6294–6301.
- 156 N. Sonoyama, M. Kirii and T. Sakata, *Electrochem. Commun.*, 1999, **1**, 213–216.
- 157 Y. Bochlin, E. Korin and A. Bettelheim, *ACS Appl. Energy Mater.*, 2019, **2**(12), 8434–8440.
- 158 M. Zhu, D.-T. Yang, R. Ye, J. Zeng, N. Corbin and K. Manthiram, *Catal. Sci. Technol.*, 2019, **9**, 974–980.
- 159 H. Tanaka and A. Aramata, *J. Electroanal. Chem.*, 1997, **437**, 29–35.
- 160 T. Atoguchi, A. Aramata, A. Kazusaka and M. Enyo, *J. Chem. Soc., Chem. Commun.*, 1991, 156–157, DOI: 10.1039/C39910000156.
- 161 M. Zhu, J. Chen, L. Huang, R. Ye, J. Xu and Y.-F. Han, *Angew. Chem., Int. Ed.*, 2019, **58**, 6595–6599.
- 162 A. N. Marianov and Y. Jiang, *Appl. Catal., B*, 2019, **244**, 881–888.
- 163 D. Quezada, J. Honores, M. García, F. Armijo and M. Isaacs, *New J. Chem.*, 2014, **38**, 3606–3612.
- 164 J. E. Pander III, A. Fogg and A. B. Bocarsly, *ChemCatChem*, 2016, **8**, 3536–3545.
- 165 C. S. Diercks, S. Lin, N. Kornienko, E. A. Kapustin, E. M. Nichols, C. Zhu, Y. Zhao, C. J. Chang and O. M. Yaghi, *J. Am. Chem. Soc.*, 2018, **140**, 1116–1122.
- 166 X.-D. Zhang, S.-Z. Hou, J.-X. Wu and Z.-Y. Gu, *Chem. – Eur. J.*, 2020, **26**, 1604–1611.
- 167 Y.-R. Wang, Q. Huang, C.-T. He, Y. Chen, J. Liu, F.-C. Shen and Y.-Q. Lan, *Nat. Commun.*, 2018, **9**, 4466.
- 168 Y. Guo, W. Shi, H. Yang, Q. He, Z. Zeng, J.-y. Ye, X. He, R. Huang, C. Wang and W. Lin, *J. Am. Chem. Soc.*, 2019, **141**, 17875–17883.
- 169 Q. Wu, R.-K. Xie, M.-J. Mao, G.-L. Chai, J.-D. Yi, S.-S. Zhao, Y.-B. Huang and R. Cao, *ACS Energy Lett.*, 2020, **5**, 1005–1012.
- 170 S. Meshitsuka, M. Ichikawa and K. Tamaru, *J. Chem. Soc., Chem. Commun.*, 1974, 158–159, DOI: 10.1039/C39740000158.
- 171 C. M. Lieber and N. S. Lewis, *J. Am. Chem. Soc.*, 1984, **106**, 5033–5034.
- 172 J. Zhang, W. J. Pietro and A. B. P. Lever, *J. Electroanal. Chem.*, 1996, **403**, 93–100.
- 173 T. Abe, F. Taguchi, T. Yoshida, S. Tokita, G. Schnurpfeil, D. Wöhrle and M. Kaneko, *J. Mol. Catal. A: Chem.*, 1996, **112**, 55–61.
- 174 M. N. Mahmood, D. Masheder and C. J. Harty, *J. Appl. Electrochem.*, 1987, **17**, 1223–1227.
- 175 N. Furuya and K. Matsui, *J. Electroanal. Chem. Interfacial Electrochem.*, 1989, **271**, 181–191.
- 176 M. Zhu, R. Ye, K. Jin, N. Lazouski and K. Manthiram, *ACS Energy Lett.*, 2018, **3**, 1381–1386.
- 177 Z. Jiang, Y. Wang, X. Zhang, H. Zheng, X. Wang and Y. Liang, *Nano Res.*, 2019, **12**, 2330–2334.
- 178 J. Choi, P. Wagner, S. Gambhir, R. Jalili, D. R. MacFarlane, G. G. Wallace and D. L. Officer, *ACS Energy Lett.*, 2019, **4**, 666–672.
- 179 N. Han, Y. Wang, L. Ma, J. Wen, J. Li, H. Zheng, K. Nie, X. Wang, F. Zhao, Y. Li, J. Fan, J. Zhong, T. Wu, D. J. Miller, J. Lu, S.-T. Lee and Y. Li, *Chem*, 2017, **3**, 652–664.
- 180 J. Chen, J. Li, W. Liu, X. Ma, J. Xu, M. Zhu and Y.-F. Han, *Green Chem.*, 2019, **21**, 6056–6061.
- 181 H. Wu, M. Zeng, X. Zhu, C. Tian, B. Mei, Y. Song, X.-L. Du, Z. Jiang, L. He, C. Xia and S. Dai, *ChemElectroChem*, 2018, **5**, 2717–2721.
- 182 M. Isaacs, F. Armijo, G. Ramírez, E. Trollund, S. R. Biaggio, J. Costamagna and M. J. Aguirre, *J. Mol. Catal. A: Chem.*, 2005, **229**, 249–257.
- 183 N. Morlanés, K. Takanabe and V. Rodionov, *ACS Catal.*, 2016, **6**, 3092–3095.
- 184 X. Zhang, Z. Wu, X. Zhang, L. Li, Y. Li, H. Xu, X. Li, X. Yu, Z. Zhang, Y. Liang and H. Wang, *Nat. Commun.*, 2017, **8**, 14675.
- 185 X. Lu, Y. Wu, X. Yuan, L. Huang, Z. Wu, J. Xuan, Y. Wang and H. Wang, *ACS Energy Lett.*, 2018, **3**, 2527–2532.
- 186 M. Wang, K. Torbensen, D. Salvatore, S. Ren, D. Joulié, F. Dumoulin, D. Mendoza, B. Lassalle-Kaiser, U. İsci, C. P. Berlinguette and M. Robert, *Nat. Commun.*, 2019, **10**, 3602.
- 187 S. Ren, D. Joulié, D. Salvatore, K. Torbensen, M. Wang, M. Robert and C. P. Berlinguette, *Science*, 2019, **365**, 367–369.
- 188 R. B. Kutz, Q. Chen, H. Yang, S. D. Sajjad, Z. Liu and I. R. Masel, *Energy Technol.*, 2017, **5**, 929–936.
- 189 Y. Y. Birdja and M. T. M. Koper, *J. Am. Chem. Soc.*, 2017, **139**, 2030–2034.
- 190 T. Yoshida, K. Kamato, M. Tsukamoto, T. Iida, D. Schlettwein, D. Wöhrle and M. Kaneko, *J. Electroanal. Chem.*, 1995, **385**, 209–225.
- 191 T. Abe, T. Yoshida, S. Tokita, F. Taguchi, H. Imaya and M. Kaneko, *J. Electroanal. Chem.*, 1996, **412**, 125–132.
- 192 W. W. Kramer and C. C. L. McCrory, *Chem. Sci.*, 2016, **7**, 2506–2515.
- 193 M. Zhu, J. Chen, R. Guo, J. Xu, X. Fang and Y.-F. Han, *Appl. Catal., B*, 2019, **251**, 112–118.
- 194 Y. Liu and C. C. L. McCrory, *Nat. Commun.*, 2019, **10**, 1683.
- 195 J. Wang, X. Huang, S. Xi, J.-M. Lee, C. Wang, Y. Du and X. Wang, *Angew. Chem., Int. Ed.*, 2019, **58**, 13532–13539.
- 196 R. Matheu, E. Gutierrez-Puebla, M. Á. Monge, C. S. Diercks, J. Kang, M. S. Prévot, X. Pei, N. Hanikel, B. Zhang, P. Yang and O. M. Yaghi, *J. Am. Chem. Soc.*, 2019, **141**, 17081–17085.
- 197 J. Y. Becker, B. Vainas, R. Eger and L. Kaufman, *J. Chem. Soc., Chem. Commun.*, 1985, 1471–1472, DOI: 10.1039/C39850001471.
- 198 Y. Y. Birdja, J. Shen and M. T. M. Koper, *Catal. Today*, 2017, **288**, 37–47.



- 199 A. J. Göttle and M. T. M. Koper, *J. Am. Chem. Soc.*, 2018, **140**, 4826–4834.
- 200 Z. Weng, J. Jiang, Y. Wu, Z. Wu, X. Guo, K. L. Materna, W. Liu, V. S. Batista, G. W. Brudvig and H. Wang, *J. Am. Chem. Soc.*, 2016, **138**, 8076–8079.
- 201 Y. Wu, J. Jiang, Z. Weng, M. Wang, D. L. J. Broere, Y. Zhong, G. W. Brudvig, Z. Feng and H. Wang, *ACS Cent. Sci.*, 2017, **3**, 847–852.
- 202 J. Jiang, A. J. Matula, J. R. Swierk, N. Romano, Y. Wu, V. S. Batista, R. H. Crabtree, J. S. Lindsey, H. Wang and G. W. Brudvig, *ACS Catal.*, 2018, **8**, 10131–10136.
- 203 Y. Y. Birdja, R. E. Vos, T. A. Wezendonk, L. Jiang, F. Kapteijn and M. T. M. Koper, *ACS Catal.*, 2018, **8**, 4420–4428.
- 204 Z. Zhang, J. Xiao, X.-J. Chen, S. Yu, L. Yu, R. Si, Y. Wang, S. Wang, X. Meng, Y. Wang, Z.-Q. Tian and D. Deng, *Angew. Chem., Int. Ed.*, 2018, **57**, 16339–16342.
- 205 Z. Weng, Y. Wu, M. Wang, J. Jiang, K. Yang, S. Huo, X.-F. Wang, Q. Ma, G. W. Brudvig, V. S. Batista, Y. Liang, Z. Feng and H. Wang, *Nat. Commun.*, 2018, **9**, 415.
- 206 D. Karapinar, A. Zitolo, T. N. Huan, S. Zanna, D. Taverna, L. H. Galvão Tizei, D. Giaume, P. Marcus, V. Mougél and M. Fontecave, *ChemSusChem*, 2020, **13**, 173–179.
- 207 D.-D. Ma, S.-G. Han, C. Cao, X. Li, X.-T. Wu and Q.-L. Zhu, *Appl. Catal., B*, 2020, **264**, 118530.
- 208 B. J. Fisher and R. Eisenberg, *J. Am. Chem. Soc.*, 1980, **102**, 7361–7363.
- 209 M. Beley, J.-P. Collin, R. Ruppert and J.-P. Sauvage, *J. Chem. Soc., Chem. Commun.*, 1984, 1315–1316, DOI: 10.1039/C39840001315.
- 210 M. Beley, J. P. Collin, R. Ruppert and J. P. Sauvage, *J. Am. Chem. Soc.*, 1986, **108**, 7461–7467.
- 211 J. P. Collin, A. Jouaiti and J. P. Sauvage, *Inorg. Chem.*, 1988, **27**, 1986–1990.
- 212 G. B. Balazs and F. C. Anson, *J. Electroanal. Chem.*, 1992, **322**, 325–345.
- 213 J. D. Froehlich and C. P. Kubiak, *Inorg. Chem.*, 2012, **51**, 3932–3934.
- 214 C. A. Kelly, Q. G. Mulazzani, M. Venturi, E. L. Blinn and M. A. J. Rodgers, *J. Am. Chem. Soc.*, 1995, **117**, 4911–4919.
- 215 J. Song, E. L. Klein, F. Neese and S. Ye, *Inorg. Chem.*, 2014, **53**, 7500–7507.
- 216 E. Fujita, J. Haff, R. Sanzenbacher and H. Elias, *Inorg. Chem.*, 1994, **33**, 4627–4628.
- 217 J. D. Froehlich and C. P. Kubiak, *J. Am. Chem. Soc.*, 2015, **137**, 3565–3573.
- 218 M. Fujihira, Y. Hirata and K. Suga, *J. Electroanal. Chem. Interfacial Electrochem.*, 1990, **292**, 199–215.
- 219 L. R. Furenliid, M. W. Renner, D. J. Szalda and E. Fujita, *J. Am. Chem. Soc.*, 1991, **113**, 883–892.
- 220 D. A. Gangi and R. R. Durand, *J. Chem. Soc., Chem. Commun.*, 1986, 697–699, DOI: 10.1039/C39860000697.
- 221 I. Zilbermann, M. Winnik, D. Sagiv, A. Rotman, H. Cohen and D. Meyerstein, *Inorg. Chim. Acta*, 1995, **240**, 503–514.
- 222 K. Bujno, R. Bilewicz, L. Siegfried and T. A. Kaden, *J. Electroanal. Chem.*, 1998, **445**, 47–53.
- 223 E. Kimura, M. Haruta, T. Koike, M. Shionoya, K. Takenouchi and Y. Iitaka, *Inorg. Chem.*, 1993, **32**, 2779–2784.
- 224 P. J. Connolly and E. J. Billo, *Inorg. Chem.*, 1987, **26**, 3224–3226.
- 225 J. Schneider, H. Jia, K. Kobihiro, D. E. Cabelli, J. T. Muckerman and E. Fujita, *Energy Environ. Sci.*, 2012, **5**, 9502–9510.
- 226 Y. Wu, B. Rudshiteyn, A. Zhanaidarova, J. D. Froehlich, W. Ding, C. P. Kubiak and V. S. Batista, *ACS Catal.*, 2017, **7**, 5282–5288.
- 227 C. de Alwis, J. A. Crayston, T. Cromie, T. Eisenblätter, R. W. Hay, Y. D. Lampeka and L. V. Tsymbal, *Electrochim. Acta*, 2000, **45**, 2061–2074.
- 228 E. Y. Lee, D. Hong, H. W. Park and M. P. Suh, *Eur. J. Inorg. Chem.*, 2003, 3242–3249.
- 229 L.-M. Cao, H.-H. Huang, J.-W. Wang, D.-C. Zhong and T.-B. Lu, *Green Chem.*, 2018, **20**, 798–803.
- 230 E. M. Nichols and C. J. Chang, *Organometallics*, 2019, **38**, 1213–1218.
- 231 C. R. Schneider, L. C. Lewis and H. S. Shafaat, *Dalton Trans.*, 2019, **48**, 15810–15821.
- 232 J. Honores, D. Quezada, M. García, K. Calfumán, J. P. Mueña, M. J. Aguirre, M. C. Arévalo and M. Isaacs, *Green Chem.*, 2017, **19**, 1155–1162.
- 233 A. Zhanaidarova, C. E. Moore, M. Gembicky and C. P. Kubiak, *Chem. Commun.*, 2018, **54**, 4116–4119.
- 234 G. Neri, J. J. Walsh, C. Wilson, A. Reynal, J. Y. C. Lim, X. Li, A. J. P. White, N. J. Long, J. R. Durrant and A. J. Cowan, *Phys. Chem. Chem. Phys.*, 2015, **17**, 1562–1566.
- 235 D. Saravanakumar, J. Song, N. Jung, H. Jirimali and W. Shin, *ChemSusChem*, 2012, **5**, 634–636.
- 236 C. R. Schneider and H. S. Shafaat, *Chem. Commun.*, 2016, **52**, 9889–9892.
- 237 C. Jiang, A. W. Nichols, J. F. Walzer and C. W. Machan, *Inorg. Chem.*, 2020, **59**, 1883–1892.
- 238 N. Sutin, C. Creutz and E. Fujita, *Comments Inorg. Chem.*, 1997, **19**, 67–92.
- 239 T. Ogata, Y. Yamamoto, Y. Wada, K. Murakoshi, M. Kusaba, N. Nakashima, A. Ishida, S. Takamuku and S. Yanagida, *J. Phys. Chem.*, 1995, **99**, 11916–11922.
- 240 A. H. A. Tinnemans, T. P. M. Koster, D. H. M. W. Thewissen and A. Mackor, *Recl. Trav. Chim. Pays-Bas*, 1984, **103**, 288–295.
- 241 C. Creutz, H. A. Schwarz, J. F. Wishart, E. Fujita and N. Sutin, *J. Am. Chem. Soc.*, 1991, **113**, 3361–3371.
- 242 E. Fujita, C. Creutz, N. Sutin and D. J. Szalda, *J. Am. Chem. Soc.*, 1991, **113**, 343–353.
- 243 E. Fujita, D. J. Szalda, C. Creutz and N. Sutin, *J. Am. Chem. Soc.*, 1988, **110**, 4870–4871.
- 244 T. Ogata, S. Yanagida, B. S. Brunenschwig and E. Fujita, *J. Am. Chem. Soc.*, 1995, **117**, 6708–6716.
- 245 E. Fujita, C. Creutz, N. Sutin and B. S. Brunenschwig, *Inorg. Chem.*, 1993, **32**, 2657–2662.
- 246 E. Fujita, L. R. Furenliid and M. W. Renner, *J. Am. Chem. Soc.*, 1997, **119**, 4549–4550.
- 247 M. H. Schmidt, G. M. Miskelly and N. S. Lewis, *J. Am. Chem. Soc.*, 1990, **112**, 3420–3426.



- 248 D. J. Szalda, E. Fujita and C. Creutz, *Inorg. Chem.*, 1989, **28**, 1446–1450.
- 249 E. Fujita and D. J. Szalda, *Inorg. Chim. Acta*, 2000, **297**, 139–144.
- 250 C.-M. Che, S.-T. Mak, W.-O. Lee, K.-W. Fung and T. C. W. Mak, *J. Chem. Soc., Dalton Trans.*, 1988, 2153–2159, DOI: 10.1039/DT9880002153.
- 251 D. C. Lacy, C. C. L. McCrory and J. C. Peters, *Inorg. Chem.*, 2014, **53**, 4980–4988.
- 252 C. C. L. McCrory, C. Uyeda and J. C. Peters, *J. Am. Chem. Soc.*, 2012, **134**, 3164–3170.
- 253 S. Varma, C. E. Castillo, T. Stoll, J. Fortage, A. G. Blackman, F. Molton, A. Deronzier and M.-N. Collomb, *Phys. Chem. Chem. Phys.*, 2013, **15**, 17544–17552.
- 254 M. Ghosh, T. Weyhermüller and K. Wieghardt, *Dalton Trans.*, 2010, **39**, 1996–2007.
- 255 M. Zhang, M. El-Roz, H. Frei, J. L. Mendoza-Cortes, M. Head-Gordon, D. C. Lacy and J. C. Peters, *J. Phys. Chem. C*, 2015, **119**, 4645–4654.
- 256 H. Sheng and H. Frei, *J. Am. Chem. Soc.*, 2016, **138**, 9959–9967.
- 257 A. Chapovetsky, M. Welborn, J. M. Luna, R. Haiges, T. F. Miller and S. C. Marinescu, *ACS Cent. Sci.*, 2018, **4**, 397–404.
- 258 X. Su, K. M. McCardle, J. A. Panetier and J. W. Jurss, *Chem. Commun.*, 2018, **54**, 3351–3354.
- 259 X. Su, K. M. McCardle, L. Chen, J. A. Panetier and J. W. Jurss, *ACS Catal.*, 2019, **9**, 7398–7408.
- 260 L. Chen, Z. Guo, X.-G. Wei, C. Gallenkamp, J. Bonin, E. Anxolabéhère-Mallart, K.-C. Lau, T.-C. Lau and M. Robert, *J. Am. Chem. Soc.*, 2015, **137**, 10918–10921.
- 261 J.-W. Wang, H.-H. Huang, J.-K. Sun, D.-C. Zhong and T.-B. Lu, *ACS Catal.*, 2018, **8**, 7612–7620.
- 262 A. Taheri, C. R. Carr and L. A. Berben, *ACS Catal.*, 2018, **8**, 5787–5793.
- 263 N. D. Loewen, E. J. Thompson, M. Kagan, C. L. Banales, T. W. Myers, J. C. Fettinger and L. A. Berben, *Chem. Sci.*, 2016, **7**, 2728–2735.
- 264 A. W. Nichols, S. Chatterjee, M. Sabat and C. W. Machan, *Inorg. Chem.*, 2018, **57**, 2111–2121.
- 265 A. W. Nichols, S. L. Hooe, J. S. Kuehner, D. A. Dickie and C. W. Machan, *Inorg. Chem.*, 2020, **59**, 5854–5864.
- 266 S.-N. Pun, W.-H. Chung, K.-M. Lam, P. Guo, P.-H. Chan, K.-Y. Wong, C.-M. Che, T.-Y. Chen and S.-M. Peng, *J. Chem. Soc., Dalton Trans.*, 2002, 575–583, DOI: 10.1039/B108472K.
- 267 D. Z. Zee, M. Nippe, A. E. King, C. J. Chang and J. R. Long, *Inorg. Chem.*, 2020, **59**, 5206–5217.
- 268 F. Franco, C. Cometto, F. Ferrero Vallana, F. Sordello, E. Priola, C. Minero, C. Nervi and R. Gobetto, *Chem. Commun.*, 2014, **50**, 14670–14673.
- 269 F. Franco, C. Cometto, L. Nencini, C. Barolo, F. Sordello, C. Minero, J. Fiedler, M. Robert, R. Gobetto and C. Nervi, *Chem. – Eur. J.*, 2017, **23**, 4782–4793.
- 270 I. Fokin, A. Denisiuk, C. Würtele and I. Siewert, *Inorg. Chem.*, 2019, **58**, 10444–10453.
- 271 M. H. Rønne, D. Cho, M. R. Madsen, J. B. Jakobsen, S. Eom, É. Escoudé, H. C. D. Hammershøj, D. U. Nielsen, S. U. Pedersen, M.-H. Baik, T. Skrydstrup and K. Daasbjerg, *J. Am. Chem. Soc.*, 2020, **142**, 4265–4275.
- 272 E. A. Mohamed, Z. N. Zahran, Y. Tsubonouchi, K. Saito, T. Yui and M. Yagi, *ACS Appl. Energy Mater.*, 2020, **3**, 4114–4120.
- 273 F. Wang, B. Cao, W.-P. To, C.-W. Tse, K. Li, X.-Y. Chang, C. Zang, S. L.-F. Chan and C.-M. Che, *Catal. Sci. Technol.*, 2016, **6**, 7408–7420.
- 274 J.-W. Wang, H.-H. Huang, J.-K. Sun, T. Ouyang, D.-C. Zhong and T.-B. Lu, *ChemSusChem*, 2018, **11**, 1025–1031.
- 275 N. Elgrishi, M. B. Chambers and M. Fontecave, *Chem. Sci.*, 2015, **6**, 2522–2531.
- 276 T. Shimoda, T. Morishima, K. Kodama, T. Hirose, D. E. Polyansky, G. F. Manbeck, J. T. Muckerman and E. Fujita, *Inorg. Chem.*, 2018, **57**, 5486–5498.
- 277 S. Fernández, F. Franco, C. Casadevall, V. Martin-Diaconescu, J. M. Luis and J. Lloret-Fillol, *J. Am. Chem. Soc.*, 2020, **142**, 120–133.
- 278 S. L.-F. Chan, T. L. Lam, C. Yang, S.-C. Yan and N. M. Cheng, *Chem. Commun.*, 2015, **51**, 7799–7801.
- 279 T. Ouyang, H.-H. Huang, J.-W. Wang, D.-C. Zhong and T.-B. Lu, *Angew. Chem., Int. Ed.*, 2017, **56**, 738–743.
- 280 D. He, T. Jin, W. Li, S. Pantovich, D. Wang and G. Li, *Chem. – Eur. J.*, 2016, **22**, 13064–13067.
- 281 C. Cometto, L. Chen, P.-K. Lo, Z. Guo, K.-C. Lau, E. Anxolabéhère-Mallart, C. Fave, T.-C. Lau and M. Robert, *ACS Catal.*, 2018, **8**, 3411–3417.
- 282 Z. Guo, S. Cheng, C. Cometto, E. Anxolabéhère-Mallart, S.-M. Ng, C.-C. Ko, G. Liu, L. Chen, M. Robert and T.-C. Lau, *J. Am. Chem. Soc.*, 2016, **138**, 9413–9416.
- 283 C. Cometto, R. Kuriki, L. Chen, K. Maeda, T.-C. Lau, O. Ishitani and M. Robert, *J. Am. Chem. Soc.*, 2018, **140**, 7437–7440.
- 284 C. Cometto, L. Chen, E. Anxolabéhère-Mallart, C. Fave, T.-C. Lau and M. Robert, *Organometallics*, 2019, **38**, 1280–1285.
- 285 K.-M. Lam, K.-Y. Wong, S.-M. Yang and C.-M. Che, *J. Chem. Soc., Dalton Trans.*, 1995, 1103–1107, DOI: 10.1039/DT9950001103.
- 286 W. Nie and C. C. L. McCrory, *Chem. Commun.*, 2018, **54**, 1579–1582.
- 287 M. Wang, L. Chen, T.-C. Lau and M. Robert, *Angew. Chem., Int. Ed.*, 2018, **57**, 7769–7773.
- 288 W. Nie, Y. Wang, T. Zheng, A. Ibrahim, Z. Xu and C. C. L. McCrory, *ACS Catal.*, 2020, **10**, 4942–4959.
- 289 M. D. Sampson and C. P. Kubiak, *J. Am. Chem. Soc.*, 2016, **138**, 1386–1393.
- 290 J. W. Raebiger, J. W. Turner, B. C. Noll, C. J. Curtis, A. Miedaner, B. Cox and D. L. DuBois, *Organometallics*, 2006, **25**, 3345–3351.
- 291 K.-Y. Wong, W.-H. Chung and C.-P. Lau, *J. Electroanal. Chem.*, 1998, **453**, 161–170.
- 292 J. M. Smieja, M. D. Sampson, K. A. Grice, E. E. Benson, J. D. Froehlich and C. P. Kubiak, *Inorg. Chem.*, 2013, **52**, 2484–2491.
- 293 Z. Chen, C. Chen, D. R. Weinberg, P. Kang, J. J. Concepcion, D. P. Harrison, M. S. Brookhart and T. J. Meyer, *Chem. Commun.*, 2011, **47**, 12607–12609.



- 294 H. Xu, D. Cheng, D. Cao and X. C. Zeng, *Nat. Catal.*, 2018, **1**, 339–348.
- 295 A. S. Varela, W. Ju and P. Strasser, *Adv. Energy Mater.*, 2018, **8**, 1703614.
- 296 F. Pan, H. Zhang, Z. Liu, D. Cullen, K. Liu, K. More, G. Wu, G. Wang and Y. Li, *J. Mater. Chem. A*, 2019, **7**, 26231–26237.
- 297 F. Pan, H. Zhang, K. Liu, D. Cullen, K. More, M. Wang, Z. Feng, G. Wang, G. Wu and Y. Li, *ACS Catal.*, 2018, **8**, 3116–3122.
- 298 T. N. Huan, N. Ranjbar, G. Rouse, M. Sougrati, A. Zitolo, V. Mougél, F. Jaouen and M. Fontecave, *ACS Catal.*, 2017, **7**, 1520–1525.
- 299 Y. Hori and A. Murata, *Electrochim. Acta*, 1990, **35**, 1777–1780.
- 300 O. Koga and Y. Hori, *Electrochim. Acta*, 1993, **38**, 1391–1394.
- 301 A. Bagger, W. Ju, A. S. Varela, P. Strasser and J. Rossmeisl, *Catal. Today*, 2017, **288**, 74–78.
- 302 A. S. Varela, W. Ju, A. Bagger, P. Franco, J. Rossmeisl and P. Strasser, *ACS Catal.*, 2019, **9**, 7270–7284.
- 303 A. Li, S. A. Nicolae, M. Qiao, K. Preuss, P. A. Szilágyi, A. Moores and M. M. Titirici, *ChemCatChem*, 2019, **11**, 3602–3625.
- 304 W. Yang, S. Xu, K. Ma, C. Wu, I. D. Gates, X. Ding, W. Meng and Z. Gao, *Nano Mater. Sci.*, 2020, **2**, 120–131.
- 305 J. Tuo, Y. Zhu, L. Cheng, Y. Li, X. Yang, J. Shen and C. Li, *ChemSusChem*, 2019, **12**, 2644–2650.
- 306 J. Li, P. Pršlja, T. Shinagawa, A. J. Martín Fernández, F. Krumeich, K. Artyushkova, P. Atanassov, A. Zitolo, Y. Zhou, R. García-Muelas, N. López, J. Pérez-Ramírez and F. Jaouen, *ACS Catal.*, 2019, **9**, 10426–10439.
- 307 S. Zhao, G. Chen, G. Zhou, L. C. Yin, J. P. Veder, B. Johannessen, M. Saunders, S. Z. Yang, R. De Marco, C. Liu and S. P. Jiang, *Adv. Funct. Mater.*, 2020, **30**, 1906157.
- 308 C.-Z. Yuan, K. Liang, X.-M. Xia, Z. K. Yang, Y.-F. Jiang, T. Zhao, C. Lin, T.-Y. Cheang, S.-L. Zhong and A.-W. Xu, *Catal. Sci. Technol.*, 2019, **9**, 3669–3674.
- 309 P. Lu, Y. Yang, J. Yao, M. Wang, S. Dipazir, M. Yuan, J. Zhang, X. Wang, Z. Xie and G. Zhang, *Appl. Catal., B*, 2019, **241**, 113–119.
- 310 S. Ma, P. Su, W. Huang, S. P. Jiang, S. Bai and J. Liu, *ChemCatChem*, 2019, **11**, 6092–6098.
- 311 F. Li, S. Hong, T.-S. Wu, X. Li, J. Masa, Y.-L. Soo and Z. Sun, *ACS Appl. Energy Mater.*, 2019, **2**, 8836–8842.
- 312 X. Li, W. Bi, M. Chen, Y. Sun, H. Ju, W. Yan, J. Zhu, X. Wu, W. Chu, C. Wu and Y. Xie, *J. Am. Chem. Soc.*, 2017, **139**, 14889–14892.
- 313 H. B. Yang, S.-F. Hung, S. Liu, K. Yuan, S. Miao, L. Zhang, X. Huang, H.-Y. Wang, W. Cai, R. Chen, J. Gao, X. Yang, W. Chen, Y. Huang, H. M. Chen, C. M. Li, T. Zhang and B. Liu, *Nat. Energy*, 2018, **3**, 140–147.
- 314 W. Bi, X. Li, R. You, M. Chen, R. Yuan, W. Huang, X. Wu, W. Chu, C. Wu and Y. Xie, *Adv. Mater.*, 2018, **30**, 1706617.
- 315 H. Yang, Q. Lin, C. Zhang, X. Yu, Z. Cheng, G. Li, Q. Hu, X. Ren, Q. Zhang, J. Liu and C. He, *Nat. Commun.*, 2020, **11**, 593.
- 316 H.-Y. Jeong, M. Balamurugan, V. S. K. Choutipalli, J. Jo, H. Baik, V. Subramanian, M. Kim, U. Sim and K. T. Nam, *Chem. – Eur. J.*, 2018, **24**, 18444–18454.
- 317 S. Liu, H. B. Yang, S.-F. Hung, J. Ding, W. Cai, L. Liu, J. Gao, X. Li, X. Ren, Z. Kuang, Y. Huang, T. Zhang and B. Liu, *Angew. Chem., Int. Ed.*, 2020, **59**, 798–803.
- 318 K. Jiang, S. Siahrostami, T. Zheng, Y. Hu, S. Hwang, E. Stavitski, Y. Peng, J. Dynes, M. Gangisetty, D. Su, K. Attenkofer and H. Wang, *Energy Environ. Sci.*, 2018, **11**, 893–903.
- 319 Y.-N. Gong, L. Jiao, Y. Qian, C.-Y. Pan, L. Zheng, X. Cai, B. Liu, S.-H. Yu and H.-L. Jiang, *Angew. Chem., Int. Ed.*, 2020, **59**, 2705–2709.
- 320 Z.-L. Wang, J. Choi, M. Xu, X. Hao, H. Zhang, Z. Jiang, M. Zuo, J. Kim, W. Zhou, X. Meng, Q. Yu, Z. Sun, S. Wei, J. Ye, G. G. Wallace, D. L. Officer and Y. Yamauchi, *ChemSusChem*, 2020, **13**, 929–937.
- 321 H. J. Freund and M. W. Roberts, *Surf. Sci. Rep.*, 1996, **25**, 225–273.
- 322 X. Zhao and Y. Liu, *J. Am. Chem. Soc.*, 2020, **142**, 5773–5777.
- 323 K. Mou, Z. Chen, X. Zhang, M. Jiao, X. Zhang, X. Ge, W. Zhang and L. Liu, *Small*, 2019, **15**, e1903668.
- 324 C. Yan, H. Li, Y. Ye, H. Wu, F. Cai, R. Si, J. Xiao, S. Miao, S. Xie, F. Yang, Y. Li, G. Wang and X. Bao, *Energy Environ. Sci.*, 2018, **11**, 1204–1210.
- 325 K. Mou, Z. Chen, X. Zhang, M. Jiao, X. Zhang, X. Ge, W. Zhang and L. Liu, *Small*, 2019, **15**, 1903668.
- 326 Q. Fan, P. Hou, C. Choi, T. S. Wu, S. Hong, F. Li, Y. L. Soo, P. Kang, Y. Jung and Z. Sun, *Adv. Energy Mater.*, 2020, **10**, 1903068.
- 327 P. Su, K. Iwase, T. Harada, K. Kamiya and S. Nakanishi, *Chem. Sci.*, 2018, **9**, 3941–3947.
- 328 C. Arana, S. Yan, M. Keshavarz-K, K. T. Potts and H. D. Abruna, *Inorg. Chem.*, 1992, **31**, 3680–3682.
- 329 C. Arana, M. Keshavarz, K. T. Potts and H. D. Abruña, *Inorg. Chim. Acta*, 1994, **225**, 285–295.
- 330 N. Elgrishi, M. B. Chambers, V. Artero and M. Fontecave, *Phys. Chem. Chem. Phys.*, 2014, **16**, 13635–13644.
- 331 J. Yang, Z. Qiu, C. Zhao, W. Wei, W. Chen, Z. Li, Y. Qu, J. Dong, J. Luo, Z. Li and Y. Wu, *Angew. Chem., Int. Ed.*, 2018, **57**, 14095–14100.
- 332 Y. Cheng, S. Zhao, H. Li, S. He, J.-P. Veder, B. Johannessen, J. Xiao, S. Lu, J. Pan, M. F. Chisholm, S.-Z. Yang, C. Liu, J. G. Chen and S. P. Jiang, *Appl. Catal., B*, 2019, **243**, 294–303.
- 333 Y. Zheng, J. Han, L. Takele, F. Xie, Y. Zhang, J. Sun, B. Han, J. Chen, Y. Gao and Z. Tang, *Inorg. Chem. Front.*, 2019, **6**, 1729–1734.
- 334 T. Möller, W. Ju, A. Bagger, X. Wang, F. Luo, T. Ngo Thanh, A. S. Varela, J. Rossmeisl and P. Strasser, *Energy Environ. Sci.*, 2019, **12**, 640–647.
- 335 H.-Y. Jeong, M. Balamurugan, V. S. K. Choutipalli, E.-s. Jeong, V. Subramanian, U. Sim and K. T. Nam, *J. Mater. Chem. A*, 2019, **7**, 10651–10661.
- 336 T. Zheng, K. Jiang, N. Ta, Y. Hu, J. Zeng, J. Liu and H. Wang, *Joule*, 2019, **3**, 265–278.
- 337 F. Pan, W. Deng, C. Justiniano and Y. Li, *Appl. Catal., B*, 2018, **226**, 463–472.
- 338 X.-M. Hu, H. H. Hval, E. T. Bjerglund, K. J. Dalgaard, M. R. Madsen, M.-M. Pohl, E. Welter, P. Lamagni,



- K. B. Buhl, M. Bremholm, M. Beller, S. U. Pedersen, T. Skrydstrup and K. Daasbjerg, *ACS Catal.*, 2018, **8**, 6255–6264.
- 339 X. Qin, S. Zhu, F. Xiao, L. Zhang and M. Shao, *ACS Energy Lett.*, 2019, **4**, 1778–1783.
- 340 J. Gu, C.-S. Hsu, L. Bai, H. M. Chen and X. Hu, *Science*, 2019, **364**, 1091.
- 341 M. N. Jackson, C. J. Kaminsky, S. Oh, J. F. Melville and Y. Surendranath, *J. Am. Chem. Soc.*, 2019, **141**, 14160–14167.
- 342 M. N. Jackson and Y. Surendranath, *Acc. Chem. Res.*, 2019, **52**, 3432–3441.
- 343 C. Zhang, S. Yang, J. Wu, M. Liu, S. Yazdi, M. Ren, J. Sha, J. Zhong, K. Nie, A. S. Jalilov, Z. Li, H. Li, B. I. Yakobson, Q. Wu, E. Ringe, H. Xu, P. M. Ajayan and J. M. Tour, *Adv. Energy Mater.*, 2018, **8**, 1703487.
- 344 H. Zhang, J. Li, S. Xi, Y. Du, X. Hai, J. Wang, H. Xu, G. Wu, J. Zhang, J. Lu and J. Wang, *Angew. Chem., Int. Ed.*, 2019, **58**, 14871–14876.
- 345 H.-J. Yang, J. Dong, Y.-H. Hong, W.-F. Lin, Z.-Y. Zhou and S.-G. Sun, *Electrochem. Commun.*, 2018, **97**, 82–86.
- 346 C. Zhang, S. Yang, J. Wu, M. Liu, S. Yazdi, M. Ren, J. Sha, J. Zhong, K. Nie, A. S. Jalilov, Z. Li, H. Li, B. I. Yakobson, Q. Wu, E. Ringe, H. Xu, P. M. Ajayan and J. M. Tour, *Adv. Energy Mater.*, 2018, **8**, 1703487.
- 347 Q. Cheng, K. Mao, L. Ma, L. Yang, L. Zou, Z. Zou, Z. Hu and H. Yang, *ACS Energy Lett.*, 2018, **3**, 1205–1211.
- 348 S. Gonell, M. D. Massey, I. P. Moseley, C. K. Schauer, J. T. Muckerman and A. J. M. Miller, *J. Am. Chem. Soc.*, 2019, **141**, 6658–6671.
- 349 A. S. Varela, M. Kroschel, N. D. Leonard, W. Ju, J. Steinberg, A. Bagger, J. Rossmeisl and P. Strasser, *ACS Energy Lett.*, 2018, **3**, 812–817.
- 350 L. D. Chen, M. Urushihara, K. Chan and J. K. Nørskov, *ACS Catal.*, 2016, **6**, 7133–7139.
- 351 A. Zhanaidarova, H. Steger, M. H. Reineke and C. P. Kubiak, *Dalton Trans.*, 2017, **46**, 12413–12416.
- 352 S. Sato, K. Saita, K. Sekizawa, S. Maeda and T. Morikawa, *ACS Catal.*, 2018, **8**, 4452–4458.
- 353 A. J. Göttle and M. T. M. Koper, *Chem. Sci.*, 2017, **8**, 458–465.
- 354 N. Leonard, W. Ju, I. Sinev, J. Steinberg, F. Luo, A. S. Varela, B. Roldan Cuenya and P. Strasser, *Chem. Sci.*, 2018, **9**, 5064–5073.
- 355 H. Rao, L. C. Schmidt, J. Bonin and M. Robert, *Nature*, 2017, **548**, 74–77.
- 356 C. Cometto, L. Chen, D. Mendoza, B. Lassalle-Kaiser, T.-C. Lau and M. Robert, *ChemSusChem*, 2019, **12**, 4500–4505.
- 357 W. Ju, A. Bagger, X. Wang, Y. Tsai, F. Luo, T. Möller, H. Wang, J. Rossmeisl, A. S. Varela and P. Strasser, *ACS Energy Lett.*, 2019, **4**, 1663–1671.
- 358 W. Ju, A. Bagger, G.-P. Hao, A. S. Varela, I. Sinev, V. Bon, B. Roldan Cuenya, S. Kaskel, J. Rossmeisl and P. Strasser, *Nat. Commun.*, 2017, **8**, 944.
- 359 X. Wang, Z. Chen, X. Zhao, T. Yao, W. Chen, R. You, C. Zhao, G. Wu, J. Wang, W. Huang, J. Yang, X. Hong, S. Wei, Y. Wu and Y. Li, *Angew. Chem., Int. Ed.*, 2018, **57**, 1944–1948.
- 360 Y. Pan, R. Lin, Y. Chen, S. Liu, W. Zhu, X. Cao, W. Chen, K. Wu, W. C. Cheong, Y. Wang, L. Zheng, J. Luo, Y. Lin, Y. Liu, C. Liu, J. Li, Q. Lu, X. Chen, D. Wang, Q. Peng, C. Chen and Y. Li, *J. Am. Chem. Soc.*, 2018, **140**, 4218–4221.
- 361 Y. Pan, R. Lin, Y. Chen, S. Liu, W. Zhu, X. Cao, W. Chen, K. Wu, W.-C. Cheong, Y. Wang, L. Zheng, J. Luo, Y. Lin, Y. Liu, C. Liu, J. Li, Q. Lu, X. Chen, D. Wang, Q. Peng, C. Chen and Y. Li, *J. Am. Chem. Soc.*, 2018, **140**, 4218–4221.
- 362 Z. Geng, Y. Cao, W. Chen, X. Kong, Y. Liu, T. Yao and Y. Lin, *Appl. Catal., B*, 2019, **240**, 234–240.
- 363 M. Bourrez, F. Molton, S. Chardon-Noblat and A. Deronzier, *Angew. Chem., Int. Ed.*, 2011, **50**, 9903–9906.
- 364 M. Stanbury, J.-D. Compain and S. Chardon-Noblat, *Coord. Chem. Rev.*, 2018, **361**, 120–137.
- 365 A. Sinopoli, N. T. La Porte, J. F. Martinez, M. R. Wasielewski and M. Sohail, *Coord. Chem. Rev.*, 2018, **365**, 60–74.
- 366 A. S. Varela, N. Ranjbar Sahraie, J. Steinberg, W. Ju, H. S. Oh and P. Strasser, *Angew. Chem., Int. Ed.*, 2015, **54**, 10758–10762.
- 367 W. Ju, A. Bagger, G. P. Hao, A. S. Varela, I. Sinev, V. Bon, B. Roldan Cuenya, S. Kaskel, J. Rossmeisl and P. Strasser, *Nat. Commun.*, 2017, **8**, 944.
- 368 B. Zhang, J. Zhang, J. Shi, D. Tan, L. Liu, F. Zhang, C. Lu, Z. Su, X. Tan, X. Cheng, B. Han, L. Zheng and J. Zhang, *Nat. Commun.*, 2019, **10**, 2980.
- 369 S. Nitopi, E. Bertheussen, S. B. Scott, X. Liu, A. K. Engstfeld, S. Horch, B. Seger, I. E. L. Stephens, K. Chan, C. Hahn, J. K. Nørskov, T. F. Jaramillo and I. Chorkendorff, *Chem. Rev.*, 2019, **119**(12), 7610–7672.
- 370 Q. Zhu, X. Sun, D. Yang, J. Ma, X. Kang, L. Zheng, J. Zhang, Z. Wu and B. Han, *Nat. Commun.*, 2019, **10**, 3851.
- 371 W. Zheng, J. Yang, H. Chen, Y. Hou, Q. Wang, M. Gu, F. He, Y. Xia, Z. Xia, Z. Li, B. Yang, L. Lei, C. Yuan, Q. He, M. Qiu and X. Feng, *Adv. Funct. Mater.*, 2020, **30**, 1907658.
- 372 H. Won da, H. Shin, J. Koh, J. Chung, H. S. Lee, H. Kim and S. I. Woo, *Angew. Chem., Int. Ed.*, 2016, **55**, 9297–9300.
- 373 F. Yang, P. Song, X. Liu, B. Mei, W. Xing, Z. Jiang, L. Gu and W. Xu, *Angew. Chem., Int. Ed.*, 2018, **57**, 12303–12307.
- 374 Z. Chen, K. Mou, S. Yao and L. Liu, *ChemSusChem*, 2018, **11**, 2944–2952.
- 375 Y. Zhao, J. Liang, C. Wang, J. Ma and G. G. Wallace, *Adv. Energy Mater.*, 2018, **8**, 1702524.
- 376 E. Zhang, T. Wang, K. Yu, J. Liu, W. Chen, A. Li, H. Rong, R. Lin, S. Ji, X. Zheng, Y. Wang, L. Zheng, C. Chen, D. Wang, J. Zhang and Y. Li, *J. Am. Chem. Soc.*, 2019, **141**, 16569–16573.
- 377 T. Bligaard and J. K. Nørskov, *Electrochim. Acta*, 2007, **52**, 5512–5516.
- 378 B. Roldan Cuenya and F. Behafarid, *Surf. Sci. Rep.*, 2015, **70**, 135–187.
- 379 H. Mistry, A. S. Varela, S. Köhl, P. Strasser and B. R. Cuenya, *Nat. Rev. Mater.*, 2016, **1**, 16009.
- 380 Y. Y. Birdja, E. Pérez-Gallent, M. C. Figueiredo, A. J. Göttle, F. Calle-Vallejo and M. T. M. Koper, *Nat. Energy*, 2019, **4**, 732–745.



- 381 K. D. Yang, C. W. Lee, J. H. Jang, T. R. Ha and K. T. Nam, *Nanotechnology*, 2017, **28**, 352001.
- 382 F. Li, D. R. MacFarlane and J. Zhang, *Nanoscale*, 2018, **10**, 6235–6260.
- 383 R. M. Arán-Ais, D. Gao and B. Roldan Cuenya, *Acc. Chem. Res.*, 2018, **51**(11), 2906–2917.
- 384 W. Zhu, R. Michalsky, Ö. Metin, H. Lv, S. Guo, C. J. Wright, X. Sun, A. A. Peterson and S. Sun, *J. Am. Chem. Soc.*, 2013, **135**, 16833–16836.
- 385 H. Mistry, R. Reske, Z. Zeng, Z.-J. Zhao, J. Greeley, P. Strasser and B. Roldan Cuenya, *J. Am. Chem. Soc.*, 2014, **136**, 16473–16476.
- 386 Z. Zhang, M. Chi, G. M. Veith, P. Zhang, D. A. Lutterman, J. Rosenthal, S. H. Overbury, S. Dai and H. Zhu, *ACS Catal.*, 2016, **6**, 6255–6264.
- 387 S. Zhang, P. Kang and T. J. Meyer, *J. Am. Chem. Soc.*, 2014, **136**, 1734–1737.
- 388 C. Kim, H. S. Jeon, T. Eom, M. S. Jee, H. Kim, C. M. Friend, B. K. Min and Y. J. Hwang, *J. Am. Chem. Soc.*, 2015, **137**, 13844–13850.
- 389 H. S. Jeon, I. Sinev, F. Scholten, N. J. Divins, I. Zegkinoglou, L. Pielsticker and B. Roldan Cuenya, *J. Am. Chem. Soc.*, 2018, **140**, 9383–9386.
- 390 A. Dutta, A. Kuzume, M. Rahaman, S. Vesztergom and P. Broekmann, *ACS Catal.*, 2015, **5**, 7498–7502.
- 391 R. Reske, H. Mistry, F. Behafarid, B. Roldan Cuenya and P. Strasser, *J. Am. Chem. Soc.*, 2014, **136**, 6978–6986.
- 392 A. A. Peterson, F. Abild-Pedersen, F. Studt, J. Rossmeisl and J. K. Nørskov, *Energy Environ. Sci.*, 2010, **3**, 1311–1315.
- 393 A. A. Peterson and J. K. Nørskov, *J. Phys. Chem. Lett.*, 2012, **3**, 251–258.
- 394 H. A. Hansen, J. B. Varley, A. A. Peterson and J. K. Nørskov, *J. Phys. Chem. Lett.*, 2013, **4**, 388–392.
- 395 Y. Lum and J. W. Ager, *Nat. Catal.*, 2019, **2**, 86–93.
- 396 D. Ren, J. Fong and B. S. Yeo, *Nat. Commun.*, 2018, **9**, 925.
- 397 K. D. Yang, C. W. Lee, K. Jin, S. W. Im and K. T. Nam, *J. Phys. Chem. Lett.*, 2017, **8**, 538–545.
- 398 C. G. Morales-Guio, E. R. Cave, S. A. Nitopi, J. T. Feaster, L. Wang, K. P. Kuhl, A. Jackson, N. C. Johnson, D. N. Abram, T. Hatsukade, C. Hahn and T. F. Jaramillo, *Nat. Catal.*, 2018, **1**, 764–771.
- 399 H. Mistry, A. S. Varela, C. S. Bonifacio, I. Zegkinoglou, I. Sinev, Y.-W. Choi, K. Kisslinger, E. A. Stach, J. C. Yang, P. Strasser and B. R. Cuenya, *Nat. Commun.*, 2016, **7**, 12123.
- 400 A. Verdager-Casadevall, C. W. Li, T. P. Johansson, S. B. Scott, J. T. McKeown, M. Kumar, I. E. L. Stephens, M. W. Kanan and I. Chorkendorff, *J. Am. Chem. Soc.*, 2015, **137**, 9808–9811.
- 401 K. Manthiram, B. J. Beberwyck and A. P. Alivisatos, *J. Am. Chem. Soc.*, 2014, **136**, 13319–13325.
- 402 D. Gao, H. Zhou, J. Wang, S. Miao, F. Yang, G. Wang, J. Wang and X. Bao, *J. Am. Chem. Soc.*, 2015, **137**, 4288–4291.
- 403 W. Zhu, Y.-J. Zhang, H. Zhang, H. Lv, Q. Li, R. Michalsky, A. A. Peterson and S. Sun, *J. Am. Chem. Soc.*, 2014, **136**, 16132–16135.
- 404 S. Liu, H. Tao, L. Zeng, Q. Liu, Z. Xu, Q. Liu and J.-L. Luo, *J. Am. Chem. Soc.*, 2017, **139**, 2160–2163.
- 405 W. Zhu, S. Kattel, F. Jiao and J. G. Chen, *Adv. Energy Mater.*, 2019, **9**, 1802840.
- 406 H.-E. Lee, K. D. Yang, S. M. Yoon, H.-Y. Ahn, Y. Y. Lee, H. Chang, D. H. Jeong, Y.-S. Lee, M. Y. Kim and K. T. Nam, *ACS Nano*, 2015, **9**, 8384–8393.
- 407 S. Ma, Y. Lan, G. M. J. Perez, S. Moniri and P. J. A. Kenis, *ChemSusChem*, 2014, **7**, 866–874.
- 408 L. Zhang, F. Mao, L. R. Zheng, H. F. Wang, X. H. Yang and H. G. Yang, *ACS Catal.*, 2018, **8**, 11035–11041.
- 409 S. Zhao, Z. Tang, S. Guo, M. Han, C. Zhu, Y. Zhou, L. Bai, J. Gao, H. Huang, Y. Li, Y. Liu and Z. Kang, *ACS Catal.*, 2018, **8**, 188–197.
- 410 C. Rogers, W. S. Perkins, G. Veber, T. E. Williams, R. R. Cloke and F. R. Fischer, *J. Am. Chem. Soc.*, 2017, **139**, 4052–4061.
- 411 D. Gao, Y. Zhang, Z. Zhou, F. Cai, X. Zhao, W. Huang, Y. Li, J. Zhu, P. Liu, F. Yang, G. Wang and X. Bao, *J. Am. Chem. Soc.*, 2017, **139**, 5652–5655.
- 412 Y. T. Guntern, J. R. Pankhurst, J. Vávra, M. Mensi, V. Mantella, P. Schouwink and R. Buonsanti, *Angew. Chem., Int. Ed.*, 2019, **58**, 12632–12639.
- 413 J. A. Trindell, Z. Duan, G. Henkelman and R. M. Crooks, *Chem. Rev.*, 2020, **120**, 814–850.
- 414 Q. Lenne, Y. R. Leroux and C. Lagrost, *ChemElectroChem*, 2020, **7**, 2345–2363.
- 415 D. Ung, I. A. Murphy and B. M. Cossairt, *Dalton Trans.*, 2020, **49**, 4995–5005.
- 416 M. A. Ortuño and N. López, *Catal. Sci. Technol.*, 2019, **9**, 5173–5185.
- 417 D. R. Kauffman, D. Alfonso, C. Matranga, H. Qian and R. Jin, *J. Am. Chem. Soc.*, 2012, **134**, 10237–10243.
- 418 N. Austin, S. Zhao, J. R. McKone, R. Jin and G. Mpourmpakis, *Catal. Sci. Technol.*, 2018, **8**, 3795–3805.
- 419 Z. Wang, L. Wu, K. Sun, T. Chen, Z. Jiang, T. Cheng and W. A. Goddard, *J. Phys. Chem. Lett.*, 2018, **9**, 3057–3061.
- 420 Z. Wang, K. Sun, C. Liang, L. Wu, Z. Niu and J. Gao, *ACS Appl. Energy Mater.*, 2019, **2**, 192–195.
- 421 Y. Fang and J. C. Flake, *J. Am. Chem. Soc.*, 2017, **139**, 3399–3405.
- 422 Z. Cao, S. B. Zacate, X. Sun, J. Liu, E. M. Hale, W. P. Carson, S. B. Tyndall, J. Xu, X. Liu, X. Liu, C. Song, J.-h. Luo, M.-J. Cheng, X. Wen and W. Liu, *Angew. Chem., Int. Ed.*, 2018, **130**, 12857–12861.
- 423 M. Gong, Z. Cao, W. Liu, E. M. Nichols, P. T. Smith, J. S. Derrick, Y.-S. Liu, J. Liu, X. Wen and C. J. Chang, *ACS Cent. Sci.*, 2017, **3**, 1032–1040.
- 424 C. Kim, T. Eom, M. S. Jee, H. Jung, H. Kim, B. K. Min and Y. J. Hwang, *ACS Catal.*, 2017, **7**, 779–785.
- 425 M. Gao, Y. Zhu, Y. Liu, K. Wu, H. Lu, S. Tang, C. Liu, H. Yue, B. Liang and J. Yan, *Chem. Commun.*, 2020, **56**, 7021–7024.
- 426 Y. Zhao, C. Wang, Y. Liu, D. R. MacFarlane and G. G. Wallace, *Adv. Energy Mater.*, 2018, **8**, 1801400.
- 427 J. A. Trindell, J. Clausmeyer and R. M. Crooks, *J. Am. Chem. Soc.*, 2017, **139**, 16161–16167.



- 428 L. Ma, W. Hu, Q. Pan, L. Zou, Z. Zou, K. Wen and H. Yang, *J. CO<sub>2</sub> Util.*, 2019, **34**, 108–114.
- 429 Z. Ma, C. Lian, D. Niu, L. Shi, S. Hu, X. Zhang and H. Liu, *ChemSusChem*, 2019, **12**, 1724–1731.
- 430 P. P. Sharma, J. Wu, R. M. Yadav, M. Liu, C. J. Wright, C. S. Tiwary, B. I. Jakobson, J. Lou, P. M. Ajayan and X.-D. Zhou, *Angew. Chem., Int. Ed.*, 2015, **54**, 13701–13705.
- 431 J. R. Pankhurst, Y. T. Guntern, M. Mensi and R. Buonsanti, *Chem. Sci.*, 2019, **10**, 10356–10365.
- 432 B. A. Rosen, A. Salehi-Khojin, M. R. Thorson, W. Zhu, D. T. Whipple, P. J. A. Kenis and R. I. Masel, *Science*, 2011, **334**, 643–644.
- 433 S.-F. Zhao, M. Horne, A. M. Bond and J. Zhang, *J. Phys. Chem. C*, 2016, **120**, 23989–24001.
- 434 G. P. S. Lau, M. Schreier, D. Vasilyev, R. Scopelliti, M. Grätzel and P. J. Dyson, *J. Am. Chem. Soc.*, 2016, **138**, 7820–7823.
- 435 H.-K. Lim, Y. Kwon, H. S. Kim, J. Jeon, Y.-H. Kim, J.-A. Lim, B.-S. Kim, J. Choi and H. Kim, *ACS Catal.*, 2018, **8**, 2420–2427.
- 436 D. C. Grills, Y. Matsubara, Y. Kuwahara, S. R. Golisz, D. A. Kurtz and B. A. Mello, *J. Phys. Chem. Lett.*, 2014, **5**, 2033–2038.
- 437 M. S. Xie, B. Y. Xia, Y. Li, Y. Yan, Y. Yang, Q. Sun, S. H. Chan, A. Fisher and X. Wang, *Energy Environ. Sci.*, 2016, **9**, 1687–1695.
- 438 Z. Han, R. Kortlever, H.-Y. Chen, J. C. Peters and T. Agapie, *ACS Cent. Sci.*, 2017, **3**, 853–859.
- 439 F. Li, A. Thevenon, A. Rosas-Hernández, Z. Wang, Y. Li, C. M. Gabardo, A. Ozden, C. T. Dinh, J. Li, Y. Wang, J. P. Edwards, Y. Xu, C. McCallum, L. Tao, Z.-Q. Liang, M. Luo, X. Wang, H. Li, C. P. O'Brien, C.-S. Tan, D.-H. Nam, R. Quintero-Bermudez, T.-T. Zhuang, Y. C. Li, Z. Han, R. D. Britt, D. Sinton, T. Agapie, J. C. Peters and E. H. Sargent, *Nature*, 2020, **577**, 509–513.
- 440 V. J. Ovalle and M. M. Waegle, *J. Phys. Chem. C*, 2019, **123**, 24453–24460.
- 441 A. Thevenon, A. Rosas-Hernández, J. C. Peters and T. Agapie, *Angew. Chem., Int. Ed.*, 2019, **58**, 16952–16958.
- 442 S. Zhong, X. Yang, Z. Cao, X. Dong, S. M. Kozlov, L. Falivene, J.-K. Huang, X. Zhou, M. N. Hedhili, Z. Lai, K.-W. Huang, Y. Han, L. Cavallo and L.-J. Li, *Chem. Commun.*, 2018, **54**, 11324–11327.
- 443 Y. Qiu, H. Zhong, W. Xu, T. Zhang, X. Li and H. Zhang, *J. Mater. Chem. A*, 2019, **7**, 5453–5462.
- 444 X. Wei, Z. Yin, K. Lyu, Z. Li, J. Gong, G. Wang, L. Xiao, J. Lu and L. Zhuang, *ACS Catal.*, 2020, **10**, 4103–4111.
- 445 K. G. Schmitt and A. A. Gewirth, *J. Phys. Chem. C*, 2014, **118**, 17567–17576.
- 446 A. Wagner, K. H. Ly, N. Heidary, I. Szabó, T. Földes, K. I. Assaf, S. J. Barrow, K. Sokołowski, M. Al-Hada, N. Kornienko, M. F. Kuehnel, E. Rosta, I. Zebger, W. M. Nau, O. A. Scherman and E. Reisner, *ACS Catal.*, 2020, **10**, 751–761.
- 447 D.-H. Nam, P. De Luna, A. Rosas-Hernández, A. Thevenon, F. Li, T. Agapie, J. C. Peters, O. Shekhah, M. Eddaoudi and E. H. Sargent, *Nat. Mater.*, 2020, **19**, 266–276.
- 448 C. A. Smith, M. R. Narouz, P. A. Lummis, I. Singh, A. Nazemi, C.-H. Li and C. M. Crudden, *Chem. Rev.*, 2019, **119**, 4986–5056.
- 449 F. Franco, M. F. Pinto, B. Royo and J. Lloret-Fillol, *Angew. Chem., Int. Ed.*, 2018, **57**, 4603–4606.
- 450 T. H. T. Myren, A. M. Lilio, C. G. Huntzinger, J. W. Horstman, T. A. Stinson, T. B. Donadt, C. Moore, B. Lama, H. H. Funke and O. R. Luca, *Organometallics*, 2019, **38**, 1248–1253.
- 451 T. H. T. Myren, A. Alherz, J. R. Thurston, T. A. Stinson, C. G. Huntzinger, C. B. Musgrave and O. R. Luca, *ACS Catal.*, 2020, **10**, 1961–1968.
- 452 J. A. Therrien and M. O. Wolf, *Inorg. Chem.*, 2017, **56**, 1161–1172.
- 453 Z. Cao, J. S. Derrick, J. Xu, R. Gao, M. Gong, E. M. Nichols, P. T. Smith, X. Liu, X. Wen, C. Copéret and C. J. Chang, *Angew. Chem.*, 2018, **130**, 5075–5079.
- 454 Z. Cao, D. Kim, D. Hong, Y. Yu, J. Xu, S. Lin, X. Wen, E. M. Nichols, K. Jeong, J. A. Reimer, P. Yang and C. J. Chang, *J. Am. Chem. Soc.*, 2016, **138**, 8120–8125.
- 455 M. R. Narouz, K. M. Osten, P. J. Unsworth, R. W. Y. Man, K. Salorinne, S. Takano, R. Tomihara, S. Kaappa, S. Malola, C.-T. Dinh, J. D. Padmos, K. Ayoo, P. J. Garrett, M. Nambo, J. H. Horton, E. H. Sargent, H. Häkkinen, T. Tsukuda and C. M. Crudden, *Nat. Chem.*, 2019, **11**, 419–425.
- 456 L. Zhang, Z. Wei, S. Thanneeru, M. Meng, M. Kruzyk, G. Ung, B. Liu and J. He, *Angew. Chem.*, 2019, **131**, 15981–15987.
- 457 Z. Cao, J. S. Derrick, J. Xu, R. Gao, M. Gong, E. M. Nichols, P. T. Smith, X. Liu, X. Wen, C. Copéret and C. J. Chang, *Angew. Chem., Int. Ed.*, 2018, **57**, 4981–4985.
- 458 H. Lu, Z. Zhou, O. V. Prezhdo and R. L. Brutchey, *J. Am. Chem. Soc.*, 2016, **138**, 14844–14847.
- 459 M. J. Trujillo, S. L. Strausser, J. C. Becca, J. F. DeJesus, L. Jensen, D. M. Jenkins and J. P. Camden, *J. Phys. Chem. Lett.*, 2018, **9**, 6779–6785.
- 460 A. Bakker, A. Timmer, E. Kolodzeiski, M. Freitag, H. Y. Gao, H. Mönig, S. Amirjalayer, F. Glorius and H. Fuchs, *J. Am. Chem. Soc.*, 2018, **140**, 11889–11892.
- 461 S. Dery, S. Kim, G. Tomaschun, I. Berg, D. Feferman, A. Cossaro, A. Verdini, L. Floreano, T. Klüner, F. D. Toste and E. Gross, *J. Phys. Chem. Lett.*, 2019, **10**, 5099–5104.
- 462 G. Lovat, E. A. Doud, D. Lu, G. Kladnik, M. S. Inkpen, M. L. Steigerwald, D. Cvetko, M. S. Hybertsen, A. Morgante, X. Roy and L. Venkataraman, *Chem. Sci.*, 2019, **10**, 930–935.

